Fiber Resonators and Lasers

by

Li Wei

A Thesis
presented to the University of Waterloo
in fulfilment of the
thesis requirement for the degree of
Doctor of Philosophy
in
Physics

Waterloo, Ontario, Canada, 2000

©Li Wei 2000

National Library of Canada
Acquisitions and Bibliographic Services
395 Wellington Street
Ottawa ON K1A 0N4
Canada

Bibliothèque nationale du Canada
Acquisitions et services bibliographiques
395, rue Wellington
Ottawa ON K1A 0N4
Canada

Your file Votre reference

Our file Notre référence

The author has granted a non-exclusive licence allowing the National Library of Canada to reproduce, loan, distribute or sell copies of this thesis in microform, paper or electronic formats.

L'auteur a accordé une licence non exclusive permettant à la Bibliothèque nationale du Canada de reproduire, prêter, distribuer ou vendre des copies de cette thèse sous la forme de microfiche/film, de reproduction sur papier ou sur format électronique.

The author retains ownership of the copyright in this thesis. Neither the thesis nor substantial extracts from it may be printed or otherwise reproduced without the author's permission.

L'auteur conserve la propriété du droit d'auteur qui protège cette thèse. Ni la thèse ni des extraits substantiels de celle-ci ne doivent être imprimés ou autrement reproduits sans son autorisation.

0-612-53524-X

Canada

The University of Waterloo requires the signatures of all persons using or photocopying this thesis. Please sign below, and give address and date.

ABSTRACT

This thesis discusses the very important components in wavelength-division multiplexed (WDM) fiber-optic communication systems — fiber laser sources and fiber Bragg grating filters. Three areas are included: theoretical studies of fiber ring resonators with an external reflector (FRRER) and compound ring resonator with an external reflector (CRRER); implementation of erbium-doped fiber lasers (EDFLs) based on the proposed passive resonators; and theoretical studies of phase-shifted fiber Bragg grating filters.

An FRRER is made with a ring resonator, a coupler and a reflector, while a CRRER made with double ring resonators, double couplers, and a reflector. We analyze theoretically both of the resonators with regard to their resonance conditions and directionality properties. The outputs and circulating intensities of the resonators are investigated. The optimum design relationships are obtained by examining the resonators. The result shows that both resonators are suitable for development of traveling-wave fiber lasers without use of optical isolators because of a high loss difference between the counter-clockwise and clockwise directions.

Whilst both resonators feature non-reciprocal property, comparing with the single resonator FRRER, the CRRER with double resonators has advantages of potentially large free spectral range due to vernier effect. The effects of the coupling coefficients, losses

and resonant numbers on the resonance are discussed for the double resonators. These resonators have properties very suitable for the construction of lasers.

Based on the proposed resonators, erbium-doped fiber lasers are fabricated. As expected, the unidirectional operation is achieved in EDFLs without need of optical isolators. The robust single-longitudinal-mode operation is achieved by employing the compound ring resonator to enhance the mode selectivity. Based on the configuration of the FRRER, by adding another reflector to the other end of the coupler, We have demonstrated a novel erbium-doped fiber laser operating at two wavelengths. The benefit of this approach is simplicity, compact and low cost.

A phase-shifted fiber Bragg grating, when combining with optical circulator, it may be used as add/drop de/multiplexer, which has very useful application in WDM fiber-optic communication systems. A comprehensive theoretical analysis of the compound phase-shifted uniform fiber Bragg grating (FBG) filter is presented. The transmission characteristics are examined by a transfer matrix formulation. The result shows that by suitably choosing the ratio, a quasi-flat-top spectrum may be obtained. The general condition of the optimum case is derived. This characteristic makes the compound phase-shifted uniform FBG filter particularly advantageous.

Acknowledgements

Special thanks to my supervisor, Dr. John Lit for his advice, guidance. His patience, frankness and encouragement helped me in finishing this work.

Many thanks are also due to my committee members, Dr. Walter W. Duley, Dr. John Vanderkooy, Dr. Robert MacPhie and Dr. Real Vallee for their interests in my work.

I am very grateful to Dr. Weiping Huang and Dr. Xun Li for providing optical spectrum analyzer, Dr. Donna Strickland for scope camera and rf spectrum analyzer, and Manfred Gartner for power amplifier.

I also wish to thank Kevin Zhang, Reed Seaver, Gonzallo Wills, Sylvain Langlois, Hossam Zoweil and Gautam Das for their interests and support. I would like to thank my family and friends for their encouragement.

To my mother and father

For their love, understanding, and steadfast support,
no matter how bad things seemed to get.

Table of Contents

List of Figures

List of Tables

List of Acronyms

ASE	Amplified Spontaneous Emission
ccw	counter-clockwise
cw	clockwise
CRR	Compound Ring Resonator
CRRER	Compound Ring Resonator with an External Reflector
DCRR	Double Coupler Ring Resonator
DCRRER	Double-coupler Ring Resonator with an External Reflector
DSF	Dispersion-Shifted Fiber
EDF	Erbium-Doped Fiber
EDFA	Erbium-Doped Fiber Amplifier
EDFL	Erbium-Doped Fiber Laser
EDFRL	Erbium-Doped Fiber Ring Lasers
ESA	Excited State Absorption
FBG	Fiber Bragg grating
FFP	Fiber Fabry-Perot
FP	Fabry-Perot
FRR	Fiber ring resonator
FRRER	Fiber ring resonator with an external reflector
FSR	Free Spectral Range
FWHM	Full Width at Half Maximum
HP	Hewlett Packard
HWP	Half-Wave Plate
LD	Loss Difference
LD	Laser Diode
MOPA	Master-Oscillator Power-Amplifier
MMF	Multimode Fiber
MZT	Mach-Zehnder Interferometer
NA	Numerical Aperture
OFDM	Optical Frequency-Division-Multiplexed
OC	Output Coupler
OI	Optical Isolator
OSA	Optical Spectrum Analyzer
PC	Polarization Controller
PZT	Pizeo-electrical Transducer
RIN	Relative Intensity Noise
RoL	Ratio of Length
QWP	Quarter-Wave Plate
SMF	Singlemode Fiber
SLM	Single Longitudinal Mode
SOP	States of Polarization
TTM	Transfer Matrix Method
WDM	Wavelength-Division Multiplexing

List of Symbols

α	Amplitude attenuation coefficient	
β	Propagation constant	μm^{-1}
r	Reflectivity of reflector	
$\Delta\lambda_{3dB}$	Linewidth	nm
γ_i	Coupler loss	dB
λ	Wavelength	μm, nm
δ_s	Phase: $\beta(l_1 + l_2)$	rad
δ_p	Phase: $\beta(l_2 + l_3)$	rad
ξ_i	Splice loss	dB
a_i, b_i	Simplified coupling coefficients	
f	Frequency	Hz
j	Imaginary number $\sqrt{-1}$	
k_i	Coupling coefficient of coupler	
k_{2r}^{3dB}	k_2-value for optimum resonance	
κ_g	Strength coupling coefficient	mm^{-1}
n	refractive index	
n_{eff}	Effective refractive index	
p_i	Transmission factor: $e^{(-\alpha L_i - \xi_i)}$	
α_{ccw}	Loss coefficients for the ccw direction	mm^{-1}
α_{cw}	Loss coefficients for the cw direction	mm^{-1}
N_0	Steady-state population difference	
τ_{sp}	Spontaneous lifetime	ns
ζ	Thermo-optic coefficient	$(°C)^{-1}$
ρ_e	Photoelastic constant	
ε	Applied strain	

Chapter 1

Introduction

Optical fiber communication systems are lightwave systems that employ optical wave as information carrier and optical fiber as information transmission line. In theory, the greater the carrier frequency, the larger the available transmission bandwidth and thus the information-carrying capacity of the communication systems. Such a system at optical frequencies offers an increase in the potential usable bandwidth by a factor of around 10^5 over traditional microwave transmission. The proposal for optical communication via optical fibers was made almost simultaneously in 1966 by Kao and Hockham [1] and Werts [2]. It is obvious that the suitable optical source and the optical fiber are the key elements for the development of optical fiber communication. During 1960s, the optical fiber exhibited very high attenuation (i.e. 1000 dB/km). Although the availability of laser sources had stimulated research into optical fiber communication, optical fiber communication was not considered to be practical until 1970, when optical fiber technology had advanced to the point where the fiber with loss of 20 dB/km or less was achieved [3]. Since then, silica fiber and optoelectronics including laser sources have been the subject of large-scale world wide research and product development. As a result, optical fiber communication is established today as one of the most promising technologies within the area of short and long-distance data transmission [4-6].

The development of technology in optical fiber communication systems has passed through a few distinct stages to increase the capacity of the optical systems. The *bit rate-distance product (BL)* was commonly used as a figure of merit to measure the system capacity, where B is the bit rate and L is the repeater spacing [7]. It is found that the ultimate capacity BL is determined by the quality of the optical source and the fiber. Table 1.1 shows the typical characteristics of the five distinct stages in the development of optical communication systems. It can be seen how the BL product has increased through technical progress either in optical fiber or in the optical source. The optical fiber has evolved from multimode fiber (MMF) to singlemode fiber (SMF), then to dispersion-shifted fiber (DSF) to reduce the dispersion in the fiber. On the other hand, the wavelength of the optical sources has shifted from 0.85μm to 1.3μm, then to 1.5μm; the three wavelength regions correspond to the first, second and third communication "window"s (see figure 1.1), where the fiber has low loss. At the same time, the optical source has advanced from broad-spectrum LEDs to multi-mode laser diode and then to single-mode laser diode.

Table 1.1 Five stages of optical fiber communication systems

Stage	Source	Fiber	B (b/s)	L (km)	BL (b/s-km)
I	0.85μm, LED	MMF	45~100 M	10	~500 M
II	1.3μm, MML	MMF	100 M	20	2 G
III	1.3μm, MML	SMF	10 G	80	800 G
IV	1.5μm, SML	DSF	10 G	100	1 T
V	1.5μm, SML, ♠	DSF	100 G	9100	910 T

Note: LED: light-emission diode; MML: multi-mode laser; SML: single-mode laser; MMF: multimode fiber; SMF: singlemode fiber; DSF: dispersion-shifted fiber; ♠ use of optical amplifier and WDM

The progress in optical sources plays a very important role in minimizing the dispersion. A laser source with a very narrow linewidth would be very desirable. Fiber lasers have the potential of being an excellent candidate as such a source in optical communication systems [8-9]. Compared to a laser diode, whose linewidth is limited by the short cavity length, a fiber laser [10-19] could have a much narrower linewidth. A linewidth as narrow as 0.95 kHz was obtained in fiber laser [20]. Moreover, fiber lasers are the most natural source for fiber-optic communications, since the light is already in the fiber and they can be directly spliced to the systems.

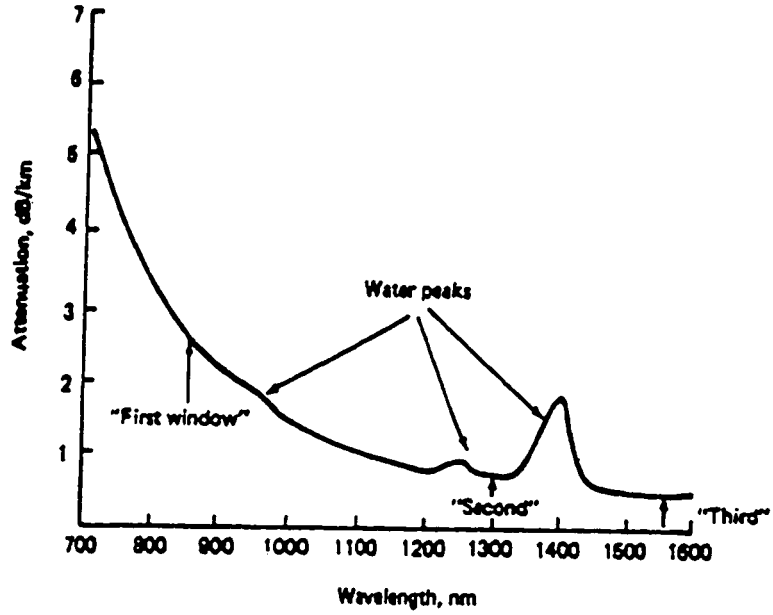

Figure 1.1 Spectral windows in single-mode fibers

Besides efforts in laser source, the advent of optical amplifier [21-25] and wavelength-division multiplexing (WDM) [26-29] in **stage V** has led to a revolution in lightwave systems, where optical amplifiers were used to increase the repeater spacing

and the WDM to increase the bit rate. Erbium-doped fiber amplifier (EDFA) as optical amplifier was developed during the 1980s and became available commercially by 1990. By using 274 EDFAs, a total transmission distance of 9,000 km was achieved [30]. Further improvement in the system capacity was achieved by using WDM strategy. WDM corresponds to the scheme in which multiple optical sources at different wavelengths are transmitted over the same fiber. WDM systems provide savings in the costs of installing and upgrading lightwave systems. It has already come into commercial use. Figure 1.2 shows schematically a WDM system. A set of optical signals at wavelengths, λ_1, λ_2, ...,λ_n , are combined together by a multiplexer, and then launched into the optical fiber. At the other end of the fiber, the signals are separated by a demultiplexer, and forwarded to their final destinations. It can be seen that multiple optical sources and multi/demultiplexer are the important elements in a WDM system.

In general a set of laser diodes operating at different wavelengths are used as multiple optical sources. However, it would increase the cost and complexity. To overcome this problem, various approaches have been tried to achieve simultaneous multiple wavelength lasing in both semiconductors [31-32] and fibers [33-34]. In recent years, multiwavelength fiber lasers [35-45] have attracted a lot of interest for optical system, because of their fiber compatibility, compact size and simplicity.

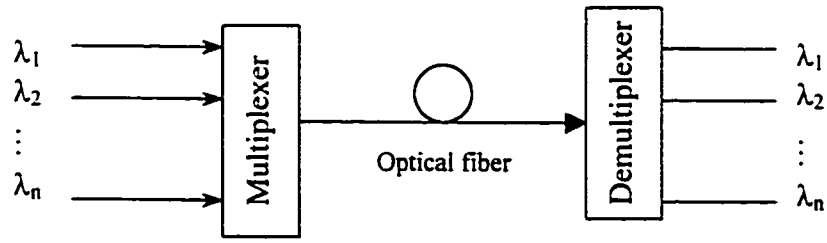

Figure 1.2 The principle of an optical WDM communication system

Other key elements in WDM systems are multiplexer and demultiplexer used to combine and split optical signals at different wavelengths. According to the wavelength spacing between adjacent signals, there are two kinds of WDM systems: widely-spaced WDM systems and dense WDM systems (or optical frequency-division-multiplexed (OFDM)). In the first type of systems, the wavelength spacing is about 10 to 300 nm, and in the latter systems, it is about 0.1 nm or less. Dense WDM systems are the subjects of current research interests. Multiplexing can be carried out by either passive couplers [46] or frequency selective devices, while the structure of a demultiplexer relies heavily on frequency selective devices. In a widely-spaced WDM system, bulk-type diffraction gratings [47] or dielectric thin-film filters [48] are normally used as frequency selective devices. In dense WDM systems, demultiplexer is essentially based on highly selective optical filters. Various schemes of optical filters have been demonstrated, including Fabry-Perot interferometers [49,50], Mach-Zehnder interferometers [51,52], and fiber grating-based filters [53,54]. For much of this decade, since the demonstration in 1989 of the holographic sidewriting technique for fabricating fiber Bragg grating, there has been considerable interest in developing grating-based filters because of their high reflectivity, simple fabrication, and fiber compatibility.

This thesis presents fiber resonators and their applications in erbium-doped fiber lasers. The study begins with the design of passive fiber ring resonators, which may be used as passive cavities for fiber lasers. By using the new resonator configurations, a single-longitudinal mode erbium-doped fiber laser (EDFL) was realized. Based on the EDFL, we also built a tunable dual-wavelength EDFL. In addition, another very

important component in WDM system, fiber Bragg grating filters is presented in appendix A.

1.1 Organization of Thesis

This thesis presents optical fiber devices—fiber resonators, erbium-doped fiber lasers (EDFL), as well as fiber Bragg grating filters. The fiber resonators are used to construct EDFL; they can also be used as narrow-band spectral filters. These components have great potential applications in fiber-optic communications, as narrow-linewidth optical sources and add/drop de/multiplexers.

This work is divided into several chapters. A short introduction is given in chapter 1. The background of fiber lasers with emphasis on erbium-doped fiber lasers is provided in chapter 2. Starting with the rate equations, we establish analytical and explicit expressions for the EDFL, which allow us to study the output power, threshold, slope efficiency, and the optimum length of the EDF.

Fiber lasers can be designed with a variety of choices for the laser cavity. In chapter 3, we present a new configuration, i.e., a basic fiber ring resonator with an external reflector (FRRER), which allow unidirectional operation in the ring cavity to be obtained without the use of optical isolators. Directionality and resonator analyses are given by analyzing the fields and intensities of the resonator, with the help of the coupled mode equations between the coupler and propagation equations.

In chapter 4 we propose a compound ring resonator with an external reflector (CRRER), which is aimed to obtain the unidirectional operation, and more importantly, to increase the free spectral range of the resonator to promote mode selectivity. This

chapter starts with a complete theoretical analysis of the compound ring resonator (CRR), including the optimum resonant condition, mode suppression, and how the parameters of the CRR affect the resonator characteristics. We then deal with the CRRER, including the directivity and resonator analysis.

In chapter 5, we present the implementations of the erbium-doped fiber lasers, based on the resonators proposed in chapter 3 and chapter 4. We first describe the related fiber laser devices in order to have a better understanding of the construction of the EDFLs. We then present the experimental results of the EDFLs, including single-wavelength EDFLs, as well as dual-wavelength EDFL.

The thesis concludes with chapter 6, which summarizes the work done on fiber resonators and fiber laser.

While the laser source is the very important component in fiber-optic communication systems, optical filters, such as, add/drop de/multiplexer, also play a critical role in the WDM technology. In appendix A, a new all-fiber phase-shift Bragg grating filter with symmetric structure is presented. Optimum conditions for the transmission curve with flat top characteristics are given for 2 and 3 phase-shift grating filters.

1.2 Summary of Contributions

This thesis describes passive fiber ring resonators, erbium-doped fiber lasers, dual-wavelength fiber laser, and fiber grating filters for optical communication systems. The following is a list of the contributions.

- By applying rate equations, laser properties such as output power and slope efficiency are derived for a fiber ring erbium-doped laser.
- Analyzed and calculated a compound fiber ring resonator (CRR), including optimum resonating conditions.
- Proposed and analyzed two fiber ring resonators (fiber ring resonator (FRR) and CRR) with external reflector, which may be used to build travelling-wave fiber ring lasers without the use of optical isolator.
- Designed and built travelling-wave single-longitudinal-mode erbium-doped fiber lasers without using nonreciprocal element based on the proposed ring resonator with external fiber grating.
- Designed and characterized a new tunable dual-wavelength erbium-doped fiber ring laser with output coming out from two separate ports, based on a ring resonator with two fiber gratings.
- Proposed and analyzed compound phase-shifted Bragg grating filters with symmetrical structures by applying a transfer matrix method (TTM). The transmission spectrum of such filters can be tailored to give a quasi-flat top.

1.3 References

1. C.K. Kao, G.A. Hockman, "Dielectric fiber surface waveguides for optical frequencies," *Proc. IEE*, vol. 113, pp.1151-1158, 1966.
2. Werts, "Propagation de la lumiere conherente dans les fibres optiques," *L'Onde Electrique*, 46, p.967, 1966.

3. F.P. Kapron, D.D. Keck, and R.D. Maurer, "Radiation losses in glass optical waveguides", *Appl. Phys. Lett.*, 17, pp.423-425, 1970.
4. S.E. Miller and I.P. Kaminow, Eds., *Optical Fiber Telecommunications II*, academic Press, San Diego, CA 1988.
5. G. Keiser, *Optical Fiber Comminations*, 2nd ed., MaGraw-Hill, New York, 1991.
6. P.E. Green, Jr., *Fiber-Optic Networks*, Prentice-Hall, Englewood Cliffs, New Jersey, 1993.
7. G.P. Agrawal, *Fiber-Optic Communication systems*, Wiley, New York, 1992.
8. V. Mizrahi, D.J. DiGiovanni, R.M. Atkins, S.G. Grubb, Y.-K. Park, and J.-M. Pdelaraux, "Stable single-mode erbium fiber grating laser for digital communications," *J. Lightwave Technol.*, vol. 11, pp.2021-2025, 1993.
9. J.L. Zyskind, J.W. sulhoff, P.D. Magill, K.C. Reichmann, and D.J. DiGiovanni, "Transmission over 653 km using an externally modulated diode-pumped erbium-doped fiber grating laser source." *Electron. Lett.*, vol. 29, pp.1105-1106, 1993.
10. C.C. Lee, Y.K. Chen and S.K. Liaw, "Single-longitudinal-mode fiber laser with a passive multiple-ring cavity and its application for video transmission," *Opt. Lett.*, vol. 23, pp. 358-360, 1998.
11. A. Gloag, N. Langford, K. McCallion and W. Johnstone, "Continuously tunable single-frequency erbium ring fiber laser," *J. Opt. Soc. Am. B*, vol.13, pp.921-925, 1996.
12. A.J. Gloag, N. Langford, I. Bennion and L. Zhang, "Single-frequency travelling-wave erbium doped fibre laser incorporating a fibre Bragg grating," *Opt. Communication*, vol. 123, pp.553-557, 1996.

13. J. Zhang, C.Y. Yue, G.W. Schinn, W.R.L. Clements, and J.W.Y. Lit, "Stable single-mode compound-ring erbium-doped fiber laser," *J. Lightwave Technol.*, vol.14, pp.104-109, 1996.

14. M.J. Guy, J.R. Taylor and R. Kashyap, "Single-frequency erbium fibre ring laser with intracavity phase-shifted fibre Bragg grating narrowband filter," *Electron.Lett.*, vol.31, pp.1924-1925, 1995.

15. K. Iwatsuki, H. Okamura, and Msaruwatari, "Wavelength-tunable single-frequency and single-polarization Er-doped fibre ring-laser with 1.4 kHz linewidth", *Electron. Lett.*, vol. 26, pp.2033-2034, 1990.

16. C. V. Poulsen and M. Sejka, "Highly optimized tunable Er^{3+}-doped single longitudinal mode fiber ring laser, experiment and model," *IEEE Photon. Technol. Lett.*, vol. 5, pp.646-648, 1993.

17. D.I. Chang, M.J. Guy, S.V. Chernikov, J.R. Taylor and H.J. Kong, "Single-frequency erbium fibre laser using the twisted-mode technique," *Electron. Lett* vol.32, pp.1786-1787, 1996.

18. W.H. Loh, B.N. Samson, L. Dong, G.J. Cowle, and K. Hsu, "High performance single frequency fiber grating-based erbium:ytterbium-codoped fiber lasers," *J. Lightwave Technol.*, vol. 16, pp.114-118, 1998.

19. K. Hsu, W.H. Loh, L. Dong, C.M. Miller, "Efficient and tunable Er/Yb fiber grating lasers," *J. Lightwave Technol.*, vol.15, pp.1438-1441, 1997.

20. Y.Cheng, J.T. Kringlebotn, W.H. Loh, R.I. Laming, and D.N. Payne, "Stable single-frequency traveling-wave fiber loop laser with integral saturable-absorber-based tracking narrow-band filter," *Opt. Lett.*, vol. 20, pp.875-877, 1995.

21. M.J.F. Digonnet, Ed., *Rare-Earth Doped Fiber Lasers and Amplifiers*, Marcel Dekker, New York, 1993.

22. A. Bjarklev, *Optical Fiber Amplifiers: Design and System Applications*, Artech House, Boston, 1993.

23. E. Desurvire, *Erbium-Doped Fiber Amplifiers*, Wiley, New York, 1994.

24. H. Taga, Y. Yoshida, S. Yamamoto, and H. Wakabayashi, "459 km, 2.4 Gbit/s from wavelength multiplexing optical fibre transmission experiment using six Er-doped fibre amplifiers", *Electron. Lett.*, vol. 26, pp.500-501, 1990.

25. P.M. Gabla, J.O. Frorud, E. Leclerc, S. Gauchard, and V. Havard, "1111 km, two-channel IM-DD transmission experiment at 25 Gb/s through 21 in-line erbium-doped fiber amplifiers", *IEEE Photon. Technol. Lett.*, vol. 4, pp.717-720, 1992.

26. S.S. Wagner and H. Kobrinski, "WDM applications in broadband telecommunication networks," *IEEE communications Magazine*, pp.22-30, March 1989.

27. G.R. Hill, "Wavelength domain optical network techniques," *Proc. IEEE*, vol. 77, pp.121-132, 1990.

28. M. Fujiwara, M. Goldman, M. O'Mahony, O. Tonguz, and A. Willner, "Special issue on multiwavelength optical technology and networks," *J. Lightwave Technol.*, vol. 14, pp932-935, 1996.

29. R.L. Cruz, G.R. Hill, A.L. Kellner, R. Ramaswami, G.H.Sasaki, and Y. Yamabayashi, "Optical networks," *Selected Areas in Communications*, IEEE Communications Society, pp761-763, 1996.

30. N.S. Bergano and C.R. Davidson, "Wavelength division multiplexing in long-haul transmission systems", *J. Lightwave technol.*, vol. 14, pp.1299-1308, 1996.

31. I.H. White, and K.O. Nyairo, "Demonstration of A 1×2 multichannel grating cavity laser for wavelength division multiplexing (WDM) applications," *Electron. Lett.*, vol. 26, pp.832-834, 1990.

32. M.C. Farries, A.C. Carter, G.G. Jones, and I. Bennion, "Tunable multiwavelength semiconductor laser with single fibre output," *Electron. Lett.*, vol. 27, pp.1498-1499, 1991.

33. H. Takahashi, H. Toba, and Y. Inoue, "Multiwavelength ring laser composed of EDFAs and an arrayed-waveguide wavelength multiplexer," *Electron. Lett.*, vol.30, pp.44-45, 1994.

34. H. Okamura and K. Iwatsuki, "Simultaneous oscillation of wavelength-tunable, singlemode lasers using an Er-doped fibre amplifier," *Electron. Lett.*, vol.28, pp.461-463, 1992.

35. J.W. Dawson, N. Park, and K.J. Vahala, "Co-lasing in an electrically tunable erbium-doped fiber laser," *Appl. Phys. Lett.*, vol.60, pp.3090-3092, 1992.

36. N. Park, J.W. Dauson, and K.J. Vahala, "Multiple wavelength operation of an erbium-doped fiber laser," *IEEE Photon. Technol. Lett.*, vol.4, pp.540-541, 1992.

37. S.V. Chernikov, R. Kashyap, P.R. Mckee and J.R. Taylor, "Dual frequency all fibre grating laser source," *Electron. Lett.*, vol.19, pp.1089-1091, 1993.

38. S.V. Chernikov, J.R. Taylor, and R. Kashyap, "Coupled-cavity erbium fiber lasers incorporating fiber grating reflectors," *Opt. Lett.*, vol.18, pp.2023-2025, 1993.

39. T. Komukai and M. Nakazawa, "Tunable single frequency erbium doped fiber ring lasers using fiber grating etalons," *Jpn. J. Appl. Phys.*, vol.34, pp.L679-680, 1995.

40. J. Chow, G. Town, B. Eggleton, M. Ibsen, K. Sugden, and I. Bennion, "Multiwavelength generation in an erbium-doped fiber laser using in-fiber comb filters," *IEEE Photon. Technol. Lett.*, vol.8, pp.60-62, 1996.

41. S. Yamashita and K. Hotate, "Multiwavelength erbium-doped fibre laser using intracavity etalon and cooled by liquid nitrogen," *Electron. Lett.*, vol.32, pp.1298-1299, 1996.

42. O. Graydon, W.H. Loh, R.I. Laming, and L. Dong, "Triple-frequency operation of an Er-doped twincore fiber loop laser," *IEEE Photon. Technol. Lett.*, vol.8, pp.63-65, 1996.

43. J. Nilsson, Y.W. Lee and S.J. Kim, "Robust dual-wavelength ring-laser based on two spectrally different erbium-doped fiber amplifiers," *IEEE Photon. Technol. Lett.*, vol.8., pp.1630-1632, 1996.

44. S. Li, H. Ding and K.T. Chan, "Erbium-doped fibre lasers for dual wavelength operation," *Electron. Lett.*, vol.33, pp.52-53, 1997.

45. S. Yamashita, and G.J. Cowle, "Bidirectional 10-GHz optical comb generation with an intracavity fiber DFB pumped Brillouin/Erbium fiber laser," *IEEE Photon. Technol. Lett.*, vol.10, pp.796-798, 1998.

46. C. Dragone, "An NxN optical multiplexed using a planar arrangement of two star couplers," *IEEE Photon. Technol. Lett.*, vol.3, pp.812-815, 1991.

47. R. Watanabe, K. Nosu and Y. Fujii, "Optical grating multiplexed in the 1.1-1.5 μm wavelength region," *Electron. Lett.*, vol.16, pp.108-109, 1980.

48. J. Minowa and Y. Fujii, "Dielectric multilayer thin-film filters for WDM transmission systems," *J. Lightwave technol.*, vol. 1, no.1, pp116-121, March 1983.

49. A.A.M. Saleh and J. Stone, "Two-stage Fabry-Perot filters as demultiplexers in optical FWDM LAN's, " *J. Lightwave technol.*, vol.7, pp.323-330, 1989.

50. J. Stone and L.W. Stulz, "High performance fibre Fabry-Perot filters," *Electron. Lett.*, vol.27, pp.2239-2240, 1991.

51. H. Toba, K. Oda, N. Takato and K. Nosu, "5-GHz spaced, eight-channel, guided-wave tunable multi/demultiplexer for optical FDM transmission systems," *Electron. Lett.*, vol.23, pp.788-789, 1987.

52. K. Inoue, N. Takato, H. Toba and M. Kawachi, "A four-channel optical waveguide multi/demultiplexer for 5-GHz spaced optical FDM transmission," *J. Lightwave technol.*, vol. 6, pp.339-345, 1988.

53. G.P. Agrawal and S. Radic, "Phase-shifted fiber Bragg Grating and their application for wavelength demultiplexing,"*IEEE Photonics Tech. Lett.*, vol.6, pp995-997, 1994.

54. R. Zengerle and O. Leminger, "Phase-shifted Bragg-grating filters with improved transmission characteristics," *J. Lightwave Technol.*, vol.13, pp2354-2358, 1995.

Chapter 2

Basic Principle of Erbium-Doped Fiber Lasers

The concept for fiber laser is not new, but it is a surprising idea. The theoretical concept behind fiber-laser operation is quite elegant. An optical fiber doped with a lasing material is optically pumped by a flashlamp or laser, and laser output is obtained from the fiber. Not only do the lasing medium and the fiber delivering system become one and the same, but the length of the active medium is theoretically unlimited, the spatial modes can be well controlled by the fiber waveguide and the fiber can be packaged in a small volume.

In this chapter, we will review the general fiber lasers, and examine their merits; we shall also review the erbium-doped fiber lasers. We shall first give the general background knowledge of erbium-doped fiber lasers such as the pump, gain, and rate equations. Then from the rate equations, we shall establish a few of the analytical and explicit expressions for an erbium-doped fiber ring laser, which include output power, laser threshold, slope efficiency, and optimum length of the erbium-doped fiber.

2.1 Historical Overview on Fiber Lasers

The first fiber laser [1] was demonstrated by Elias Snitzer as early as 1961 by using a neodymium(Nd)-doped glass fiber with a 300 μm core diameter, and slipping it inside a helical flashlamp. Late in 1965, with R. Woodcock, he investigated a glass doped with both erbium and ytterbium and achieved lasing action at 1.54 μm, still with

flashlamp as the pump source [2]. Erbium emission at 1.54 μm received some early attention in the mid-1960's, but even today it is still a commercially significant laser because of its use as an eye-safe laser for range finding applications [3-4]. As research on optical fiber communications began to take off in the early 1970s, so the quest for new light sources became important. In 1974 Julian Stone and Charles Burrus at Bell Labs used low-loss silica fiber to made Nd-doped fiber lasers which were end-pumped with diode lasers [5], but their technology languished because diode powers were low and their lifetimes were limited.

It was not until late 1980s that interest in rare-earth doped fiber lasers was revived. The development of rare-earth doped fiber lasers proceeded at an enormous pace [6-10], thanks to the impressive progress on diode laser pump source, the technology of rare-earth doping, and the development of many fiber optic components. The initial emphasis was focused on Nd- and Er-doped fiber lasers [11-12], but other dopants such as holmium (Ho), samarium (Sm), thulium (Tm), and ytterbium (Yb) were also investigated. Table 2.1 lists the doped ions and the transitions used for the laser action, the types of the fiber used as host, and the wavelengths emitted by the lasers. It can be seen that fiber lasers cover the wavelength ranging from about 450 to 3500 nm. This considerable spectral range suggests a myriad of potential applications for the fiber laser such as in optical data storage, optical communications, photonic switching, range finding, sensor technology, and medical applications.

Among rare-earth doped fiber lasers, erbium-doped fiber lasers at 1.5 μm region attracted the most attention because it coincides with the least-loss (as low as 0.15dB/km) region of silica fibers used for lightwave communications. Erbium doped fiber lasers can

Table 2.1 Wavelengths emitted by rare-earth-doped fiber lasers

Doped Ion	Transition	Type of Fiber	Wavelength (μm)
Er^{3+}	$^4S_{3/2} \rightarrow {}^4I_{15/2}$	Fluoride	0.55
	$^4S_{3/2} \rightarrow {}^4I_{13/2}$	Fluoride	0.85
	$^4I_{11/2} \rightarrow {}^4I_{15/2}$	Fluoride	0.98
	$^4I_{13/2} \rightarrow {}^4I_{15/2}$	**Silica/Fluoride**	**1.55**
	$^4F_{9/2} \rightarrow {}^4I_{9/2}$	Fluoride	3.50
Nd^{3+}	$^4F_{3/2} \rightarrow {}^4I_{9/2}$	Silica	0.92
	$^4F_{9/2} \rightarrow {}^4I_{11/2}$	Silica	1.06
	$^4F_{9/2} \rightarrow {}^4I_{13/2}$	Silica/Fluoride	1.35
Ho^{3+}	$^5S_2 \rightarrow {}^5I_8$	Fluoride	0.55
	$^5S_2 \rightarrow {}^5I_5$	Fluoride	1.35
	$^5I_7 \rightarrow {}^5I_8$	Silica/Fluoride	2.08
Pr^{3+}	$^3P_0 \rightarrow {}^3H_4$	Fluoride	0.49
	$^3P_1 \rightarrow {}^3H_4$	Fluoride	0.52
	$^1D_2 \rightarrow {}^3F_4$	Silica	1.05
Tm^{3+}	$^1G_4 \rightarrow {}^3H_5$	ZBLAN	0.48
	$^3H_4 \rightarrow {}^3H_6$	Fluoride	0.80
	$^3F_4 \rightarrow {}^3H_6$	Silica/Fluoride	1.90
Sm^{3+}	$^4G_{5/2} \rightarrow {}^6H_{9/2}$	Silica	0.65
Yb^{3+}	$^4F_{5/2} \rightarrow {}^4F_{7/2}$	Silica/Fluoride	1.02

Note: The wavelength shown in Table 2.1 is only indicative of the spectral region since it can be tuned over a wide range (~ 50 nm) for most fiber lasers.

be operated either in continuous wave or in pulse mode. Continuous wave EDFLs are preferred for applications in multi-channel lightwave systems, while pulsed mode EDFLs in soliton communication systems. The techniques of Q-switching and mode locking [13-14] can be used to produce high power short duration pulses, which will not be discussed in this thesis. We restrict our research to cw single-longitudinal mode EDFLs. In the next section, the merits of fiber lasers will be discussed. Section 2.3 will give a review of EDFLs.

2.2 Merits of Fiber Lasers

After over 20 years of research, fiber laser technology has moved from the laboratory to the commercial marketplace. Fiber lasers are well suited to industrial applications because they are compact and reliable. They have many advantages over other type of lasers. When compared to many solid-state and gas laser systems, fiber lasers are simpler and more compact and can be pumped with diodes. Compared to laser diodes, fiber lasers are spectrally cleaner and can be modulated with less chirp and signal distortion. Moreover, fiber-to-fiber compatibility is a distinct advantage in optical communication systems. Some of the merits of fiber lasers are:

- The intense and concentrated pumping available in rare-earth doped, single-mode fibers leads to lower threshold three-level laser operation, and improves efficiency, just as tighter confinement improves diode laser performance.
- The long, thin geometry of fibers makes heat removal much easier than in bulk solid-state lasers and the higher efficiency also means there is much less heat waste.

- Fiber waveguide and splicing alleviate any mechanical alignment of parts and provide superior environmental stability.
- There are many possible laser cavity designs and configurations, which are less cumbersome and more stable than their bulk optics counterparts.
- The long fiber cavity length leads to a very narrow linewidth; it also makes continuous wavelength tuning possible since cavity modes are closely spaced.
- High output and low relative intensity noise.

2.3 Review on Erbium-Doped Fiber Lasers

The first erbium-doped fiber laser was reported by R.J. Mears et al. [15] in 1986. The 90 cm single-mode EDFL described in [15] was pumped with a λ = 514.5 nm argon ion laser. It had a threshold of 30 mW absorbed pump power and a slope efficiency of 0.6%. In 1987, a low threshold (~ 2.5mW) cw operation of EDFL was demonstrated, pumped by a Styrl 9M dye laser at 807 nm [16]. The first laser-diode (LD) pumped EDFL was also reported in 1987; it used an 811-nm AlGaAs pump source [17]. It has a 3 mW oscillation threshold and 130 μW output power with a slope efficiency of 3.3%. The performance of EDFL [18-19] has been improved since these experimental results. In an EDFL pumped with a 0.82-μm LD, the threshold pump power was 5 mW with a slope efficiency of 8.5% in a 70-cm long cavity [18]. In another EDFL, with AlGaAs array for pump LD, output powers of EDFL [19] at 1.5 μm could be increased up to 8 mW with 13.5% slope efficiency with respect to launched pump power. However, the 800-nm pump band of Er^{3+} suffered from the serious disadvantage of pump excited-state absorption (ESA), which limited further improvement of the EDFLs.

The performance of EDFLs improves considerably when they are pumped at the 0.98 or 1.48-μm wavelength because of the absence of ESA. Indeed, semiconductor lasers operating at these wavelengths were developed solely for the purpose of pumping Er-doped fiber. Their use has resulted in excellent 1.55-μm fiber lasers to the extent that such devices are available commercially. As early as 1989, a 0.98-μm-pumped EDFL exhibited a slope efficiency of 58% with respect to absorbed pump power [20], a figure that is close to the quantum limit of 63% obtained by taking the ratio of signal to pump photon energies. EDFLs pumped at 1.48 μm also exhibit similarly good performance. In fact, the choice between 0.98 and 1.48 μm is not always clear since each pumping wavelength has its own merits. Both pumping wavelengths have been used for developing practical EDFLs with excellent performance characteristics [21-22].

The most important characteristics of cw EDFLs are their ability to provide narrow-linewidth single-longitudinal-mode (SLM) output and continuous wavelength tuning over a wide range. Such lasers are required for coherent optical communications, fiber sensing, and range finding. A wide variety of EDFL designs, based on either linear Fabry-Perot (FP) [23-28] or ring configurations [29-38], have been demonstrated by several research groups.

The first demonstration of SLM operation of EDFLs was based on a Fox-Smith resonator configuration [23]. The resonator was formed by coupling two cavities of erbium doped fiber as shown in Fig. 2.1. The two cavities of length 80 and 95 cm were pumped by an argon ion laser (514 nm) through port 1. The ends of arms 1 and 4 were butted against the dielectric mirrors. A diffraction-grating system was used on port 3 to tune the laser. In this configuration, longitudinal mode selection is based on the principle

of coupling two laser cavities of different lengths; the lengths are chosen so that the two sets of Fabry-Perot modes coincide only with large frequency periodicity, which results in a broad effective free spectral range (FSR). SLM oscillation with an 8.5 MHz linewidth and a slope efficiency of 0.04% were obtained in this configuration. The main drawback of this linear approach is the bulk pumping system, bulk tuning component, and end-butted fiber-mirror interface, which result in a poor pump efficiency, consequently, a low slope efficiency. Furthermore, a mirror with dielectric coatings could be damaged by focused, high-power pump radiation.

Modern fiber device—fiber Bragg grating (FBG), which is fabricated by the transverse writing of feedback elements directly into the fiber core with a UV radiation [39-40], provides a perfect way to avoid pumping the light through the dielectric mirrors. FBG is a reflective type of filter with a much narrower bandwidth than a dielectric mirror. In 1991, G.A. Ball [24] first utilized two FBGs to form a 50 cm linear FP cavity as shown in Fig.2.2(a). The two Bragg gratings were written holographically into the core of single-mode erbium-doped fiber. The reflectivities of the two FBGs were 80% and 72%. The laser was pumped with a Ti:sapphire laser at 980 nm. SLM operation with a 47 kHz linewidth was achieved. In this configuration, the FBGs provided good longitudinal mode discrimination and cavity feedback.

Single-frequency linear EDFLs with FBGs are attractive because of their engineering simplicity. In order to ensure single-frequency operation, however, such lasers must necessarily be short (a few centimeters) [41-42] so that only a few axial modes fall within the reflection bandwidth of the FBG. As a result of their inherent short lengths, these lasers normally suffer inadequate pump absorption, hence poor efficiency

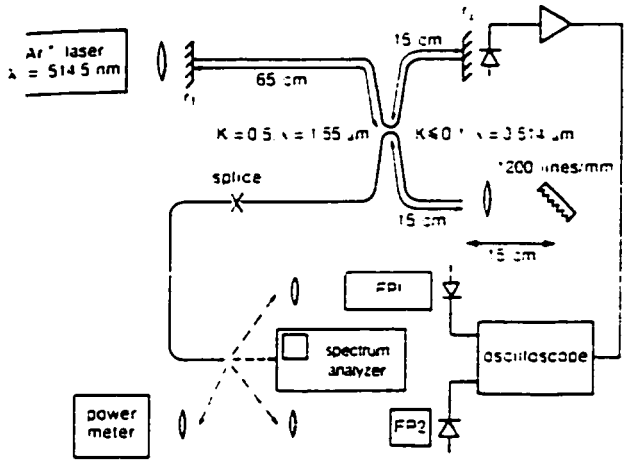

Figure 2.1 Fox-Smith resonator configuration

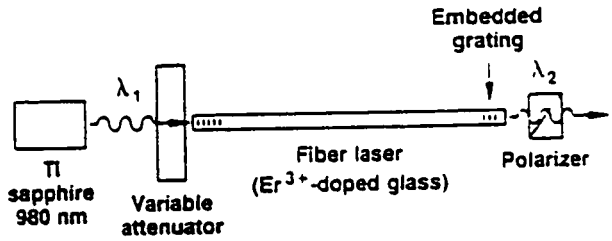

Figure 2.2(a) Linear FP cavity with fiber Bragg grating

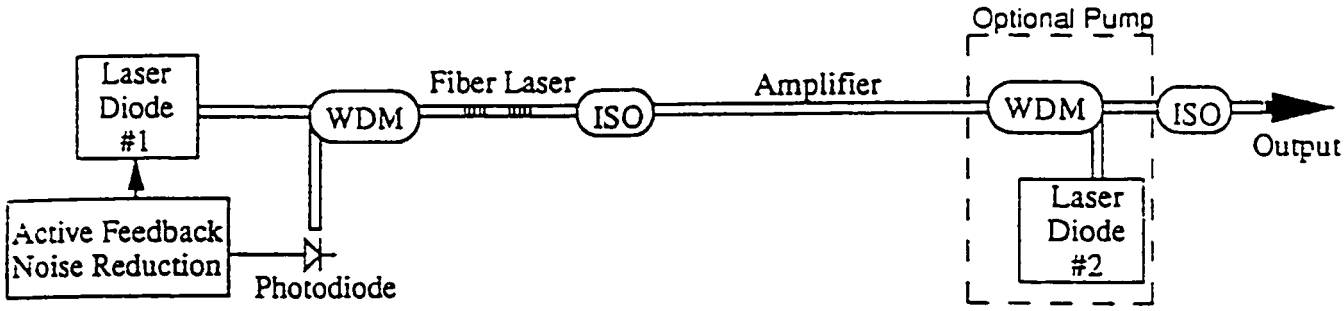

Figure 2.2(b) The MOPA configuration with fiber Bragg grating

and low output power. Increasing the erbium dopant concentration as a means of increasing the pump absorption is however problematic. It can result in self-pulsation and ion-ion interactions [43-44], which are detrimental to the performance of the laser.

This problem can be alleviated by either co-doping Er^{3+} fiber with Yb^{3+} [45-46] or using the so-called master-oscillator power-amplifier (MOPA) [47-48]. The Yb^{3+}-codoped Er^{3+} phosphate-glass or aluminophos phosilicate (P/Al/Si) fibers are capable of efficient pump absorption at 980 nm up to two orders of magnitude greater compared to Er^{3+}-doped fibers. As a result, co-doped Er/Yb fiber lasers show high output characteristics. Unfortunately, such lasers suffer from limited tunability (~ 5nm) due to the narrower gain spectrum of Er/Yb fibers [49]. The MOPA configuration (shown in Fig. 2.2(b)) is based on a short robust single frequency fiber laser followed by a piece of amplifier fiber, which is pumped by using the residual pump power from the laser. This design, while offering a high-power output and robust single-frequency operation, suffers from the high relative intensity noise (RIN), which is attributed to the low power oscillation.

An alternative approach which can alleviate these problems is to use a unidirectional ring configuration. It is well known that travelling-wave operation can eliminate spatial hole burning. This makes a ring-cavity design more suitable for SLM operation than a linear-cavity design when operating above threshold. Since ring configuration allows the use of much longer gain fiber lengths, ring lasers have potentially high slope efficiencies. Owing to the long cavity lengths, they also have narrow linewidths.

Because of these advantages, in recent years, there has been an increased interest in unidirectional erbium-doped fiber ring lasers (EDFRLs) [29-38]. So far, several different travelling-wave cavity designs have been studied, including unidirectional ring cavities [29-33] and unidirectional Sagnac-like loop cavities [34-38]. Robust SLM oscillation in the typically long cavity of a ring EDFL requires mode selection from an enormous number of densely spaced longitudinal modes lying beneath the erbium gain curve. Various schemes of mode selection have been used to achieve SLM operation in EDFRLs.

In an early experiment [29], two cascaded fiber Fabry-Perot (FFP) etalons with widely different FSRs were inserted in an EDFRL as mode selectors. Each of the two FFP filters has its own principal function in the compound resonator. The tuning and coarse mode selection were accomplished by the FFP with a large FSR (70 nm), while the FFP with a small FSR (12 GHz) was for fine mode selection. SLM operation with a linewidth less than 5.5 kHz was realized. Relatively good performance has been achieved in this configuration although the FFPs and a few optical isolators make it costly; moreover FFPs are prone to drift in the central wavelength as well.

Another attractive all-fiber ring configuration was reported by J. Zhang et al. [21], as shown in Fig. 2.3. This structure was based on an all-fiber compound-ring resonator in which a dual-coupler sub-ring was inserted into the main cavity as a mode selector. When combined with a tunable bandpass filter, the resonator enables robust SLM laser oscillation. The stable mode-hop free operation is achieved by an active stabilization scheme. Stable SLM with a linewidth less than 5 kHz was realized. Such a laser could

be tuned over 45 nm with a 20 mW output. In addition, similar structures [31,33] based on sub-ring resonator have been investigated to achieve SLM operation.

Besides the ring-cavity design, Sagnac-like loop cavity [34-38] is another type of travelling-wave configuration. It is of interest as it allows the use of reflective-type filter (e.g. FBG) rather than transmission-type filter, such as FFP, sub-ring resonator, in a ring cavity design. Fig. 2.4 shows the basic structure of a loop cavity. The fiber loop was formed by joining two output ports of a 3 dB coupler. With this configuration, G.J. Cowle et al. [34] demonstrated a SLM operation with a linewidth of 10 kHz. However, it suffers from mode hopping. Good performances have been achieved by the use of FBG [35] instead of dielectric mirror, and additional filter such as a narrowband grating filter [36], and a self-induced tracking filter [37] based on a piece of unpumped erbium-doped fiber. A similar configuration [38] which used an optical isolator instead of 3 *dB* coupler also gave good results.

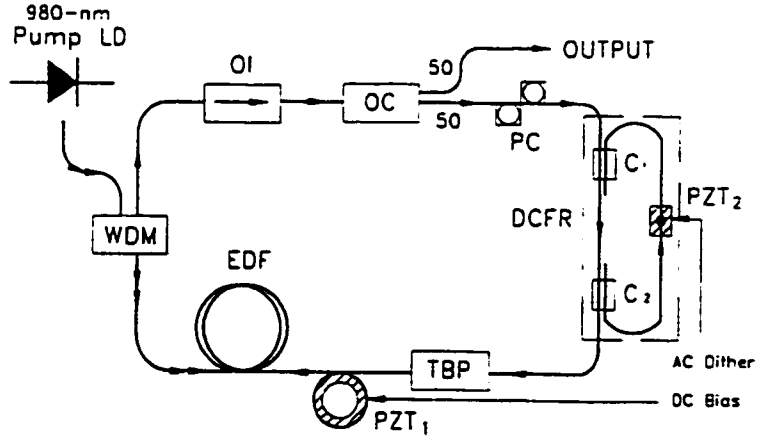

Figure 2.3 Attractive all-fiber ring configuration

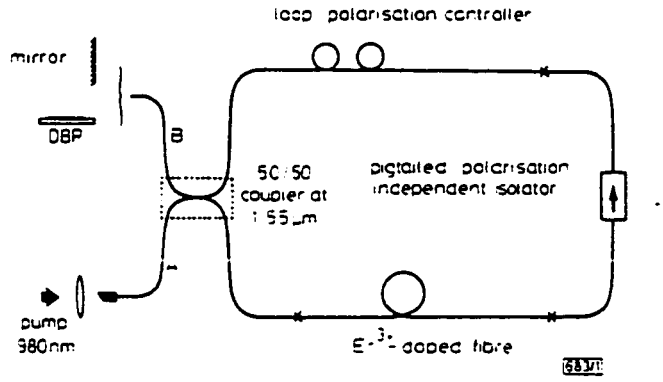

Figure 2.4 Basic structure of a loop cavity

Unidirectional operations of the above ring-cavity or loop-cavity lasers were achieved by using a nonreciprocal element – optical isolator. Unfortunately, such isolators will introduce additional destructive losses and much higher costs.

Recently, unidirectional erbium doped fiber ring lasers have been demonstrated without optical isolators [50-51]. In one case, nonreciprocal operation was achieved by an S-shape feedback loop formed by two couplers; a combination of polarization splitter and output coupler was used in the other. Although the linewidths of the lasers were measured to be less than 0.05 nm in [50] and 0.2 nm in [51], limited by the resolutions of the optical spectrum analyzers, single-longitudinal-mode operation was not confirmed.

2.4 Pump and Gain

When a rare-earth element, erbium, is doped into a silica host, it becomes triply ionized Er^{3+}. Due to the neighbouring atoms in the host lattice, Er^{3+} is subject to a crystal or ligand field. The ligand field caused a stark splitting of Er^{3+} energy level, and further, the amorphous nature of glass broadens energy levels of Er^{3+} into bands. Fig. 2.5 shows the relevant energy levels of Er^{3+} in silica glasses.

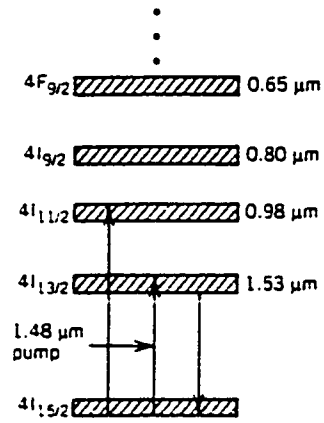

Figure 2.5 The relevant energy levels of Er^{3+} in silica glasses

A few transitions can be used to pump an erbium-doped fiber (EDF). However, the pump bands of 0.98 μm and 1.48 μm are the preferred choices as they are free from the problem of the excited state absorption. Normally, pumping can be achieved by the use of wavelength-division-multiplexing (WDM) coupler for both ring cavity and linear cavity. Optical gain is realized when the laser medium is pumped to achieve population inversion. Fig. 2.6 shows the general pump bands available to achieve stimulated emission at ~1.5 μm for an erbium doped silica fiber. The various absorption bands seen in this spectrum correspond to the absorption transitions shown in Fig. 2.5. Fig. 2.7(a) shows the gain and absorption spectra of an erbium-doped fiber (EDF) whose core is doped with germania [52]. The gain spectrum is quite broad with a double-peak structure. The shape and the width of the gain spectrum is quite sensitive to core composition. Fig. 2.7(b) shows the emission spectra for four different core compositions [53].

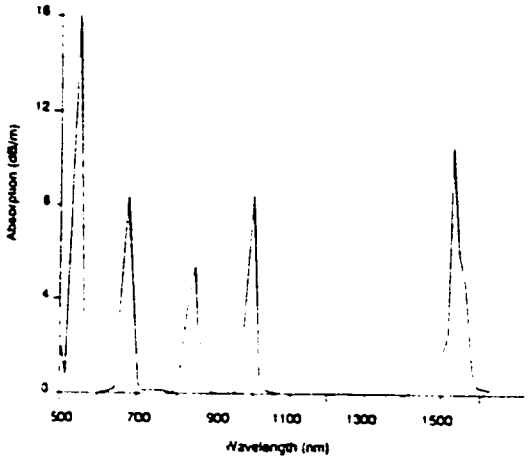

Figure 2.6 Absorption spectrum of an erbium doped silica fiber

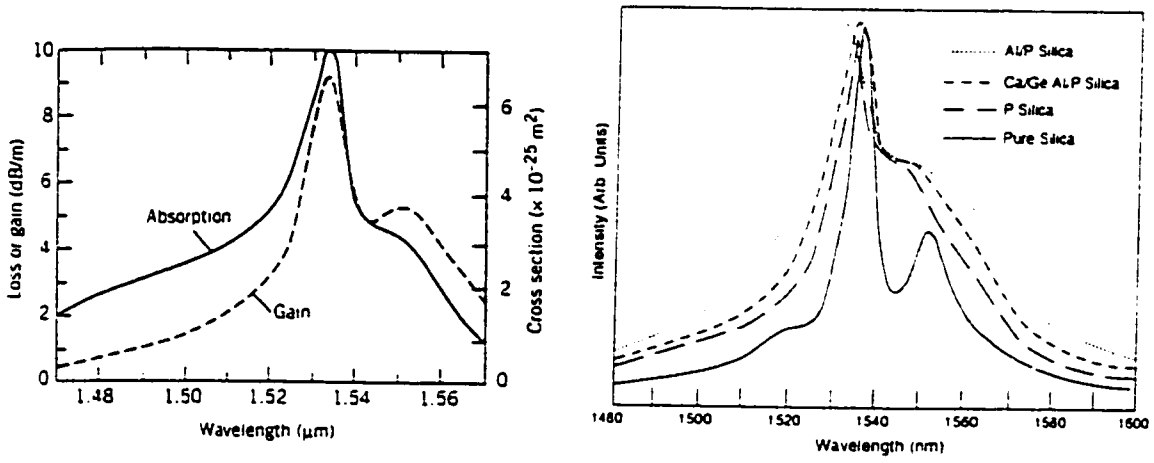

(a) (b)

Figure 2.7 (a) Absorption and gain spectra of an erbium doped germania fiber (b)Emission spectra of four EDF with different core compositions

2.5 Theoretical Model

Two main ingredients of a laser are a gain medium that provide amplification and a suitable cavity that provides optical feedback. To obtain an efficient EDFL, the design of laser cavity, including output coupler ratio, doped fiber, and cavity loss is very important. There have been a few models to characterize the behavior of EDFLs [54-56], however, their expressions for operating characteristics are in terms of fiber and atomic parameters,

such as the erbium atom density, the excited-state spontaneous lifetime, emission cross-section and absorption cross-section. Measurement of these parameters is time consuming. The paper by Pfeiffer et. al. [57] is an exception, but he did not give optimization of fiber parameters. In the next two sections, we derive analytical expressions for an erbium doped fiber ring laser, including laser threshold, output power, slope efficiency, and optimum length of EDF. These expressions are based on cavity loss, coupler ratio, and easily measured fiber data, i.e., saturation powers, and small signal absorption coefficients.

2.5.1 Rate Equations

The theoretical model that we consider is based on a basic fiber ring configuration, depicted in Fig. 2.8. The gain medium is a piece of EDF with a length of L. For pump wavelengths that are free from ESA, the propagation of pump and signal waves could be described by a set of equations that only take into account the population of the upper laser level ($^4I_{13/2}$) and the lower laser level ($^4I_{15/2}$) of the erbium ions. The rate equation for the population of the upper level N_2 and the amplification or attenuation of the local intensity I_k are described by

$$\frac{\partial N_2}{\partial t} = -\frac{N_2}{\tau} - \sum_{j=p,s} u_j \frac{1}{h\nu_j}\frac{\partial I_j}{\partial z} \tag{2.1}$$

$$\frac{\partial I_k}{\partial z} = u_k I_k (N_2\sigma_k^{em} - N_1\sigma_k^{abs}) = u_k I_k (N_2(\sigma_k^{em} + \sigma_k^{abs}) - N\sigma_k^{abs}) \tag{2.2}$$

Here u_j indicates the direction of propagation of the pump ($j = p$) and signal wave ($j = s$): u_j = +1 for positive z-direction, u_j = -1 for negative z-direction. τ is the upper level spontaneous lifetime, $h\nu_j$ the photon energy, σ_k^{em} and σ_k^{abs} the emission and absorption

cross section respectively, and subscript k stands for either p for pump beam or s for signal beam.

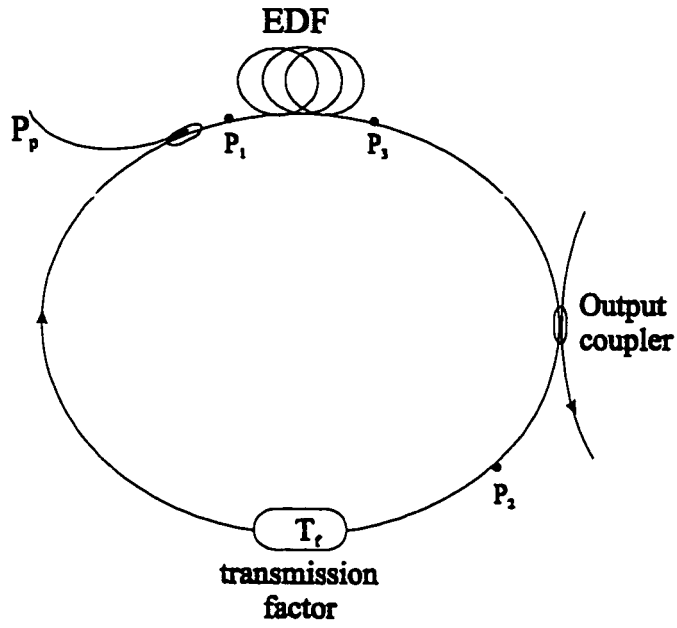

Figure 2.8 Schematic diagram of an EDFL

In equilibrium, from Eq.(2.1) the population of the upper level is

$$N_2 = -\tau \sum_{j=p,s} u_j \frac{1}{h\nu_j} \frac{\partial I_j}{\partial z} \tag{2.3}$$

By inserting Eq. (2.3) into (2.2), and integrating it over the fiber cross section, then the change of power in a pump beam or signal beam is given by

$$\frac{\partial P_k}{\partial z} = -u_k P_k (\alpha_k + \frac{1}{P_k^{sat}} \sum_{j=p,s} u_j \frac{\lambda_j}{\lambda_k} \frac{\partial P_j}{\partial z}) \tag{2.4}$$

with the small signal absorption coefficient

$$\alpha_k = \rho \Gamma_k \sigma_k^{abs} \tag{2.5}$$

and the saturation power

$$P_k^{sat} = \frac{h\nu_k A}{\Gamma_k(\sigma_k^{em} + \sigma_k^{abs})\tau} \tag{2.6}$$

where ρ is the erbium ion density within the active volume of cross sectional area A. Γ_k is the overlap integral between the erbium distributions.

2.5.2 Operating Characteristics

In this section, we will examine a few important parameters characterizing a fiber ring EDFL, which include output power, laser threshold, slope efficiency, and optimum length of EDF.

Integration of Eq. (2.4) over the length L of the EDF yields

$$\ln\left[\frac{P_k(L)}{P_k(0)}\right] = -u_k\left\{\alpha_k L + \frac{1}{P_k^{sat}}\sum_j \frac{\lambda_j}{\lambda_k} u_j\left[P_j(L) - P_j(0)\right]\right\} \tag{2.7}$$

Let P_p and P_s denote the pump power and the laser signal power. The corresponding values of u_j in Eq.(2.7) are 1 and 1, as the ring laser operates unidirectionally, the backward signal power has been neglected. Assume that the single-pass gain for the EDF is G, which gives

$$P_s(L) = GP_s(0) \tag{2.8}$$

Then, Eq. (2.7) can be simplified as:

$$P_s(L) = P_s(0)\exp(-\alpha_s L + \frac{g}{P_s^{sat}}) \tag{2.9}$$

$$P_p(L) = P_p(0)\exp(-\alpha_p L + \frac{g}{P_p^{sat}} \cdot \frac{\lambda_s}{\lambda_p}) \tag{2.10}$$

where

$$g = \frac{\lambda_p}{\lambda_s}\left[P_p(0) - P_p(L)\right] - \left[P_s(L) - P_s(0)\right] \tag{2.11}$$

or, from Eqs.(2.8) and (2.9):

$$g = P_s^{sat}(\alpha_s L + \ln G) \tag{2.12}$$

Now, referring back to Fig. 2.8, during a round trip, the laser cavity has a total cavity loss

$$\delta_{cav} = \frac{P_3}{P_1} = \frac{1}{T_f R} \tag{2.13}$$

where R is the reflectivity of the output coupler, and T_f is the transmission factors describing the round trip loss from P_2 to P_1 in the passive fiber cavity.

The gain G between P_1 to P_3 is determined by the well-known threshold condition:

$$G = \frac{1}{T_f R} \tag{2.14}$$

By solving Eqs. (2.8-14), one can obtain the intra-cavity circulating laser power $P_s(L)$ at the end of EDF:

$$P_s(L) = \frac{1}{1 - RT_f}\left\{\frac{\lambda_p}{\lambda_s} P_p(0)\left[1 - \frac{P_p(L)}{P_p(0)}\right] - g\right\} \tag{2.15}$$

2.5.2.1 Output Power

A fraction of the circulating power $P_s(L)$ is transmitted from the output coupler as the output power. Hence we can write the output power as

$$P_{out} = (1 - R) \cdot P_s(L) \tag{2.16}$$

therefore

$$P_{out} = \frac{1 - R}{1 - RT_f}\left\{\frac{\lambda_p}{\lambda_s} P_p(0)\left[1 - \exp(-\alpha_p L - (\alpha_s L - \ln RT_f) \cdot \frac{P_s^{sat}}{P_p^{sat}} \cdot \frac{\lambda_s}{\lambda_p})\right] - P_s^{sat}(\alpha_s L - \ln RT_f)\right\}$$

Eq. (2.17)

This equation shows how the laser output power depends on the pump power, the length of the EDF, and other parameters associated with the passive cavity (i.e., R, T_f) and the EDF (i.e., α_p, P_p^{sat}, α_s, P_s^{sat}).

2.5.2.2 Threshold and Slope efficiency

The threshold pump power can be found by setting $P_{out} = 0$. The slope efficiency is a measure of efficiency with which the laser converts pump power into the output power once it has reached threshold. By rewriting Eq. (2.17) as

$$P_{out} = \eta_s [P_p(0) - P_{th}] \tag{2.18}$$

then, the threshold pump power and the slope efficiency turn out to be

$$P_{th} = \frac{\lambda_s}{\lambda_p} \cdot \frac{P_s^{sat}(\alpha_s L - \ln RT_f)}{1 - \exp[-\alpha_p L - (\alpha_s L - \ln RT_f) \cdot \frac{P_s^{sat}}{P_p^{sat}} \cdot \frac{\lambda_s}{\lambda_p}]} \tag{2.19}$$

$$\eta_S = \frac{1-R}{1-RT_f} \frac{\lambda_p}{\lambda_s} P_p(0) \left[1 - \exp(-\alpha_p L - (\alpha_s L - \ln RT_f) \cdot \frac{P_s^{sat}}{P_p^{sat}} \cdot \frac{\lambda_s}{\lambda_p}) \right] \tag{2.20}$$

2.5.2.3 Optimum length of EDF

The effect of pump decay along the EDF results in non-uniform medium inversion. Since the medium is absorbing laser signal when not inverted, the fiber becomes lossy at laser wavelengths beyond a certain length. Therefore, for a given pump power, there is an optimum length L_{opt} of the EDF that maximizes the output power.

From Eq.(2.9-2.10), one can obtain the ratio of the residual pump power to pump power

$$\frac{P_p(L)}{P_p(0)} = G^{\varepsilon} \exp[(\varepsilon \alpha_s - \alpha_p) \cdot L] \tag{2.21}$$

where

$$\varepsilon = \frac{P_s^{sat}}{P_p^{sat}} \cdot \frac{\lambda_s}{\lambda_p} \tag{2.22}$$

Combining Eqs.(2.12), (2.14), (2.15), and (2.16) yields the output power in another form

$$P_{out} = \frac{1}{1 - RT_f} \left\{ \frac{\lambda_p}{\lambda_s} P_p(0) \left[1 - (T_f R)^{-\varepsilon} \exp(\varepsilon\alpha_s - \alpha_p) \cdot L \right] - P_s^{sat} \left[\alpha_s L - \ln(T_f R) \right] \right\} \tag{2.23}$$

By using the condition $\frac{dP_{out}}{dL} = 0$, we can find the optimum length of EDF:

$$L_{opt} = \frac{1}{(\varepsilon\alpha_s - \alpha_p)} \cdot \left\{ \ln\left[\frac{\varepsilon\alpha_s P_p^{sat}}{(\alpha_p - \varepsilon\alpha_s) P_p(0)} \right] + \varepsilon \ln(T_f R) \right\} \tag{2.24}$$

2.6 Summary

This chapter describes the basic principle of an erbium doped fiber laser (EDFL), including reviews of fiber lasers, merit of fiber lasers, as well as EDFL. The analytical expressions of operating characteristics such as output power, threshold, slope efficiency, and optimum length of EDF have been derived, based on the rate equations.

2.6 References

1. E. Snitzer, *Phys. Rev. Lett.*, "Optical master action of Nd^{3+} in a barium crown glass", vol.7, pp.444-446, 1961.
2. E. Snitzer and R. Woodcock, "Yb^{3+}-Er^{3+} glass laser", *Appl. Phys. Lett.*, vol.6, pp.45-46, 1965.
3. F.W. Quelle, *SPIE Seminar on Laser Range Instrumentation*, El Paso, TX, 1967.

4. J.P. Segre, *Proc. Electro-Optics Conf.*, Montreux, Switzerland, 1974.

5. J. Stone and C.A. Burrus, "Neodymium-doped fiber lasers: room temperature cw operation with an injection laser pump", *Appl. Opt.*, vol.13, pp.1256-1258, 1974.

6. R.J. Mears, L. Reekie, S.B. Pole, and D.N. Payne, "Neodymium-doped silica single-mode fibre lasers", *Electron. Lett.*, vol.21, pp.738-740, 1985.

7. I.P. Alcock, A.I. Ferguson, D.C. Hanna, and A.C. Tropper, "Tunable, continuous-wave neodymium-doped monomode-fiber laser operating at 0.900-0.945 and 1.070-1.135 μm", *Opt. Lett.*, vol.11, pp.709, 1986.

8. M. Shimizu, H. Suda and M. Horiguchi, "High efficiency Nd-doped fibre lasers using direct-coated dielectric mirrors", *Electron. Lett.*, vol.23, pp.768-769, 1987.

9. I. Liu, M. Digonnet, K. Fesler, B.Y. Kim, and H.J. Shaw, "Broadband diode-pumped fibre laser", *Electron. Lett.*, vol.24, pp.838-840, 1988.

10. W.J. Barnes, S.B. Poole, J.E. Townsend, L. Reekie, D.J. Taylor, and D.N. Payne, "Er^{3+}-Yb^{3+} and Er^{3+} doped fiber lasers", *J. Lightwave. Technol.*, vol. 7, pp.1461-1465, 1989.

11. I.N. Duling, L. Goldberg, and J.F. Weller, "High-power mode-locked Nd:fiber laser pumped by an injection-locked diode array," *Electron. Lett.*, vol. 24, pp.1333-1335, 1988.

12. G.T. Maker, and A.I. Ferguson, "1.56 μm Yb-sensitised Er fiber laser pumped by diode-pumped Nd:YAG and Nd:YLF lasers," *Electron. Lett.*, vol. 24, pp.1160-1162, 1988.

13. A.E. Siegman, *Lasers*, University Science Books, Mill Valley, CA, 1986

14. P.w. Milonni and J.H. Eberly, *Lasers*, Wiley, New York, 1988

15. R.J. Mears, L. Reekie, S.B. Poole, and D.N. Payne, "Lower threshold tunable CW and Q-switched fibre laser operating at 1.55 μm", *Electron. Lett.*, vol.22, pp.159-160, 1986.

16. C.A. Millar, I.D. Miller, B.J. Ainslie, S.P. Craig and J.R. Armitage, "Low-threshold CW operation of an erbium-doped fiber laser pumped at 807 nm wavelength", *Electron. Lett.*, vol.23, pp.865-866, 1987.

17. L. Reekie, I.M. Jauncey, S.B. Poole and D.N. Payne, "Diode-laser-pumped operation of an Er^{3+}-deoped single-mode fibre laser", *Electron. Lett.*, vol.23, pp.1076-1078, 1987.

18. D.C. Hanna, R.M. Percival, I.M. Perry, R.G. Smart, and A.C. Trooper, "Efficient operation of an Yb-sensitised Fr fibre laser pumped in 0.8 μm region", *Electron. Lett.*, vol.24, pp.1068-1069, 1988.

19. R. Wyatt, B.J. Ainslie, and S.P. Craig, "Efficient operation of array-pumped Er^{3+}-deoped silica fibre laser at 1.5 μm," *Electron. Lett.*, vol. 24, pp.1362-1363, 1988.

20. W.L. Barnes, P.R. Morkel, L. Reekie, and D.N. Payne, "High-quantum-efficiency Er^{3+} fiber lasers pumped at 980 nm", *Opt. Lett.*, vol. 14, pp.1002-1004, 1989.

21. J. Zhang and J.W.Y. Lit, "Erbium-doped fiber compound ring laser with a right filter", *IEEE Photon. Technol. Lett.*, vol. 6, pp.588-590, 1994.

22. C.X. Shi, "A novel twisted Er-doped fiber ring laser: proposal, theory, and experiment," *Opt. Communication*, vol.125, pp.349-358, 1996.

23. P. Barnsely, P. Urquhart, C. Millar, and M. Brierley, "Fiber Fox-Smith resonators: application to single-longitudinal-mode operation of fiber laser", *J. Opt. Soc. Am. A.*, vol.5, pp.1339-1346, 1988.

24. G.A. Ball, W.W. Morey and W.H. Glenn, "Standing-wave monomode erbium fiber laser", *IEEE Photon. Technol. Lett.*, vol. 3, pp.613-615, 1991.

25. J.L. Zyskind, V. Mizrahi, D.J. DiGiovanni and J.W. Sulhoff, "Short single frequency erbium-doped fiber laser", *Electron. Lett.*, vol. 28, pp.1385-1387, 1992.

26. G.A. Ball and W.W. Morey, "Continuously tunable single-mode erbium fiber laser", *Opt. Lett.*, vol. 17, pp.420-422, 1992.

27. V. Mizrahi, D.J. DiGiovanni, R.M. Atkins, S.G. Grubb, Y.K. Park and J.M.P. Delavaux, "Stable single-mode erbium fiber-grating laser for digital communication", *J. Lightwave Technol.*, vol. 11, pp.2021-2025, 1993.

28. D.I. Chang, M.J. Guy, S.V. Chernikov, J.R. Taylor and H.J. Kong, "Single-frequency erbium fibre laser using the twisted-mode technique," *Electron. Lett* vol.32, pp.1786-1787, 1996.

29. J.L. Zyskind, J.W. Sulhoff, Y. Sun, J. Stone, L. W. Stulz, G.T. Harvey, D.J. DiGiovanni, H.M. Presby, A.Piccirilli, U. Koren, and R.M. Jopson, "Singlemode diode-pumped tunable erbium-doped fibre laser with linewidthe less than 5.5 kHz", *Electron.Lett.*, vol. 27, pp.2148-2149, 1991.

30. C. V. Poulsen and M. Sejka, "Highly optimized tunable Er^{3+}-doped single longitudinal mode fiber ring laser, experiment and model," *IEEE Photon. Technol. Lett.*, vol. 5, pp.646-648, 1993.

31. A. Gloag, N. Langford, K. McCallion and W. Johnstone, "Continuously tunable single-frequency erbium ring fiber laser," *J. Opt. Soc. Am. B*, vol.13, pp.921-925, 1996.

32. J. Zhang, C.Y. Yue, G.W. Schinn, W.R.L. Clements, and J.W.Y. Lit, "Stable single-mode compound-ring erbium-doped fiber laser," *J. Lightwave Technol.* vol.14, pp.104-109, 1996.

33. C.C. Lee, Y.K. Chen and S.K. Liaw, "Single-longitudinal-mode fiber laser with a passive multiple-ring cavity and its application for video transmission," *Opt. Lett.*, vol. 23, pp.358-360, 1998.

34. G.J. Cowle and D.N. Payne, "Single-frequency travelling-wave erbium-doped fibre loop laser," *Electron. Lett.*, vol. 27, pp.229-230, 1991.

35. A.J. Gloag, N. Langford, I. Bennion and L. Zhang, "Single-frequency travelling-wave erbium doped fibre laser incorporating a fibre Bragg grating," *Opt. Communication*, vol. 123, pp.553-557, 1996.

36. M.J. Guy, J.R. Taylor and R. Kashyap, "Single-frequency erbium fibre ring laser with intracavity phase-shifted fibre Bragg grating narrowband filter," *Electron.Lett.*, vol.31, pp.1924-1925, 1995.

37. Y.Cheng, J.T. Kringlebotn, W.H. Loh, R.I. Laming, and D.N. Payne, "Stable single-frequency traveling-wave fiber loop laser with integral saturable-absorber-based tracking narrow-band filter," *Opt. Lett.*, vol. 20, pp.875-877, 1995.

38. T. Komukai and M. Nakazawa, "Tunable single frequency erbium doped fiber ring lasers using fiber grating etalons", *Jpn. Appl. Phys.*, vol. 34, pp.L679-680 , 1995.

39. K.O. Hill, Y. Fuji, D.C. Johnson, B.S. Kawasaki, "Photosensitivity in optical fiber waveguides: application to reflection filter fabrication", *Appl. Phys. Lett.*, vol.32, pp.647-649, 1978.

40. G. Meltz, W.W. Morey, and H.W. Glenn, "Formation of Bragg gratings in optical fibers by a transverse holographic method," *Opt. Lett.*, vol. 14, pp.823-825, 1989.

41. G.A. Ball, W.H. Glenn, W.W. Morey, and P.K. Cheo, "Modeling of short, single-frequency, fiber lasers in high-gain fiber," *IEEE Photon. Technol. Lett.*, vol.5, pp.649-651, 1993.

42. M. Svalgaard and S.L. Gibert, "Stability of short, single-mode erbium-doped fiber lasers," *Appl. Opt.*, vol. 36, pp.4999-5005, 1997.

43. J.L. Zyskin, V. Mizrahi, D.J. DiGiovanni and J.W. Sulhoff, *Electron.Lett.*., vol. 28, pp.1385-1387, 1992.

44. F. Sanchez, P. LeBoudec, P.L. Francois, and G. Stephan, "Effects of ion pairs on the dynamics of erbium-doped fiber lasers", *Phys. Rev. A.*, vol. 48, pp.2220-2229, 1993.

45. J.T. Kringlebotn, P.R. Morkel, L. Reekie, J.L. Archambault, and D.N. Payne, "Efficient diode-pumped single-frequency erbium : ytterbium fiber laser," *IEEE Photon. Technol. Lett.*, vol. 5, pp.1162-1164, 1993.

46. K. Hsu, W.H. Loh, L. Dong, and C.M. Miller, "Efficient and tunable Er/Yb fiber grating lasers," *J. Lightwave Technol.*, vol. 15, pp.1438-1441, 1997.

47. G.A. Ball, G. Hull-Allen, and W.W. Morey, "20-mw single-frequency integrated fiber MOPA with active noise reduction," in Technical Digest *OFC'94*, vol.4, p.22, 1994.

48. G.A. Ball, G. Hull-Allen, and W.W. Morey, "60 mW 1.5 μm single-frequency low-noise fiber laser MOPA," *IEEE Photon. Technol. Lett.*, vol. 6, pp.192-194, 1994.

49. J.E. Townsend, W.L. Barnes, K.P. Jedrzejewski, and S.G. Grubb, "Yb sensitised Er doped silica optical fiber with ultrahigh transfer efficiency and gain," *Electron.Lett.*, vol.27, pp.1958-1959, 1991.

50. Y. Shi, M. Seijka, and O. Poulsen, "A unidirectional Er^{3+}-doped fiber ring laser without isolator", *IEEE Photon. Technol. Lett.*, vol. 7, pp.290-292, 1995.

51. Y. Hua and J. Conradi, "Single-polarization wavelength-tunable fiber laser with a nonreciprocal cavity", *J. Lightwave Technol.*, vol. 13, pp.1913-1918, 1995.

52. Y. Kimura and M. Nakazawa, "Lasing characteristics of Er^{3+}-doped silica fibers from 1553 up to 1603 nm", *J. Appl. Phys.*, vol.64, pp.516-520, 1988.

53. W.J. Miniscalco, L.J. Andrews, B.A. Thompson, R.S. Quimby, L.J.Vacha, and M.G. Drexhage, "1.3 μm fluoride fibre laser", *Electron. Lett.*, vol. 24, pp.28-29, 1988.

54. J.Chen, X. Zhu, and W. Sibbett, "Derivation of the threshold pump power of erbium-doped fiber lasers", *Opt. Lett*, vol. 17, pp.926-928, 1992.

55. M. Mignon, E. Desurvire, "An analytical model for the determination of optimal output reflectivity and fiber length in erbium-doped fiber lasers", *IEEE Photon. Technol. Lett.*, vol. 4, pp.850-852, 1992.

56. P. Franco, M. Midrio, A. Tozzato, M. Romagnoli, and F. Fontana, "Characterization and optimization criteria for filterless erbium-doped fiber lasers", *J. Opt. Soc. Am. B.*, vol. 11, pp.1090-1097, 1994.

57. Th. Pfeiffer, H. Schmuch, and H. Bulow, "Output power characeristics of erbium-doped fiber ring lasers", *IEEE Photon. Technol. Lett.*, vol. 4, pp.847-859, 1992.

Chapter 3

Fiber ring resonators with an external reflector

As we have mentioned in chapter 1, the design of laser cavity is a key step in building a fiber laser with good performance. Various configurations based on two types of cavities, linear FP cavity and ring cavity, have been reviewed in chapter 1. Among these designs unidirectional fiber ring lasers have been particularly attractive, because they have excellent lasing efficiency, and are able to eliminate back scattering and spatial hole-burning effects. Consequently, these lasers have better potential to achieve single-longitudinal mode oscillations. Ring-structure erbium-doped fiber laser with transmission-type filters, such as FP filter [1], Mach-Zehnder interferometer (MZT) [2], and ring filter [3] have been demonstrated. Compared with fiber Bragg grating (FBG) filter [4], these filters are expensive and complicated. Unfortunately, FBG is a reflection-type filter. Recently, the loop-structure (Sagnac-type geometry) erbium-doped fiber laser [5-7] has attracted much attention because it allows the use of FBG as a filter in a traveling-wave cavity.

Conventionally, one or more optical isolators (OI) are included to force the wave propagation unidirectional. However, such isolators will introduce additional destructive losses and increase the costs. More recently, unidirectional erbium-doped fiber ring lasers without optical isolators have been reported [8-9]. In one case, nonreciprocal operation

was achieved by an S-shape feedback loop formed by two couplers [8]; in the other case a combination of polarization splitter and output coupler was used [9].

In this chapter, we present a new resonator design for a fiber laser to achieve unidirectional operation by using an external reflector, which may be a FBG. Such a scheme has two advantageous. First unidirectional operation can be achieved without the use of an OI. Second it allows the use of reflection-type FBG in a ring structure.

This chapter is divided into three sections. The first section describes the principle of operation of the resonator. The second section deals with the directionality analysis of the resonator, for determining how to choose the coupler coefficient to favor one direction over the other. In the third section, the resonator is analyzed to find the characteristics of the resonator.

3.1 Principle of operation

Figure 3.1 shows the basic structure of the fiber ring resonator with an external reflector (FRRER). It is just a simple fiber ring resonator (FRR), with a reflector inserted at one end of the coupler. This reflector introduces some very interesting properties to the resonator.

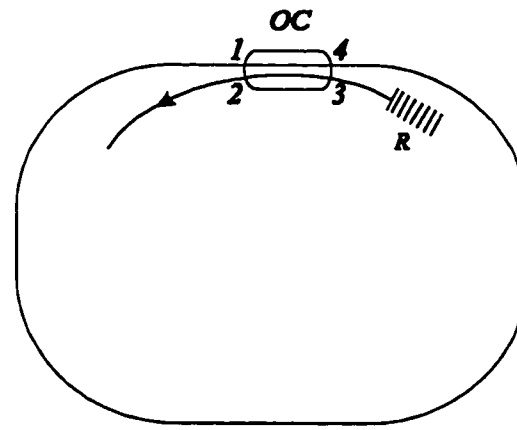

Figure 3.1 Schematic of FRRER.
OC: output coupler; R:end reflector.

Because the resonator will be used to construct lasers, a piece of fiber with a gain medium, for instance an erbium-doped fiber (EDF), is added to the ring as in Fig. 3.2.

Suppose the EDF is pumped by a 980-nm or 1480-nm laser diode. Below the lasing threshold, the amplified spontaneous emission travels around the ring cavity in two directions, clockwise (cw) and counter clockwise (ccw) directions. At the output coupler (OC), the ccw wave in port 4 is partly coupled into port 2 and leaves the ring as output; the other part propagates to port 1 and, after traveling around the ring, is returned to port 4. The cw wave is divided into two parts by the OC; part of it proceeds from port 1 to port 4 and then returns to port 1 again; the other part that is coupled into port 3 is reflected by a reflector and returned partly to port 2 as output and partly to port 1 as a ccw wave. Because of this latter injection of wave into the ccw direction from a wave that is originally traveling in the cw direction, some nonreciprocal losses between the two directions are introduced into the ring cavity, which may ensure unidirectional oscillation in the ccw direction without the need of an OI.

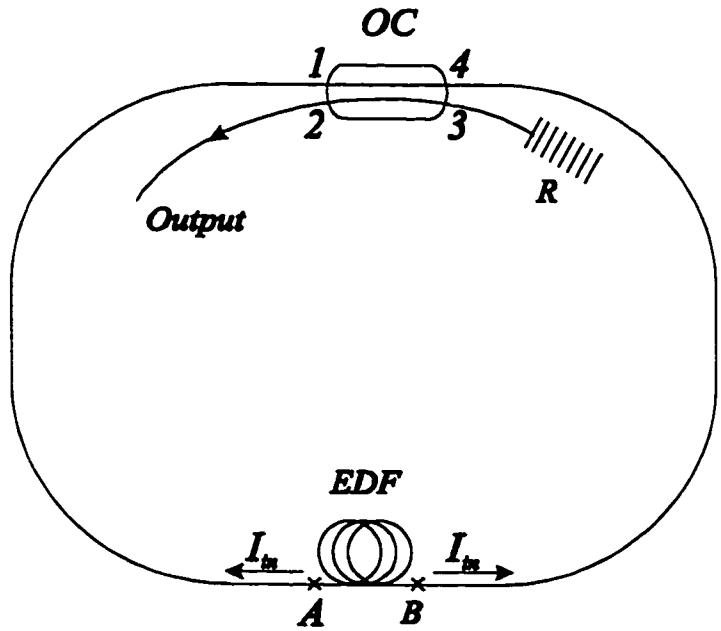

Figure 3.2 Configuration of FRRER with EDF.
OC: output coupler; *R*: reflector;*EDF*: Er^{3+}-doped fiber.

3.2 Directionality Analysis

In the previous section, we have described how by means of an external reflector, nonreciprocal loss may be achieved for the cw and ccw directions. In this section, we will explore the directionality property of FRRER by calculating the loss difference (*LD*). *LD* is defined as

$$LD = 10\log(\frac{RI_{ccw}}{RI_{cw}}) \tag{3.1}$$

where RI_{ccw} and RI_{cw} are the resultant intensities for the ccw and cw directions, respectively. Obviously, it is desirable to have a big *LD* in order to achieve a better unidirectional performance. By following the propagation of a ray in Fig.3.2, we calculate the *LD*. Let us consider that the same amount of light intensity I_{in} is launched at points A and B in the cw and ccw directions, where the light is caused by amplified spontaneous emission (ASE), generated in the EDF below lasing threshold. We trace the light in the two directions and calculate the returned intensities at point A as RI_{ccw} and at point B as RI_{cw}. As no circulating intensity exists from point A to B or B to A, it is ready to write *LD* as

$$LD = 10\log\left[\frac{k^2(1-\gamma)^2 r}{1-k}+1\right] \tag{3.2}$$

where r is the reflectivity of the end reflector; k and γ are the intensity coupling coefficient and coupler intensity loss coefficient, respectively. Eq. (3.2) can also be derived as in appendix B.

Figure 3.3 shows how the loss difference depends on the coupler coefficient k and the coupler loss γ. The reflectivity of the end reflector is assumed to be 100%. It can be seen that the *LD* increases with increasing k, while the coupler loss slightly degrades the *LD*.

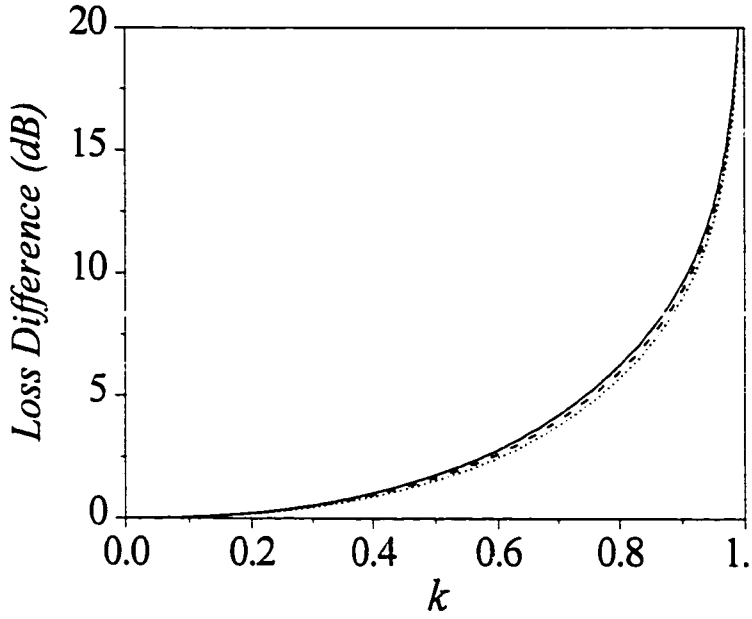

Figure 3.3 Loss difference as a function of the coupler coefficient for various values of coupler losses. Solid line: γ=0; dash line: γ=0.04; dotted line: γ=0.08.

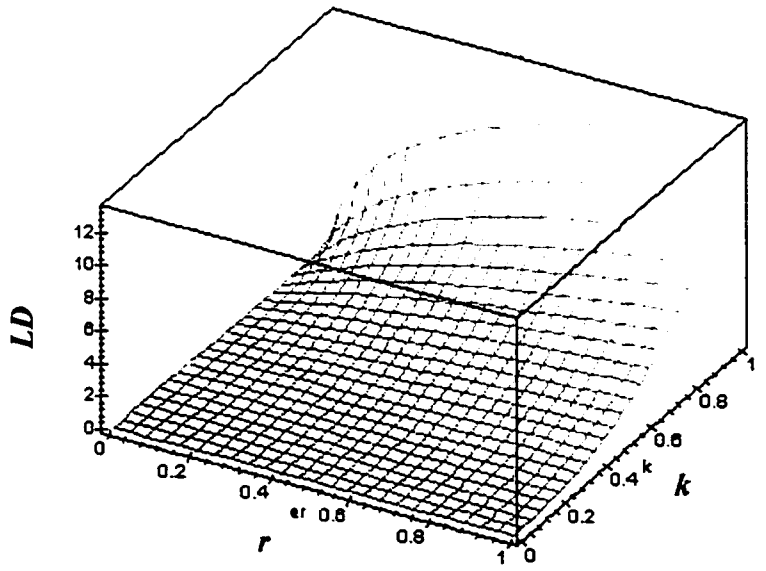

Figure 3.4 Loss difference as a function of the coupler coefficient and the reflectivity of the external reflector with $\gamma = 0.02$.

On the other hand, the influence of the end reflector on the loss difference is very important. It is clear from Fig.3.4 that high LD can be obtained when both R and k are high, whereas high R is critical and required, since LD tends to 0 (i.e., equal loss in both directions) as $R \to 0$, no matter how high k is.

It can be noted in Fig. 3.2 that part of the cw light is coupled into the ccw direction by the reflector while the ccw light offers no contribution to the cw direction. As a result, the loss difference between the two directions arises, which depends on the parameters of the coupler as shown in Fig.3.3. Thus, lasing oscillation would be favored in the ccw direction, provided the EDF is a homogeneously broadened material. It is well known that the line-broadening of an EDF has both homogeneity and inhomogeneity [10-11]. Fortunately, at room temperatures, the homogeneous linewidth of EDF is about 2 nm [8]. Therefore, if the linewidth of the end reflector is chosen to be less than 2 nm, such principle should work. This has being proved in our experiment in chapter 5, where a unidirectional operation was achieved with a high power difference (~37dB) between the two directions.

3.3 Resonance Analysis

It is well known that the resonance properties of a resonator may be evaluated by assuming that an input field E_{in} is launched into the cavity through one of the two ports of the output coupler. For a general ring resonator, either of the two ports may be chosen to inject the input to analyze the resonator since lights in cw and ccw directions are reciprocal. However, the FRRER in Fig. 3.1 is a nonreciprocal resonator, as discussed in section 3.1-3.2, therefore two cases, in which light is separately injected into the two ports of the output coupler, should be considered. Case I has light circulating only in the

ccw direction shown in Fig. 3.5(a), where the light is launched into port 3. Case II has light circulating in both cw and ccw directions, as shown in Fig.3.5(b); in this case, the light is launched into port 2. Both cases describe the state when the laser is first turned on. Because of the nonreciprocal loss difference in the two directions, ultimately case II will evolve into case I and lasing will be favored in the ccw direction.

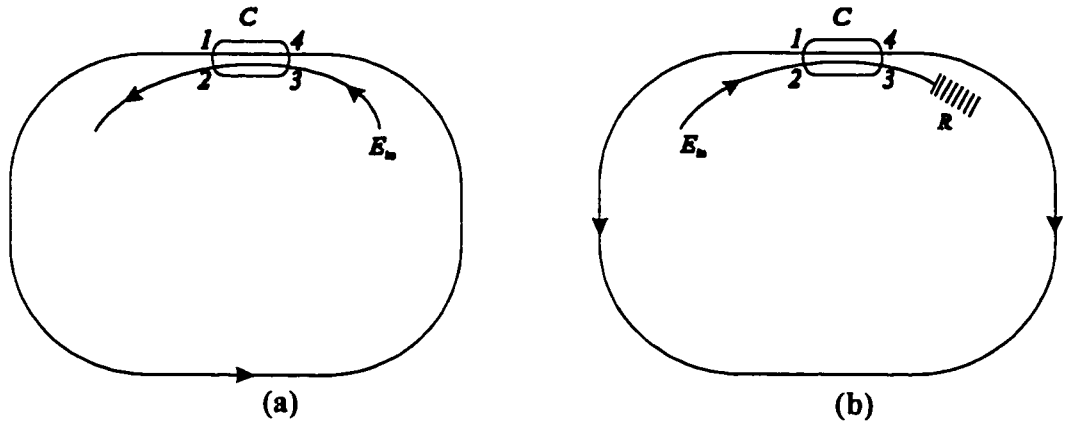

Figure 3.5 Schematic for resonance analysis (a) Case I (b) Case II
R: end reflector; *C*: coupler; E_{in}: input field.

3.3.1 Case I

The schematic diagram of case I is shown in Fig.3.5(a). It is a single-coupler FRR, formed by splicing the two directional ports of the coupler *C*. The ports of the coupler are numbered as 1 to 4 in counter-clockwise manner starting from the left. When input light is launched into port 3, part of the input light comes out as an output, and the other part circulates inside of the fiber ring. The coupler has an intensity coupling coefficient k and intensity loss γ, and the fiber ring has a cavity length l and a splice loss ξ.

By using coupled-mode equations for the fiber coupler and the propagation relations along the fibers, one can find the output electric field and circulating electric

fields, which are given in appendix C1. It is noted that for simplicity of analysis, we've made a few assumptions as follows.

1. Coupler and fiber are polarization-maintaining so that the complex electric fields can be treated as scalars.
2. The coupler has zero length, no backward reflection, and it is reciprocal, i.e., coupling ratio from port 1 to 4 is the same as from port 4 to 1.
3. The coupler is frequency independent.
4. Input light intensity is always low so that nonlinearities may be ignored.

From the electric fields, one can obtain in a straightforward manner the normalized output and circulating intensities:

$$I_{1a} = \left|\frac{E_{1a}}{E_{in}}\right|^2 = \frac{b^2}{(1-ap)^2 + 4ap\sin^2(\delta/2)} \tag{3.3}$$

$$I_{2a} = \left|\frac{E_{2a}}{E_{in}}\right|^2 = \frac{[a-(1-\gamma)p]^2 + 4a(1-\gamma)p\sin^2(\delta/2)}{(1-ap)^2 + 4ap\sin^2(\delta/2)} \tag{3.4}$$

For simplicity, we have set

$$p = e^{-(\alpha l+\xi)} \tag{3.5}$$

$$q = e^{i\delta} \tag{3.6}$$

$$\delta = \beta \cdot l \tag{3.7}$$

Where p, δ, and β are the transmission factor, the phase change for a round trip of the fiber ring, and the propagation constant, respectively.

For a weakly guiding fiber, β can be expressed approximately as

$$\beta \approx \frac{2\pi n\nu}{c} \tag{3.8}$$

where n is the refractive index in the fiber core, ν is the frequency of the light coupled into the cavity, and c is the velocity of light in vacuum.

In Eqs.(3.3)-(3.4), I_{2a} and I_{1a} describe the output intensity and circulating intensity, respectively. When the fiber ring is at perfect resonance, all the energy should be circulating inside the ring and no energy comes out. Then we could set $I_{2a} = 0$ in Eq. (3.4); this will give us the optimum resonance conditions, which are

$$k_{opt} = 1 - p^2 \cdot (1 - \gamma) \tag{3.9}$$

$$\delta = \beta \cdot l = 2m\pi \tag{3.10}$$

where Eq.(3.9) and Eq.(3.10) are respectively, the amplitude condition and the phase condition for resonance; and the subscript *opt* in Eq.(3.9) denotes optimum. In the following, we will examine the properties of the resonator and give some computed results.

3.3.1.1 Frequency response

Figures 3.6(a) and 3.6(b) show the frequency responses of I_{2a} and I_{1a} with coupling coefficient k as a parameter. Obviously, the resonator behaves like a FP, except that it has a channel-dropping response. At optimum resonance, the circulating intensity reaches maximum and the output intensity reaches minimum. When k departs from k_{opt}, the circulating intensity decreases and the output intensity increases; when $k < k_{opt}$, the curves become sharper, and it becomes broader for $k > k_{opt}$.

3.3.1.2 Effects of losses

The frequency responses of the intensities with different transmission factors are shown in Fig.3.7. The coupling coefficients are chosen to be the optimum value k_{opt}, in

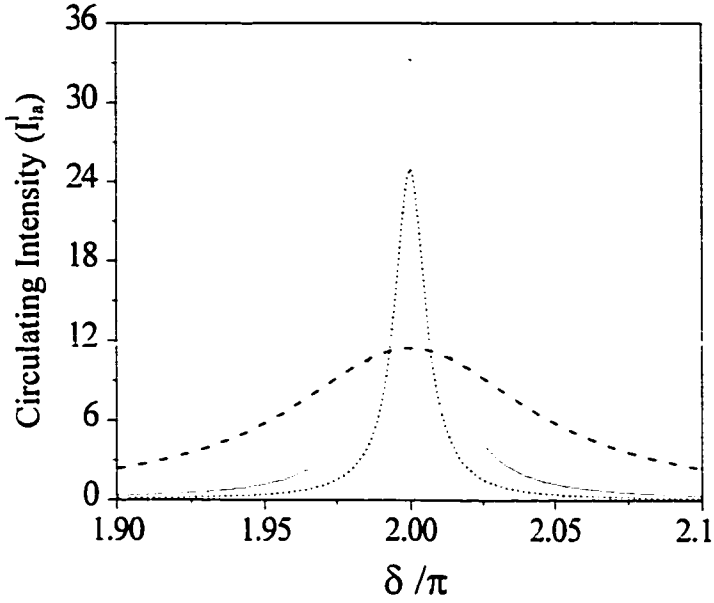

(a)

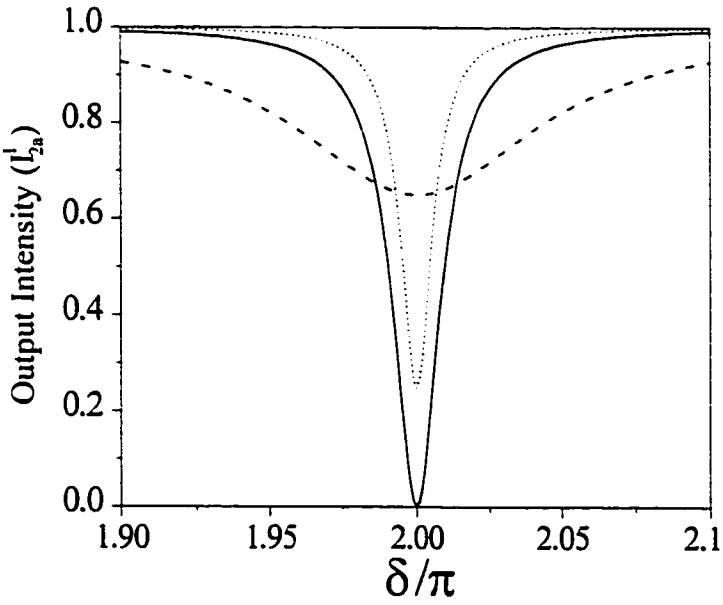

(b)

Figure 3.6 Frequency responses of (a) circulating intensity (b) and output intensity with the coupling coefficient k as a parameter. Solid: $k = k_{opt} = 0.029$; dotted: $k = 0.01$; dashed: $k = 0.25$. Other parameters are $\gamma = 0.01$, $p = 0.99$, and $r = 0.99$.

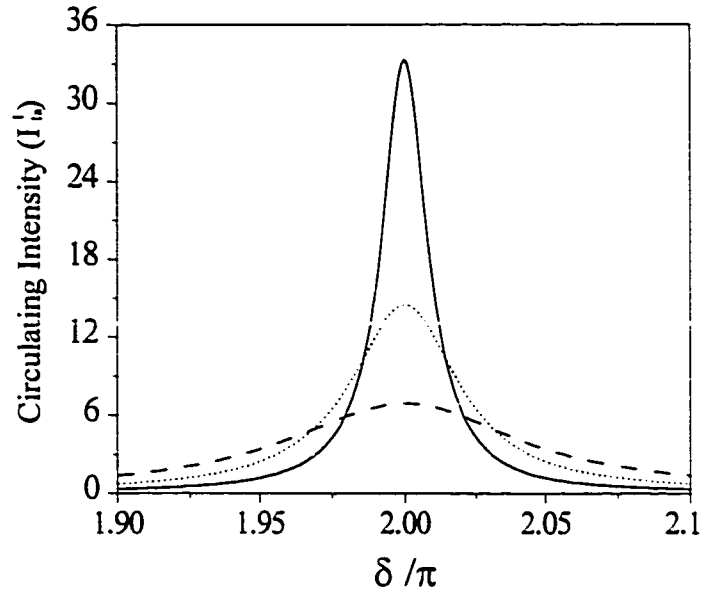

(a)

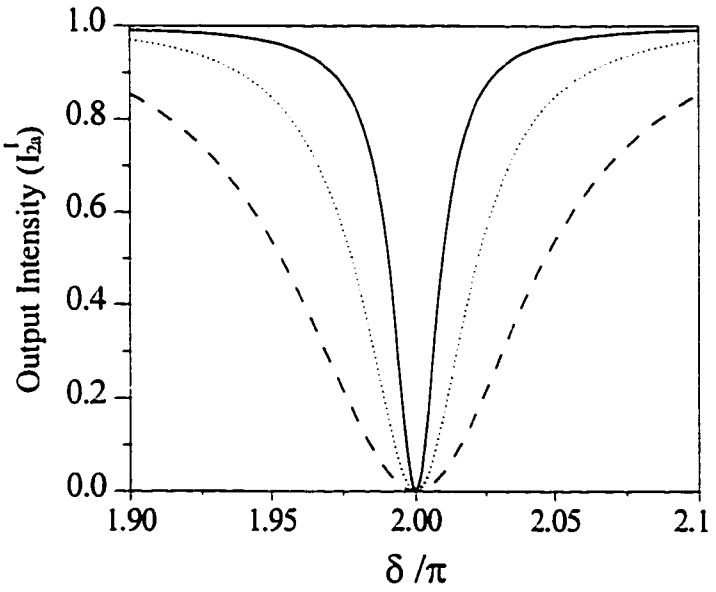

(b)

Figure 3.7 Frequency responses of (a) circulating intensity (b) and output intensity with the transmission factor p as a parameter. Solid: $p = 0.99$; dotted: $p = 0.97$; dashed: $p = 0.95$. Other parameters are $\gamma = 0.01$ and $r = 0.99$.

order to isolate the effect of the transmission factor since k_{opt} greatly depends on the transmission factor, as seen in Eq.(3.9). From Fig.(3.7), it can be seen that the transmission factor degrades the properties of the resonator by decreasing the circulating intensity and increasing the linewidth of curves, and consequently the finesse of the resonator.

3.3.2 Case II

Figure 3.5(b) shows the configuration for Case II. It is a FRRER, formed by a FRR with an external reflector spliced to port 3. The input light launched into port 2 is partly coupled into port 4 while another part is coupled into port3. This latter part is reflected by the reflector. Part of the reflected light comes out as an output, and the other part joins the circulating light in the ccw direction. The input light at port 4 will form the circulating light in the cw direction.

The normalized circulating intensities and the output intensity can be obtained from the electric fields, which are derived in appendix C2:

$$I_{4a} = \left|\frac{E_{4a}}{E_{in}}\right|^2 = \frac{b^2}{(1-ap)^2 + 4ap\sin^2(\delta/2)} \tag{3.11}$$

$$\begin{aligned} I_{1a} &= \left|\frac{E_{1a}}{E_{in}}\right|^2 = \frac{b^2 r^2 p_0^2}{(1-ap)^2 + 4ap\sin^2(\delta/2)}\ I_{3a} \\ &= b^2 r^2 p_0^2\ \frac{[a-(1-\gamma)p]^2 + 4a(1-\gamma)p\sin^2(\delta/2)}{[(1-ap)^2 + 4ap\sin^2(\delta/2)]^2} \end{aligned} \tag{3.12}$$

$$I_{2a} = \left|\frac{E_{2a}}{E_{in}}\right|^2 = r^2 p_0^2 (I_{3a})^2 = r^2 p_0^2\ \left[\frac{[a-(1-\gamma)p]^2 + 4a(1-\gamma)p\sin^2(\delta/2)}{[(1-ap)^2 + 4ap\sin^2(\delta/2)]}\right]^2 \tag{3.13}$$

with

$$p_0 = e^{-(\alpha l_0 + \xi_0)} \tag{3.14}$$

where p_0 and ξ_0 are the transmission factor and the splicing loss of the fiber between port 3 and the reflector.

In the above equations, I_{2a}, I_{4a}, and I_{1a} represent the output intensity, and the circulating intensities in the cw and ccw directions, respectively.

The intensities in Eqs.(3.11)-(3.13) can also be conceptually obtained from another approach. That is to transform the resonator in Fig.3.5(b) to an unfolded equivalent model as shown in Fig.3.8.

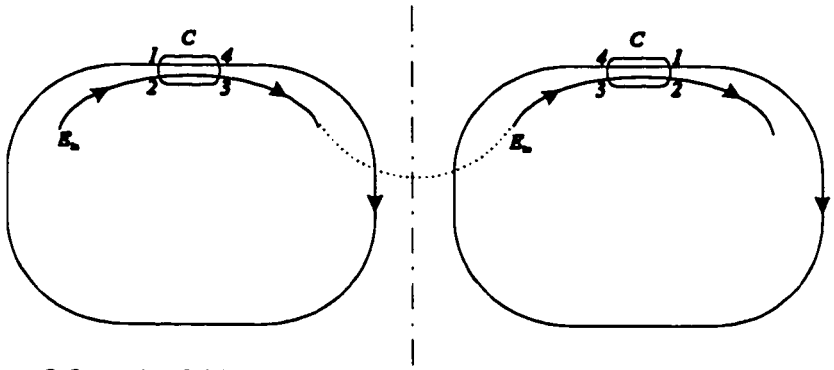

Figure 3.8 Unfolded equivalent model of the configuration in Case II. The right-hand side of the dash line is a mirror image of the left-hand side.

Consider the input light which leaves port 3 as shown in Fig.3.5(b). When it reaches the end reflector, instead of being reflected back to port 3, it will serve as an input in the mirror image of the resonator as shown in Fig.3.8. Therefore, for a systematic presentation, the normalized output intensity and circulating intensities in the ccw direction should be I_{2a}, I_{1a} in the image resonator of the right side. Based on the results in case I, one can write these intensities as:

$$I_{2a}^{II} = r^2 p_0^2 (I_{3a}^{II})^2 = r^2 p_0^2 (I_{2a}^{I})^2 \tag{3.15}$$

$$I_{1a}^{II} = r^2 p_0^2 I_{3a}^{II} I_{4a}^{II} = r^2 p_0^2 I_{2a}^{I} I_{1a}^{I} \tag{3.16}$$

and also have:

$$I_{4a}^{II} = I_{1a}^{I}, \quad I_{3a}^{II} = I_{2a}^{I} \tag{3.17}$$

where the superscript I and II in Eqs.(3.15)-(3.17) denotes case I and II, respectively. Obviously, the intensities obtained by direct derivation and simple equivalent model are identical.

By setting $I_{2a} = 0$ in Eq.(3.13) or $I_{2a} = 0$ in Eq.(3.15), the optimum conditions are found to be the same as in case I, which is expected from Eq.(3.15). In the same way as in case I, we will explore the characteristics of case II, together with a comparison between the two cases.

3.3.2.1 Frequency response

Figure 3.9 shows the frequency response of the circulating intensity I_{1a}^{II} in the ccw direction with four different coupling coefficients. It can be seen that the shape of the curve can change from a quasi-channel-passing type to a channel-dropping type under certain conditions. At the optimum value k_{opt}, the intensity of the resonant curve is of a quasi-channel-dropping type with a profound dip and zero intensity. The depth of the dip decreases when k increases, and the curve becomes a channel-passing type with a flat top at $k = 0.16$. If k increases further, the flat top disappears, and the shape of the resonator curves is similar to the shape of the circulating intensity I_{1a}^{I} or I_{4a}^{II}.

As mentioned in section 3.13, when such a resonator (in case II) is used to construct a laser, both case I and case II are used to describe the state below the threshold. Then, the resultant circulating intensity in the ccw direction I_{1a}^{T} should be the superimposition of I_{1a}^{I} on I_{1a}^{II}. That will lead to a high circulating intensity and narrow linewidth, for example, if k is chosen to be 0.25 (see Fig.3.6 and Fig.3.9), compared with

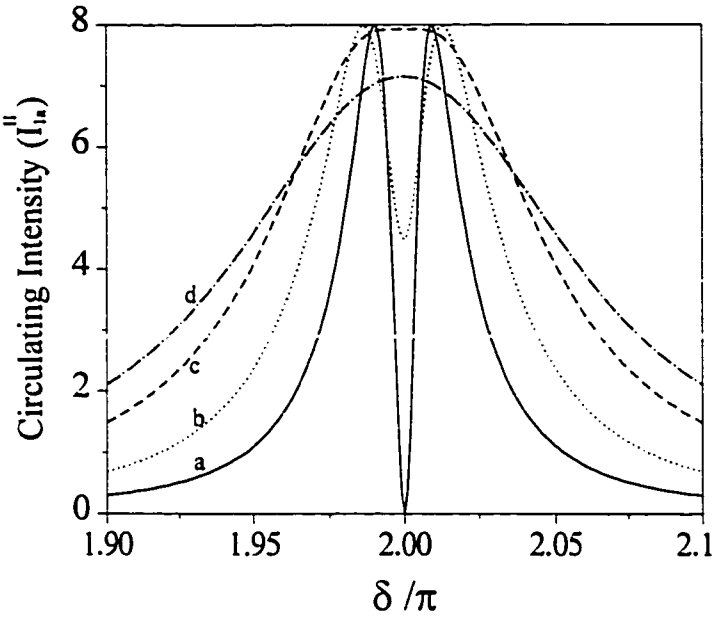

Figure 3.9 Frequency response of the circulating intensity I_{1a}^{II} with different coupling coefficient. a: $k = k_{opt} = 0.029$; b: $k = 0.09$; c: $k = 0.16$; d: $k = 0.25$. Other parameters are $\gamma = 0.01$, $p = 0.99$ and $r = 0.99$.

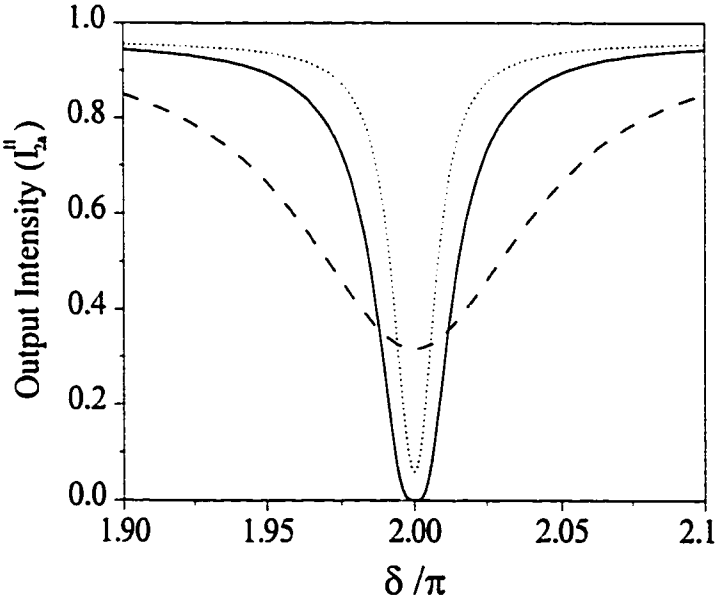

Figure 3.10 Frequency response of the output intensity I_{2a}^{II} with different coupling coefficient. Solid: $k = k_{opt} = 0.029$; dotted: $k = 0.01$; dashed: $k = 0.2$.

FRR with the circulating intensity of I_{1a}^{I} only. It is well known that high circulating intensity and narrow linewidth are desirable for lasers. Therefore, the single fiber ring resonator with an external reflector will give a better performance, compared with the single fiber ring resonator.

The frequency response of the circulating intensity I_{4a}^{II} in the cw direction has the same curve as the circulating intensity I_{1a}^{I} in case I from Eq.(3.17), shown in Fig.3.6(a).

The resonant curve of the output intensity as a function of the coupling coefficient k is shown in Fig.3.10. It has a behavior similar to that in Case I. The difference between the two cases will be given the next sub-section.

In Figs. (3.9) and (3.10), we have kept the reflectivity r of the reflector constant at 0.99. The reflector plays an important role in that it offers the resonator a loss difference in the two directions as discussed in section 3.1, and also special resonant characteristics. From Eqs.(3.15)-(3.16), it can be seen that when r decreases, I_{2a}^{II} and I_{1a}^{II} will decrease as r^2. When r is zero, case II becomes identical to case I.

3.3.2.2 Comparison between Case I and Case II

Case I and II become different when an end reflector is added to the resonator. Then the circulating intensity I_{1a}^{II} in the ccw direction is generated in case II while it is absent in case I. The curve of I_{1a}^{II} is fairly dependent on the coupling coefficient, as shown in Fig.3.9.

Although the curves of the output intensity in the two cases are quite similar, they have different characteristics in intensity and finesse. The finesse of the fiber resonator is

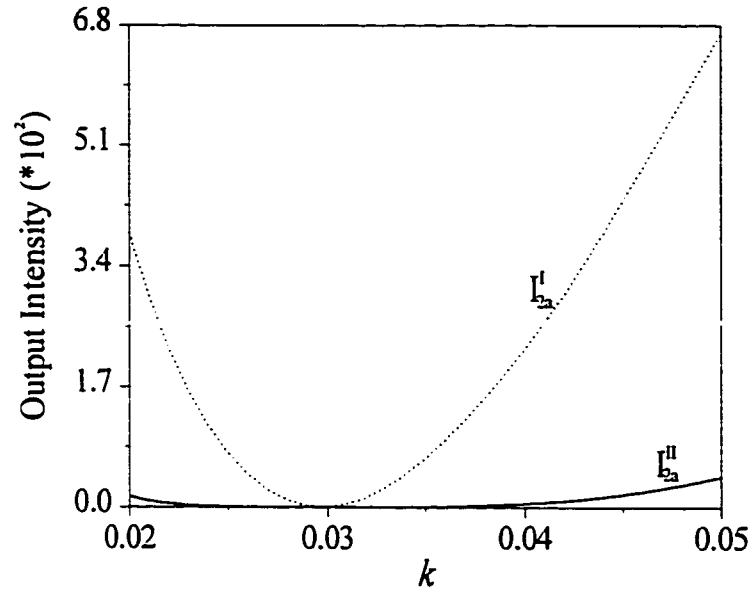

(a)

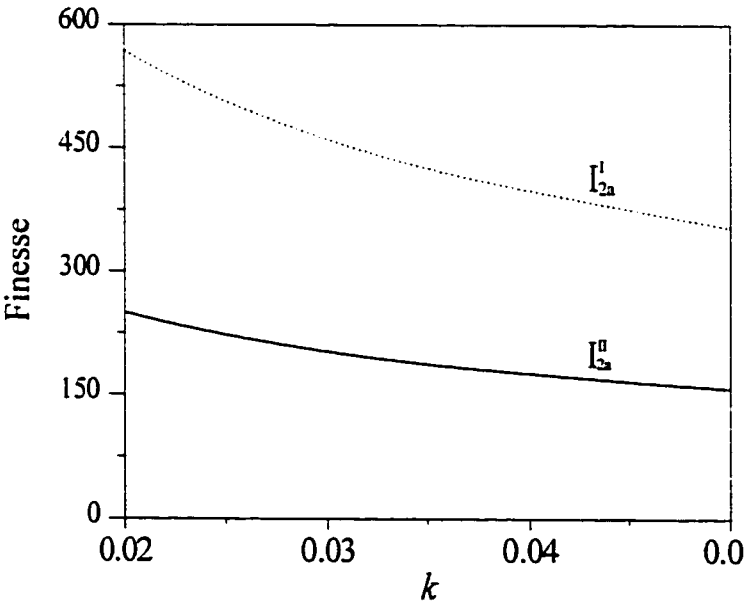

(b)

Figure 3.11 (a) Output intensity (b) and finesse as a function of the coupling coefficient k. Solid: Case I; dashed: Case II. $k_{opt} = 0.0297$. Other parameters are $\gamma = 0.01$, $p = 0.99$ and $r = 0.99$.

defined as the ratio of the resonance peak spacing to the full width at half maximum (FWHM). Figures 3.11(a) and (b) show the output and finesse as functions of the coupling coefficient in the two cases. Figure 3.11(a) tells us that the output intensity in case II is less sensitive to the deviation of k_{opt}, compared with case I. This property may be very useful in practical applications. This is because k_{opt} greatly depends on transmission factor, which is unpredictable when the coupling coefficient is chosen. However, the finesse will degrade in case II by 2 times. Therefore, there is a tradeoff between the two cases when used as a filter.

3.4 Summary

We have reported a fiber ring resonator with an end reflector (FRRER). Such a resonator has a loss difference between the clockwise and counter-clockwise directions. Consequently, if it is used as a laser resonator, unidirectional operation may be obtained without one or more optical isolators. A directionality analysis is studied in terms of the loss difference, by assuming that the same amount of light is launched into the cw and ccw directions. To comprehend the properties of the passive resonator for lasers, we have analyzed the FRRER and the FRR, which are referred to as case II and case I, respectively. The optimum conditions and intensities in terms of the coupling coefficient and the losses are investigated. It is found that the optimum conditions are the same and the intensities in the two cases are correlated, which can be better understood from its unfolded equivalent model. When the coupling coefficient departs from the k_{opt}, the curves of the circulating intensities (I_{1a}^{I} and I_{1a}^{II}) in the two cases have Lorentzian shapes. Therefore, compared with the FRR, the resultant circulating intensity ($I_{1a}^{I} + I_{1a}^{II}$)

in the FRRER will lead to a higher circulating intensity and narrower linewidth. They are desirable properties when the resonator is used in lasers.

3.5 References:

1. J.L. Zyskind, J.W. Sulhoff, Y. Sun, J. Stone, L. W. Stulz, G.T. Harvey, D.J. DiGiovanni, H.M. Presby, A.Piccirilli, U. Koren, and R.M. Jopson, "Singlemode diode-pumped tunable erbium-doped fibre laser with linewidthe less than 5.5 kHz", *Electron.Lett.*, vol. 27, pp.2148-2149, 1991.
2. Y.T. Chieng and R.A. Minasian, "Tunable erbium-doped fiber laser with a reflection Mach-Zehnder interferometer", *IEEE Photon. Technol. Lett.*, vol.6, pp.153-156, 1994.
3. J. Zhang, C.Y. Yue, G.W. Schinn, W.R.L. Clements, and J.W.Y. Lit, "Stable single-mode compound-ring erbium-doped fiber laser," *J. Lightwave Technol.*, vol.14, pp.104-109, 1996.
4. C.R. Giles, "Lightwave application of fiber Bragg gratings", *J. Lightwave Technol.*, vol. 15, pp.1391-1404, 1997.
5. A.J. Gloag, N. Langford, I. Bennion and L. Zhang, "Single-frequency travelling-wave erbium doped fibre laser incorporating a fibre Bragg grating," *Opt. Communication*, vol.123, pp.553-557, 1996.
6. Y.Cheng, J.T. Kringlebotn, W.H. Loh, R.I. Laming, and D.N. Payne, "Stable single-frequency traveling-wave fiber loop laser with integral saturable-absorber-based tracking narrow-band filter," *Opt. Lett.*, vol. 20, pp.875-877, 1995.
7. T. Komukai and M. Nakazawa, "Tunable single frequency erbium doped fiber ring lasers using fiber grating etalons", *J. Appl. Phys.*, vol. 34, pp.L679-680, 1995.

8. Y. Shi, M. Seijka, and O. Poulsen, "A unidirectional Er^{3+}-doped fiber ring laser without isolator", *IEEE Photon. Technol. Lett.*, vol. 7, pp.290-292, 1995.
9. Y. Hua and J. Conradi, "Single-polarization wavelength-tunable fiber laser with a nonreciprocal cavity", *J. Lightwave Technol.*, vol. 13, pp.1913-1918, 1995.
10. J.L. Zyskind, E. Desurvire, J.W. Sulhoff and D.J. DiGiovanni, "Determination of homogeneous linewidth by spectral gain hole-burning in an erbium-doped fiber amplifier with GeO_2:SiO_2 core:", *IEEE Photon. Technol. Lett.*, vol.2, pp.869-871, 1990.
11. M.J. Weber, "Fluorescence and glass lasers", *J. Non-Crystalline Solids*, vol.47, p.117, 1982.

Chapter 4

Compound Ring Resonator with an external reflector

4.1 Introduction

Optical fiber-based ring resonators with one or multiple couplers [1-8] have many practical applications in fiber lasers, optical filters, and fibre sensor systems. When an optical resonator is used in single-frequency fiber lasers or densely spaced optical frequency division multiplexing (OFDM) systems, a large free spectral range (*FSR*) is required for mode suppression and more channels. In chapter 3, we have described and discussed FRRER including FRR. These resonators are single ring resonators. When they are used in practical laser systems, it is unavoidable to have a cavity length tens of meters long, because of the inclusion of a number of intracavity elements, such as polarization controller and wavelength multiplexing coupler. Obviously, the long cavity length will give a small *FSR*, which would cause multiple-mode oscillations and mode hopping problems.

In order to increase the FSR to relieve these problems, double-ring resonators [4-8] are the best choice to achieve large *FSR* with vernier effect. Different configurations of vernier filters based on the combination of fiber couplers, fiber rings, and in-line amplifier have been reported. Urquhart [4] proposed a vernier fiber ring resonator composed of two single-ring resonators in tandem. Oda et al. [5] and Barbarossa et al. [6]

suggested compound double-ring resonators based on three couplers with improved characteristics. Also Ja [7] reported S-shape double-ring double-loop resonator and degenerate two wave mixing. The output fields of these resonators offer channel-passing response, acting as a transmission filter for applications in OFDM systems.

On the other hand, when a resonator is used in a doped fiber laser, high circulating field with a channel-passing response is required for better mode suppression. Zhang et al. [8] reported a three-coupler compound resonator by inserting a double-coupler fiber ring (DCFR) into the main resonator ring. It has been used to make single-longitudinal-mode fiber lasers [10]. Although this resonator performs well in a fiber ring laser, the insertion loss of the mode filter DCFR is quite high (about 2 dB) [10]. This is because it is difficult to choose the exact coupler coefficient to realize the amplitude resonance condition of DCFR; thus, part of energy leaks out of the other port of the DCFR as loss.

In this chapter, we propose a double-coupler compound ring resonator (CRR), whose *FSR* can be increased by vernier operation. It is simple and easy to make with only two couplers. Moreover, with the insertion of an external grating, such a resonator may be readily used to construct a unidirectional ring laser without the use of an optical isolator.

In section 4.2, we will present a new basic double-coupler CRR. To analyse the proposed CRR, first, the expressions of output intensity and circulating intensities of the CRR are given. Optimum design relationships for resonance can be determined from the output intensity. Based on the intensities and the resonance conditions, the characteristics of the resonator are investigated in terms of coupling coefficient, losses and resonant number, including frequency response, mode suppression and reduction factor.

Section 4.3 will be focused on the double-coupler compound ring resonator with an external reflector (CRRER). First the principle of the CRRER is described. Next the properties of the directionality are investigated to see how the coupling coefficient affects the loss difference. Finally, the resonance analysis of the proposed CRRER is presented.

4.2 Basic Compound Ring Resonator

Figure 4.1 shows the schematic diagram of the proposed CRR, which incorporates two directional couplers. It has two ring cavities, which share a common fiber segment L_2. The primary ring (ring p) has a total length $L_p = L_2+L_3$, and the second ring (ring s) has total length $L_s = L_1+L_2$. The ports of each coupler are numbered in a counter-clockwise manner. The two couplers have intensity coupling coefficients k_1 and k_2, respectively. Port 3 is chosen as the input port, from which the input energy circulates as travelling wave in both of the two ring cavities, and the output comes out from port 8. For simplicity, the couplers and fibers hold the same assumption as those in chapter 3.

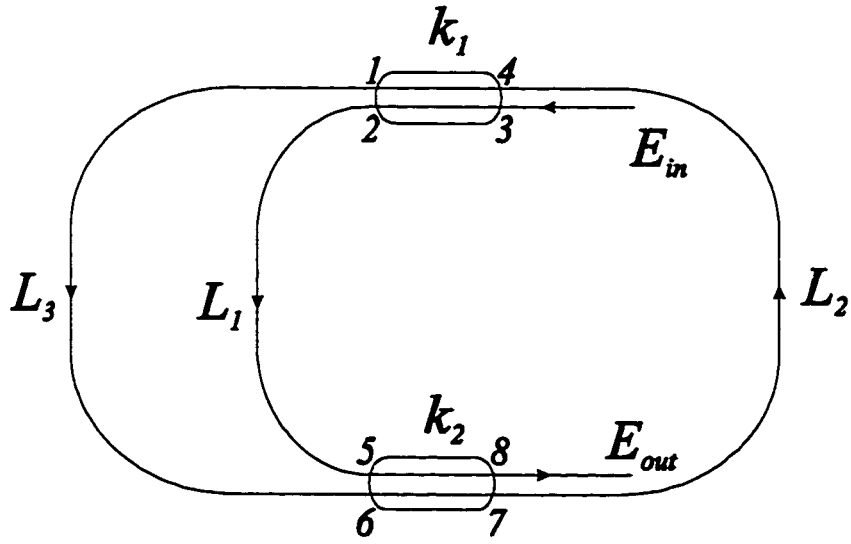

Figure 4.1 The schematic diagram of the CRR

4.2.1 Output and Circulating Intensities

The output and circulating fields of the resonator can be derived by using the same method in Chapter3, and are given in appendix D1. The normalized output and circulating intensities, i.e., the products of the relative fields and their complex conjugates, can be expressed as:

$$\begin{aligned} I_{8a} = \{ & [a_1 a_2 p_s - b_1 b_2 p_p - p_s p_p (1-\gamma_1)(1-\gamma_2)]^2 \\ & + 4a_1 a_2 b_1 b_2 p_s p_p \sin^2[(\delta_p - \delta_s)/2] \\ & + 4a_1 a_2 p_s^2 p_p (1-\gamma_1)(1-\gamma_2)\sin^2(\delta_p/2) \\ & - 4b_1 b_2 p_s p_p^2 (1-\gamma_1)(1-\gamma_2)\sin^2(\delta_s/2)\} / p_2^2 I_d \end{aligned} \tag{4.1}$$

$$I_{1a} = \{[b_1 + b_2 p_s (1-\gamma_1)^2] - 4b_1 b_2 p_s \sin^2(\delta_s/2)\} / I_d \tag{4.2}$$

$$\begin{aligned} I_d = & (1 - a_1 a_2 p_p + b_1 b_2 p_s)^2 + 4a_1 a_2 p_p \sin^2(\delta_p/2) \\ & - 4b_1 b_2 p_s \sin^2(\delta_p/2) + 4a_1 a_2 b_1 b_2 p_s p_p \sin^2[(\delta_p - \delta_s)/2] \end{aligned} \tag{4.3}$$

with

$$\delta_s = \beta L_s \tag{4.4}$$

$$\delta_p = \beta L_p \tag{4.5}$$

where δ_p and δ_s are the phase changes in ring p and ring s.

The output and circulating intensities as functions of the phase change of the second ring are shown in Fig. 4.2. It is obvious that the curves of the output and circulating intensities are of channel-blocking and channel-passing types, respectively. From Eqs.(4.1)-(4.2) it is clear that the output and circulating intensities of the CRR depend on the coupler coefficients of the two directional couplers. The optimum design of the coupler coefficients will be given in following subsection.

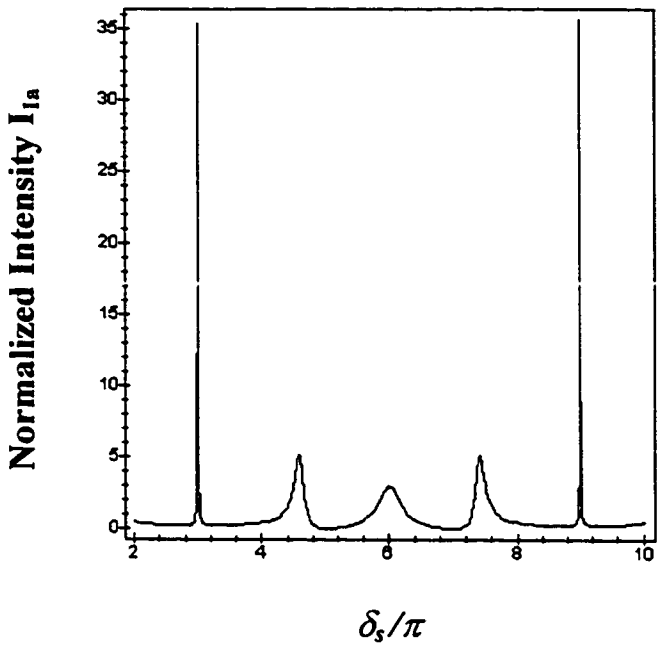

(a)

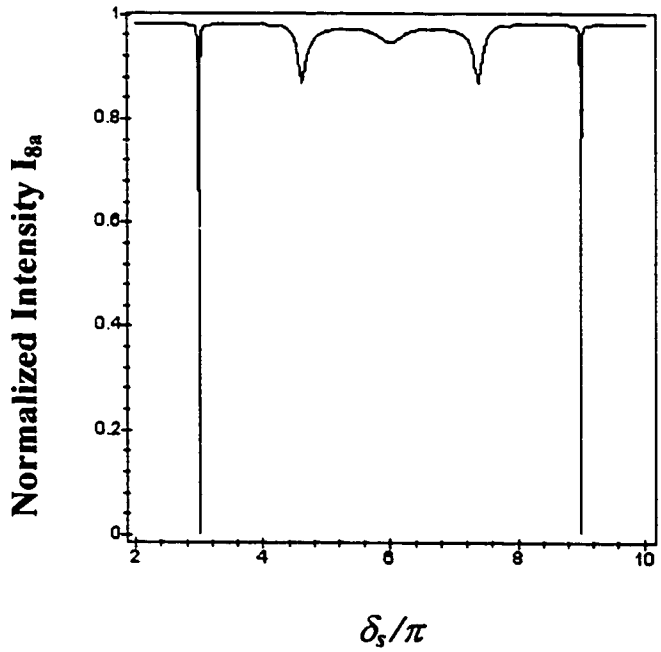

(b)

Figure 4.2 Spectral response function for (a) I_{1a}, (b) I_{8a} as function of the optical phase δ_s/π. Coupler losses, $\gamma_1=\gamma_2=0.5\%$; Transmission factors, $p_s=p_p=0.995$. Lengths of rings: $L_p=4\ m$ and $L_s=3\ m$.

4.2.2 Resonance Condition

The resonator conditions can be obtained by setting the output field E_{8a} in Eq. (C.9) or intensity in Eq.(4.1) to zero. The phase resonance conditions are expressed as

$$\delta_p = 2m\pi \tag{4.6}$$

$$\delta_s = 2n\pi + \pi \tag{4.7}$$

where m and n are positive integers. The additional phase of π in Eq.(4.7) is introduced into the optical wave because it crosses the couplers twice in a round trip in the second ring. Results identical to Eqs.(4.6)-(4.7) may be obtained by using the fact that the optical wave is in phase with the original wave after circulating one complete turn.

By solving the equation

$$a_1 a_2 p_s - b_1 b_2 p_p = p_s p_p (1-\gamma_1)(1-\gamma_2) \tag{4.8}$$

the amplitude resonance condition can be written as

$$k_{2r}^{A,B} = p_s^2 \left[\sqrt{(1-k_1)k_1 A} \mp k_1 p_p^2 \sqrt{(1-\gamma_1)\cdot(1-\gamma_2)}\right]^2 \Big/ k_1 (k_1 p_s^2 - k_1 p_p^2 - p_s^2)^2 \tag{4.9}$$

with

$$A = \gamma_1 p_s^2 p_p^2 + \gamma_2 p_s^2 p_p^2 + k_1 p_p^2 - k_1 p_s^2 - \gamma_1 \gamma_2 p_s^2 p_p^2 - p_s^2 p_p^2 + p_s^2 \tag{4.10}$$

where the subscript r in Eq.(4.9) denotes resonance.

From Eq.(4.9) it can be seen that there are two optimum values k_{2r}^{A} and k_{2r}^{B} for k_1, referred to as A-resonance and B-resonance, respectively. The dependence of the optimum values of $k_{2r}^{A,B}$ on k_1 with different transmission factors is plotted in Fig.4.3 with Eq.(4.9). Figure 4.3 shows that $k_{2r}^{A} < k_{2r}^{B}$ for the same value of k_1 and losses, and $k_{2r}^{A,B}$ change noticeably with k_1, and $k_{2r}^{A,B}$ is strongly dependent on the transmission factors.

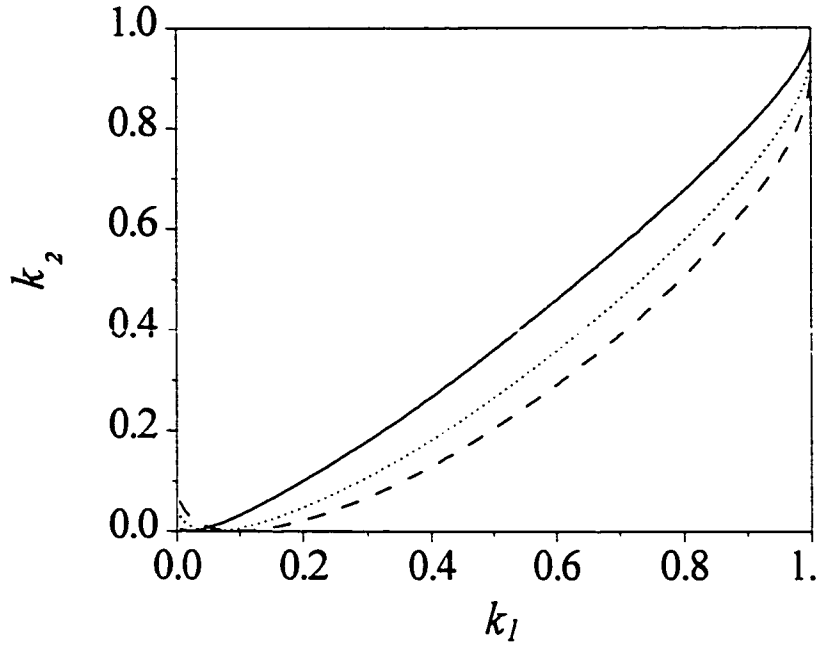

(a)

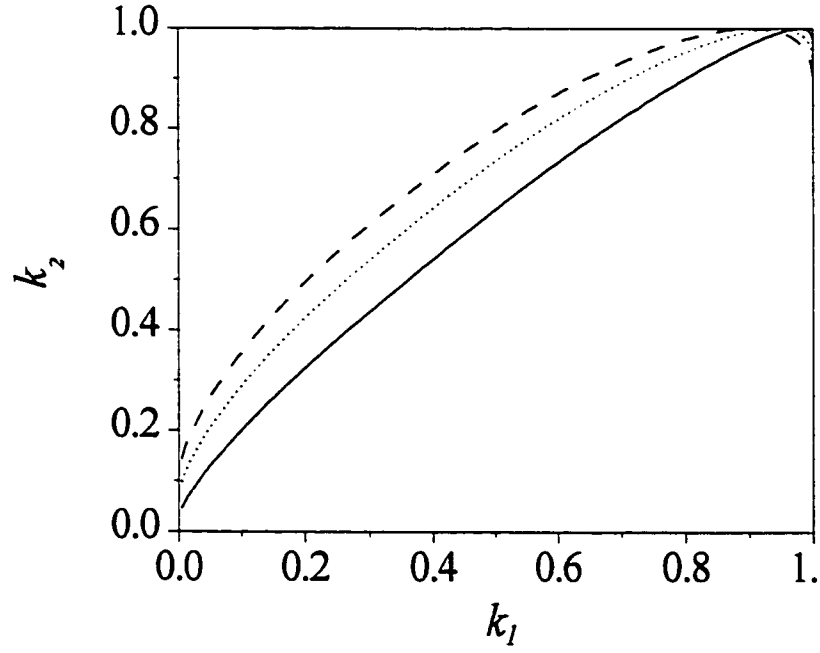

(b)

Figure 4.3 Optimum values of k_2 as functions of k_1 for different transmission factors with $\gamma_1=\gamma_2=1\%$. Solid: $p_s=p_p=1$; Dotted: $p_s=p_p=0.98$; Dashed: $p_s=p_p=0.96$.
(a) A-resonance (b) B-resonance

In the next section, we shall present computed results under A-resonance and B-resonance, and discuss the various characteristics of the resonator and the influences of different parameters on them.

4.2.3 Computed Results and Discussion

Figure 4.4(a) and 4.4(b) are three-dimension plots of the circulating intensity as a function of k_1 and the phase change of the secondary ring under A- and B-resonances. It can be seen that under both resonances the circulating intensity decreases as k_1 increases, but A-resonance has a higher circulating intensity than B-resonance, and also the circulating intensity changes with k_1 slightly more slowly in case A- than in case B-resonance.

4.2.3.1 Away from Optimum Value and effects of loss

In Fig. 4.4, the optimum values $k_{2r}^{A,B}$ have been used for all values of k_1. When the amplitude resonance condition is not satisfied, the output characteristics will deteriorate. Figures 4.5(a) and 4.5(b) show the output intensities around resonance for three values of k_1 for A- and B-resonance, respectively. It can be seen that for A-resonance, at an under coupling state (i.e. $k_2 < k_{2r}^{A}$), the curve becomes broader, i.e., the full frequency width at half maximum (FWHM) of the resonant peak increases, while at an overcoupling state (i.e. $k_2 > k_{2r}^{A}$), the curve dips more sharply. However, for B-resonance, the opposite effects happen. Similar properties for the circulating intensities are shown in Figs. 4.5(c) and 4.5(d). It is clear from Figs. 4.5(a)-(d) that under optimum conditions, the circulating intensity reaches a maximum and the output a minimum.

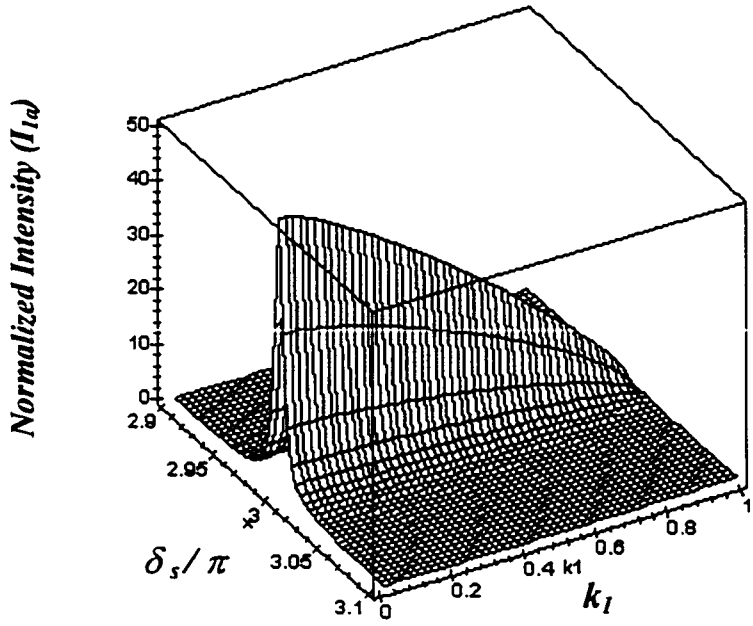

(a)

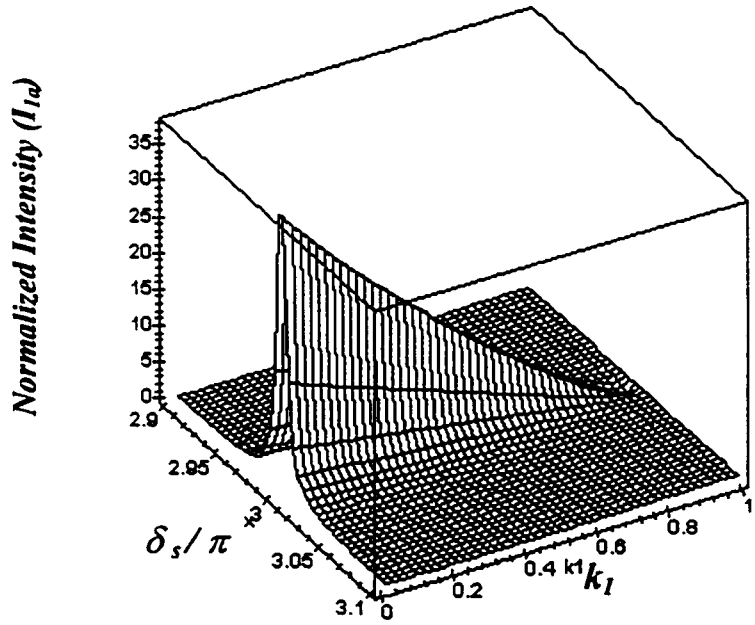

(b)

Figure 4.4 Circulating intensity I_{1a} as a function of k_1 and the optical phase δ_s with optimum k_2. Other parameters are $\gamma_1 = \gamma_1 = 0$, $p_s = p_p = 0.995$.

(a) A-resonance (b) B-resonance

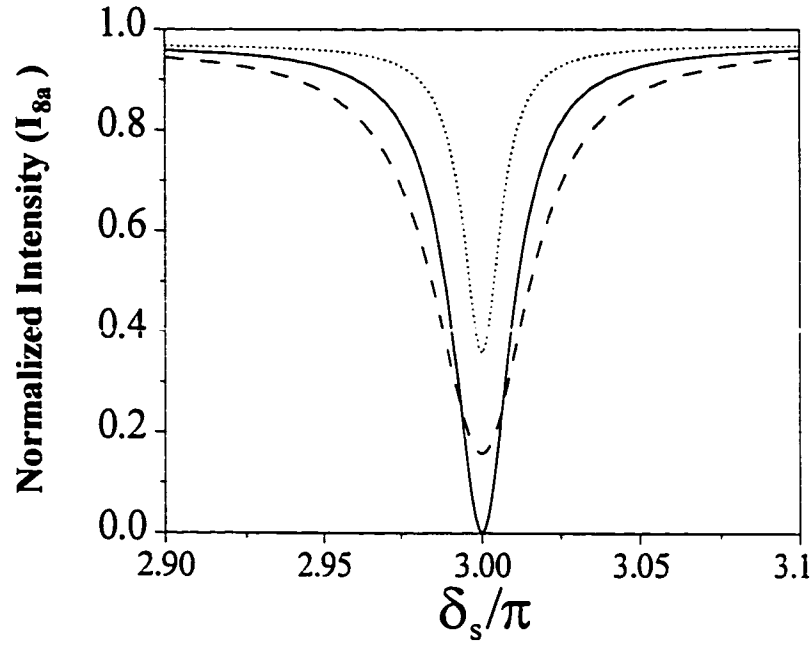

(a)

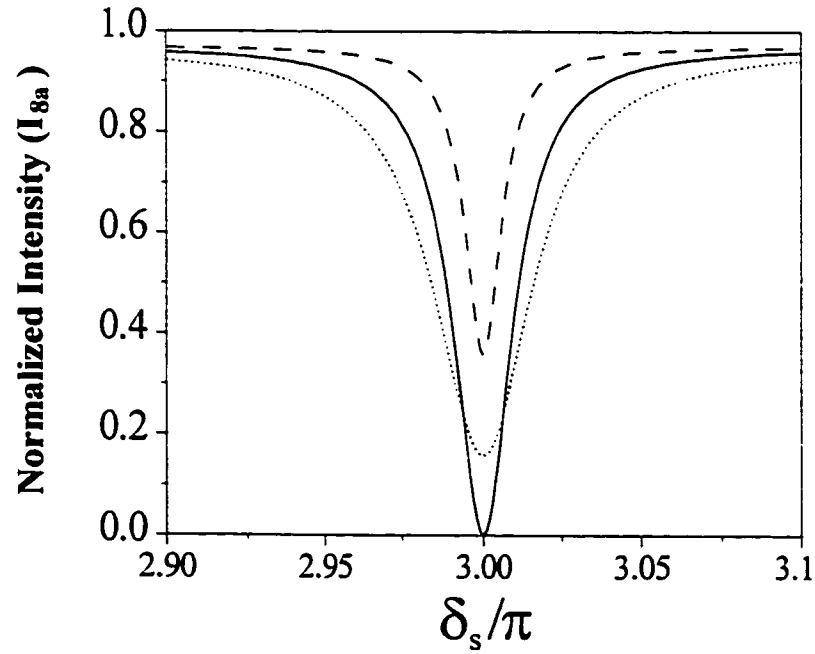

(b)

Figure 4.5 Normalized intensities as functions of the optical phase δ_s for various values of k_2. (a) & (c) A-resonance,$k_1=0.6$, Solid: $k_2 = 0.4$ (k_{2r}^A); Dashed: $k_2=0.3$; Dotted: $k_2=0.5$. (b) & (d) B-resonance, $k_1=0.4$, Solid: $k_2 = 0.6$ (k_{2r}^B); Dashed: $k_2=0.5$; Dotted: $k_2=0.7$. Other parameters are $\gamma_1=\gamma_2=1\%$, and $p_s=p_p=0.99$.

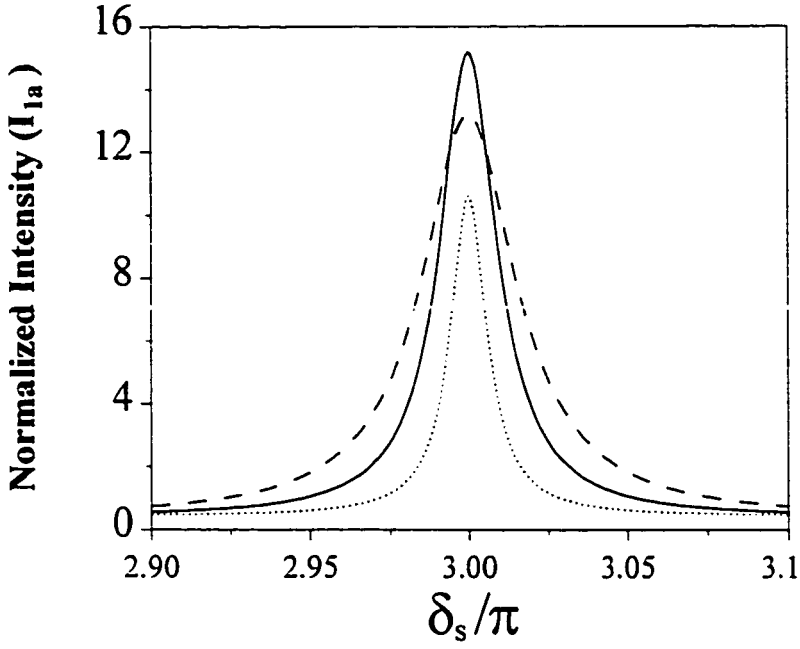
Normalized Intensity (I_{1a})
16
12
8
4
0
2.90
2.95
3.00
3.05
3.1
δ_s/π

(c)

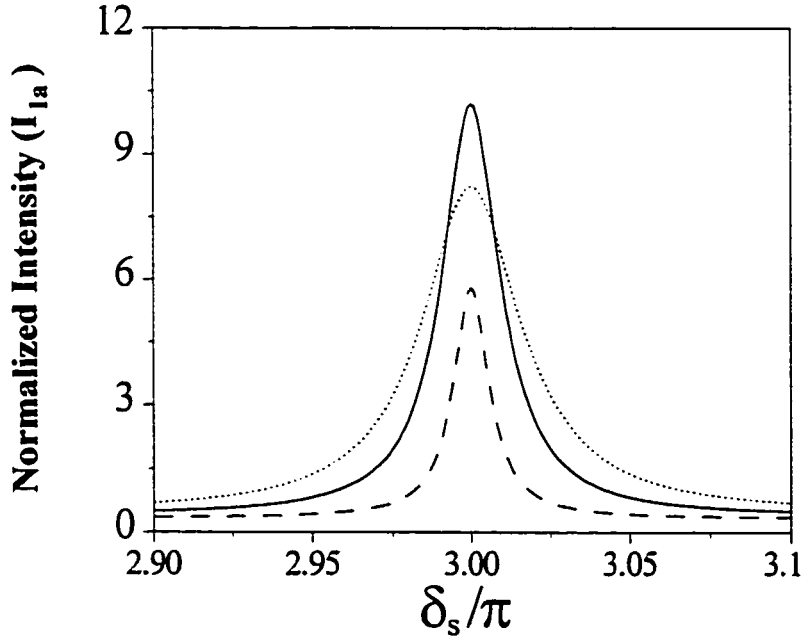
Normalized Intensity (I_{1a})
12
9
6
3
0
2.90
2.95
3.00
3.05
3.1
δ_s/π

(d)

Figure 4.5

On the other hand, when the losses in the resonator change, the characteristics will be seriously affected. This can be verified from Figs. 4.6(a)-(d). The circulating intensities as functions of the optical phase for various values of transmission factors in A- and B-resonance are plotted in Figs. 4.6(a) and 4.6(b), and the output intensity characteristics in both cases in 4.6(c) and 4.6(d), respectively. For both A- and B-resonance, the transmission factor reduces the height of the circulating intensities, and the sharpness of the intensity curves, and consequently reduces the finesse of the resonator also. However, under the same conditions, the characteristics of B-resonance are degraded more by the transmission factor than those of A-resonance. The coupling loss has the similar effect on the characteristics of A- and B- resonance, since on a round trip in both rings, there are twice the amount of splice losses and twice the amount of coupling losses.

4.2.3.2 Mode Suppression

Besides the optimum amplitude resonance condition, the phase resonance condition is the other important resonance condition. When the phase resonance conditions in Eqs. (4.6)-(4.7) are satisfied simultaneously, there is a high circulating intensity and the *FSR* of the CRR can be enhanced, when compared with the *FSR* of each of the two rings, which is defined as the separation between two neighbouring resonant peaks, expressed as

$$FSR_i = \frac{c}{n_e L_i} \qquad i = s, p \tag{4.11}$$

where c is the velocity of light in vacuum; n_e is the effective index of the fiber, and L_i is the ring length. According to Eqs.(4.6)-(4.7), when both rings are resonating simultaneously, the ratio of the lengths (*RoL*) of ring p and ring s is:

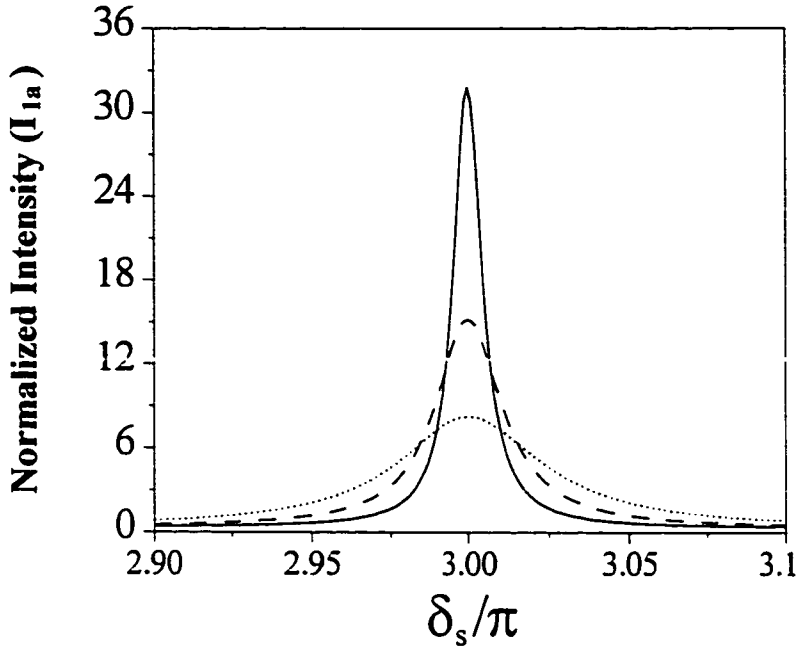

(a)

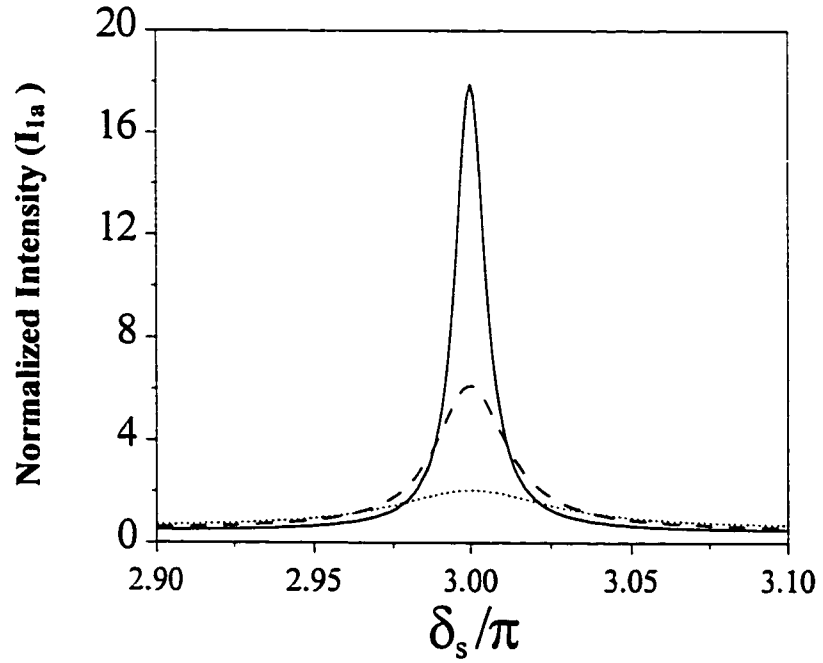

(b)

Figure 4.6 Normalized intensities as functions of the optical phase δ_s for various values of transmission factors. Solid: $p_s=p_p=1$; Dashed: $p_s=p_p=0.986$; Dotted: $p_s=p_p=0.958$. Other parameters are $k_1=0.5$ and $\gamma_1=\gamma_2=1\%$.

(a) & (c) A-resonance; (b) & (d) B-resonance .

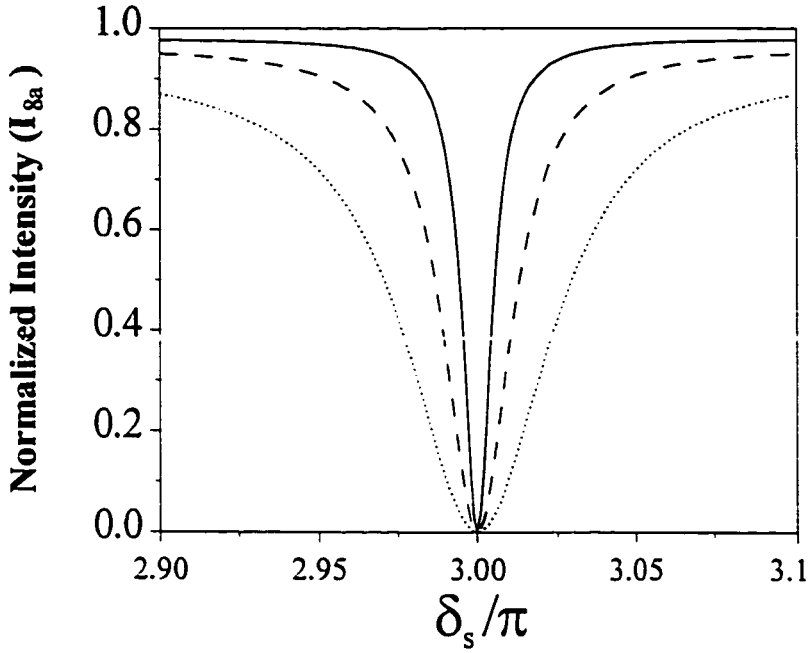
Normalized Intensity (I_{8a})
1.0
0.8
0.6
0.4
0.2
0.0
2.90
2.95
3.00
3.05
3.1
δ_s/π

(c)

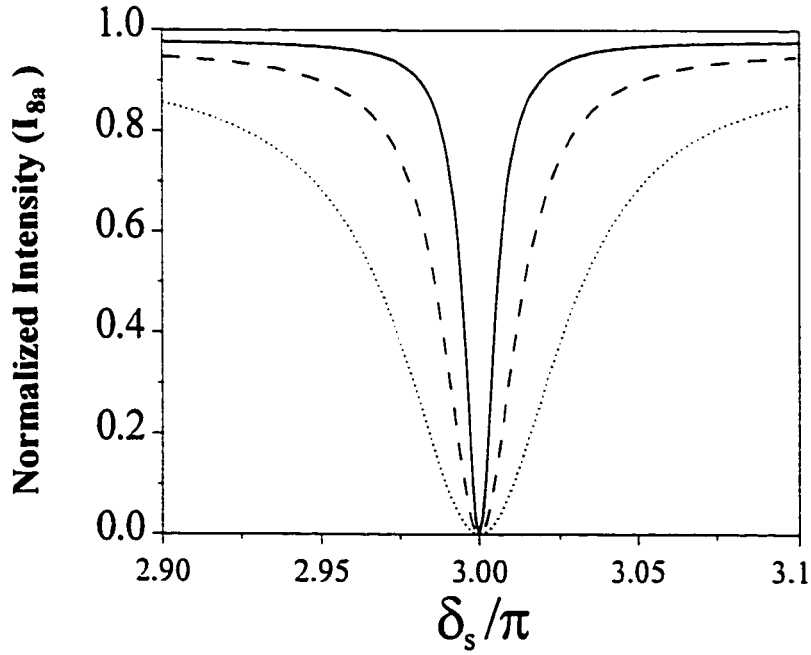
Normalized Intensity (I_{8a})
1.0
0.8
0.6
0.4
0.2
0.0
2.90
2.95
3.00
3.05
3.1
δ_s/π

(d)

Figure 4.6

$$RoL = L_p : L_s = (2m) : (2n+1) \tag{4.12}$$

Note that $2m$ is an even number and $2n$+1 is odd. Then, the ($2m$)th main peak of ring p will coincide with the ($2n+1$)th main peak of ring s. Consequently, the resultant *FSR* of the DCDR resonator is $2m$ times that of ring p and $2n$+1 times that of ring s, written as

$$FSR = (2m) \cdot FSR_p = (2n+1) \cdot FSR_s \tag{4.13}$$

This is the vernier effect that increases the *FSR* of the DCDR.

When the compound ring resonator is used as a filter, the lengths of the two rings are normally chosen to be slightly different, such as $RoL = N : (N-1)$, in order to make good use of the vernier effect; N is an even integer, and is defined as the resonant number. The resultant *FSR* is increased by many times for each of the two rings. The bigger is the value of N, the bigger is the *FSR*, and the closer is *RoL* to 1. Such a situation is referred as the case $RoL \to 1$. On the other hand, when the compound ring resonator is used as a laser resonator, the lengths of the two rings are normally chosen to be widely different, such as $RoL = N : 1$. This is because the length of the primary ring usually has to be tens of meters long, due to the inevitable inclusion of the active fiber and a number of cavity components. The *FSR* of the compound ring resonator is determined by the *FSR* of the small ring s, which could be made as small as possible to increase the *FSR*. Such a situation is referred as the case $RoL \gg 1$.

Figure 4.7 shows the circulating intensity as a function of the phase change of the rings. *RoL* is 12:11, the coupler coefficient k_1 is 0.5, and k_2 is fixed at k_{2r}^A for A-resonance. As can be seen in the figure, the resultant *FSR* of the CRR resonator is enhanced by 11 times those of the rings.

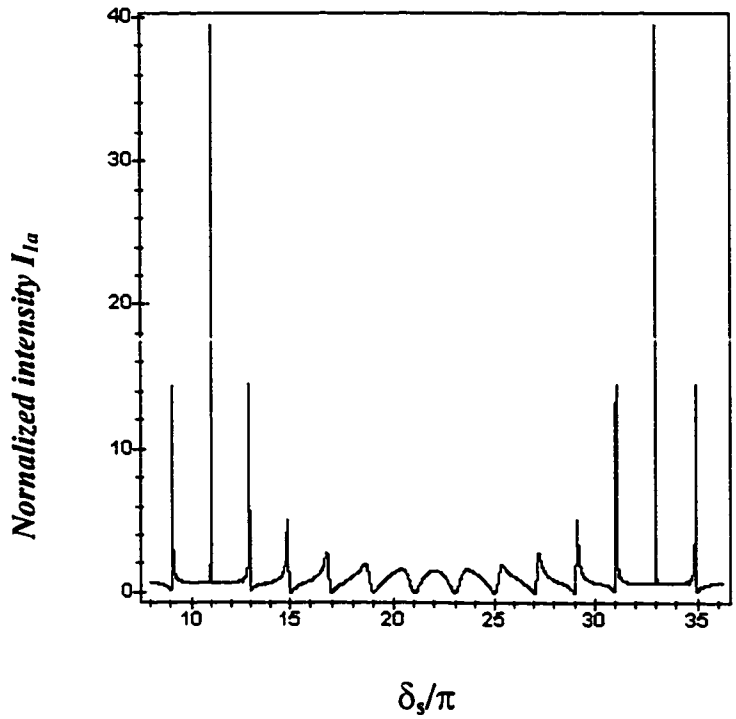

Figure 4.7 Mode suppression by the vernier effect. k_1=0.7, k_2 = k_{2r}^A, γ_1 =γ_2=0.5%, p_s=p_p=1, and L_p:L_s=12:11.

4.2.3.3 Reduction Factor

One of the important performance parameters of a vernier filter is the reduction factor. It is defined as the ratio of the height of the largest side peak to that of the main peak in the circulating intensity. A good compound ring resonator should have a small reduction factor, which is dependent on the coupler coefficient and the resonant number.

A) Influence of coupler coefficient k_1

Figures 4.8(a) and 4.8(b) display the reduction factor as a function of coupler coefficient k_1 for various values of coupler losses under A- and B-resonance, respectively. We have chosen *RoL* to be 4:3 (i.e., case $RoL \to 1$, and $N = 4$), and the

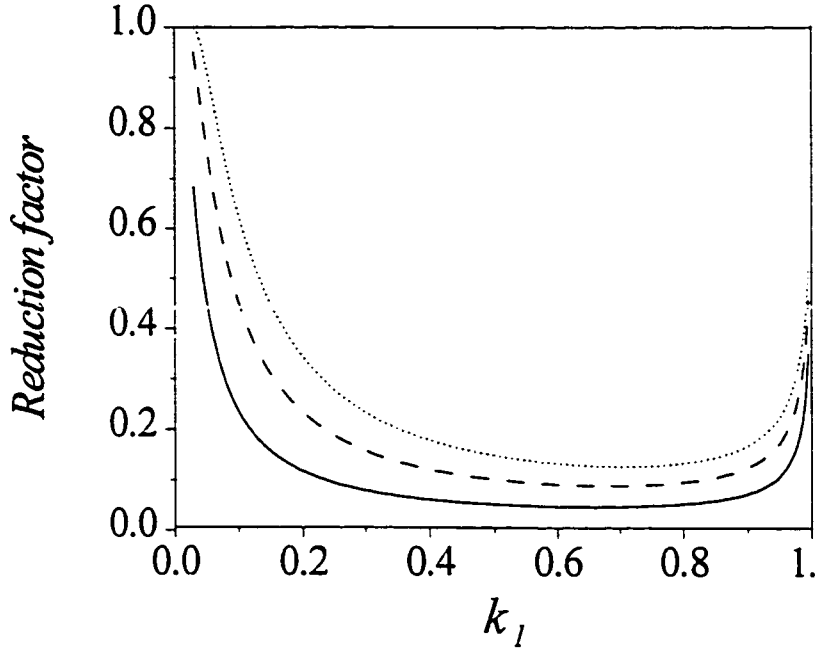

(a)

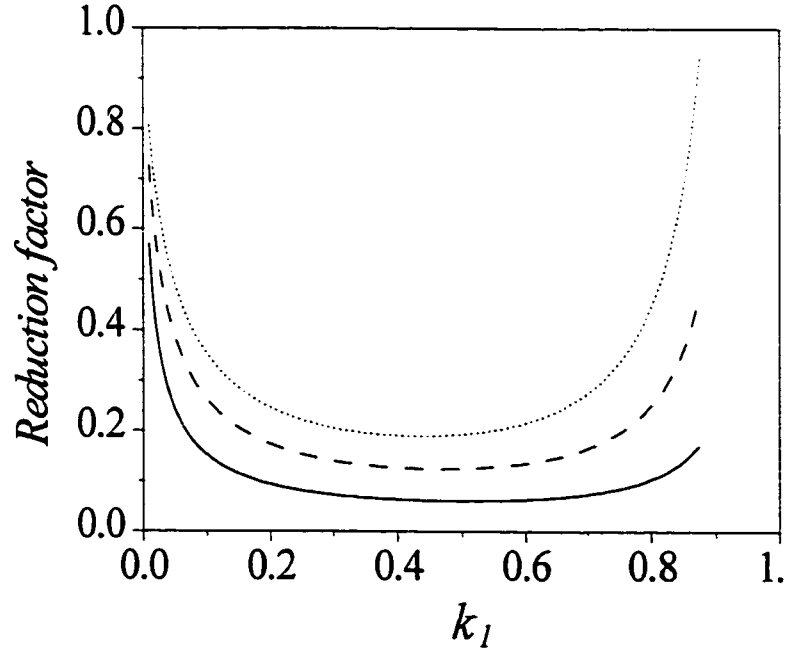

(b)

Figure 4.8 The reduction factor as a function of coupler coefficient for various values of the coupler losses with $p_s=p_p=0.995$, and $L_p:L_s$=4:3. Solid: $\gamma_1=\gamma_2=0$; Dashed: $\gamma_1=\gamma_2=0.5\%$; Dotted: $\gamma_1=\gamma_2=1\%$ (a) A-resonance (b) B-resonance

transmission factors of the two couplers are 0.995 for A- and B- resonance. As the coupler loss decreases, the reduction factor decreases. For both types of resonance, the reduction factor has a small minimum range, and with decreasing coupler loss, the minimum range becomes wider and flatter.

By comparing the A-resonance with the B-resonance, the following phenomena can be seen:

a. Under the same conditions (i.e., coupler loss, transmission factor and resonant number), the minimum reduction factor under A-resonance is smaller than under B-resonance.

b. The usable range of k_1 is wider under A-resonance than under B-resonance. The k_1 for the lowest reduction factor is around 0.7 and 0.4 for A- and B-resonance, respectively.

c. Under A-resonance, when $k_1 < 0.04$, the reduction factor will be more than 1, i.e., no vernier effects. Under B-resonance, when $k_1 > 0.87$, there is no vernier operation.

Similar curves for the case $RoL \gg 1$ could be obtained for both types of resonance.

B) Influence of the resonant number

As we have seen, when the resonant number N increases, the vernier operation becomes more effective; however, it degrades the reduction factor. Figures 4.9(a)-(b) and 4.10(a)-(b) show the reduction factor as a function of the resonant number in the case $RoL \to 1$ and $RoL \gg 1$, respectively. The curves (a) and (b) respectively correspond to A- resonance and B-resonance. Inspection of Figs.4.9-4.10 shows the following characteristics:

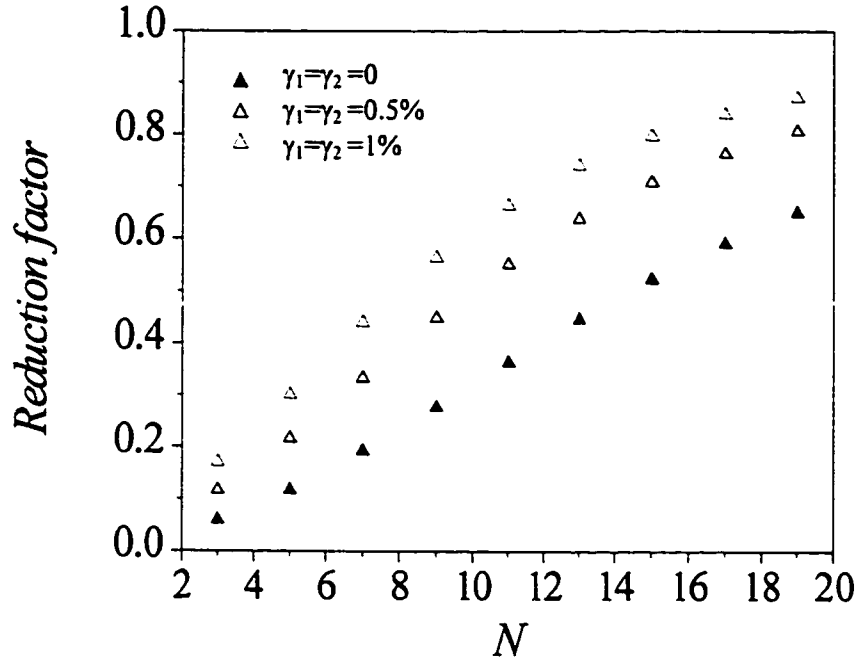

(a)

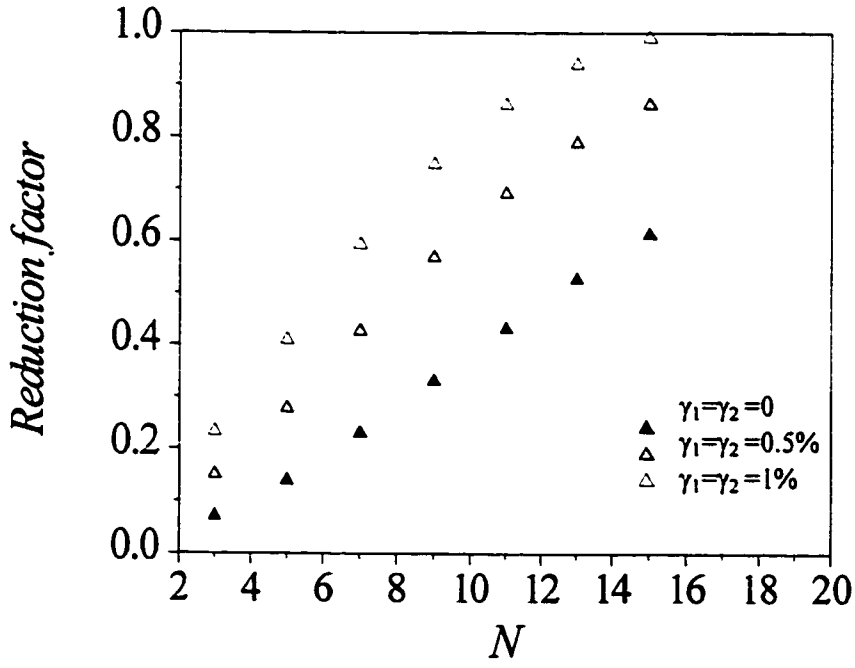

(b)

Figure 4.9 The reduction factor versus the resonant number N for various values of coupling losses with $p_s=p_p=0.995$ in case $RoL\rightarrow 1$. (a) A-resonance (b)B-resonance

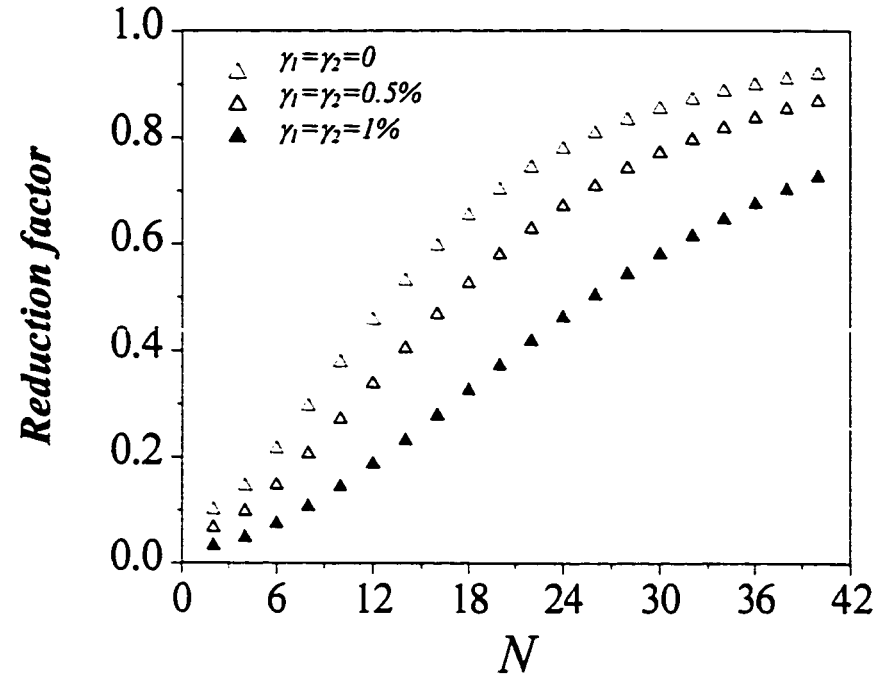

(a)

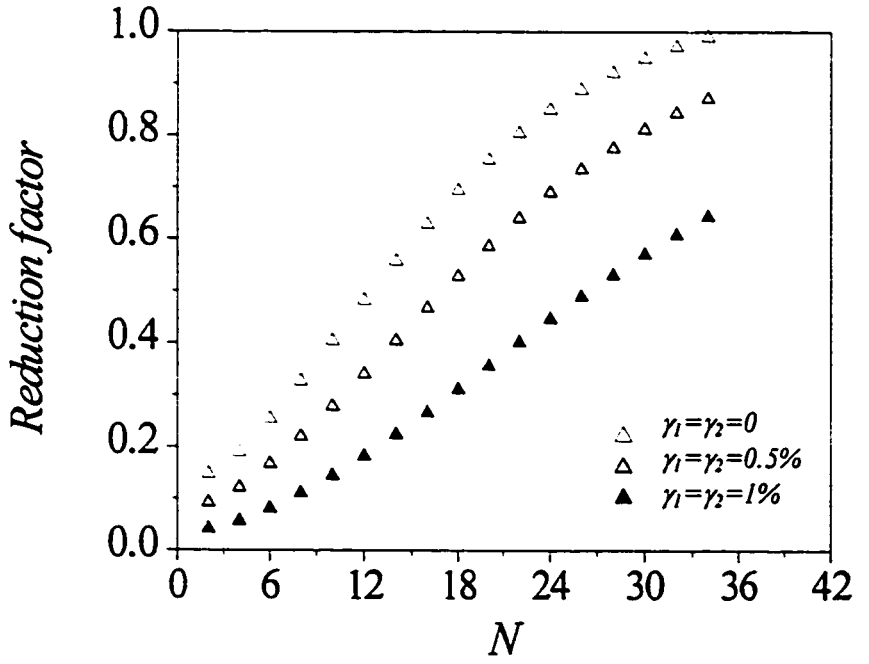

(b)

Figure 4.10 The reduction factor versus the resonant number N for various values of coupling losses with $p_s=p_p=0.995$ in case $RoL \gg 1$. (a) A-resonance (b) B-resonance

a. As the resonant number and coupler loss increase, the reduction factor increases in both types of resonance; however, it degrades faster in the B-resonance than in the A-resonance, for both cases of *Ro*L.

b. Under the same conditions (i.e., losses and resonant number), the A-resonance has a reduction factor smaller than that of the B-resonance. Thus the allowable maximum resonant number is smaller in the B-resonance than in the A-resonance for both cases of *RoL*.

c. Comparison between two cases $RoL \gg 1$ and $RoL \to 1$ tells us that for the same resonant number, the reduction factor is much smaller in case $RoL \gg 1$ than in $RoL \to 1$. Thus the allowable maximum resonant number is much greater in case $RoL \gg 1$ than in $RoL \to 1$.

4.3 Compound Ring Resonator with an External Reflector

In the last section, we have discussed the basic two-coupler compound ring resonator. As mentioned in chapter 3, when an external reflector is added to a single ring resonator, the resonator becomes a non-reciprocal resonator, which has a loss difference between the cw and ccw directions, if used as a fiber laser. Similarly, such principle may be applied to the CRR.

4.3.1 Principle of Operation

Figure 4.11 shows the configuration of the compound ring resonator with an external reflector (CRRER). It consists of a double-coupler double-ring resonator and a reflector. The reflector R is joined to one of the two free ends of the two couplers. The double couplers have intensity coupling coefficient k_1 and k_2, and the double rings have

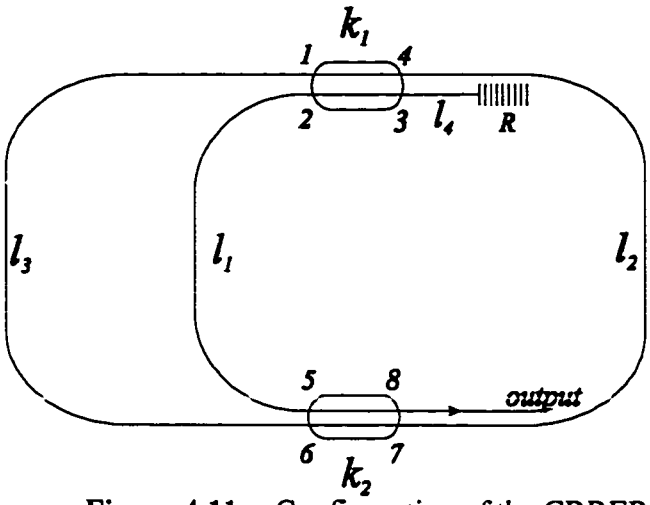

Figure 4.11 Configuration of the CRRER

cavity length $l_p = l_2 + l_3$ and $l_S = l_1 + l_2$. Since this resonator is used to build fiber lasers, we modify the configuration as in Fig.4.12, by inserting a piece of gain medium EDF, in order to see clearly how the non-reciprocal loss is formed.

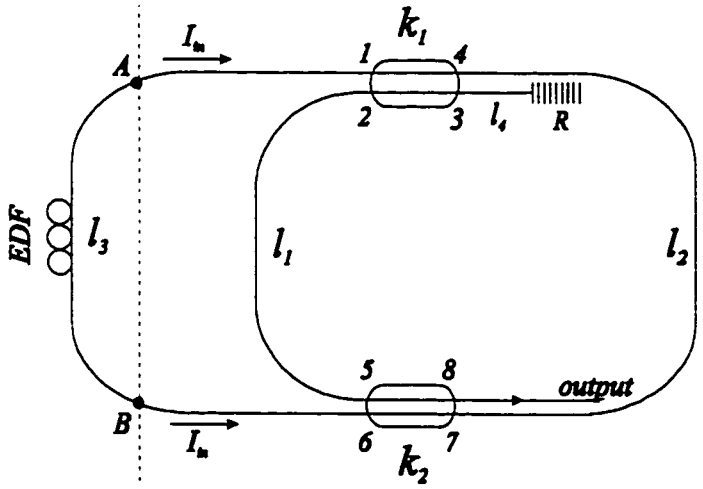

Figure 4.12 Configuration of the CRRER for lasers
EDF: erbium-doped fiber; R: reflector

Just as does the reflector in the FRRER described in chapter 3, the reflector plays the same role in the CRRER by introducing non-reciprocal loss for the cw and ccw directions. Below lasing threshold, let us consider that the same amounts of ASE power I_{in} start from point A and B, and travel along the ring resonator at the right side of the

dashed line. When the light propagates from point B along the ccw direction, it will return part of the light in the same direction at point A, and another part of the light will come out as output, where the reflector has no effect. However, when the light propagates from point A along the cw direction, besides the above two parts of the light, part of the light will feedback to the ccw direction to point A due to the reflector. Therefore, the non-reciprocal loss between the two directions is introduced, which may result in unidirectional oscillation favoring the ccw direction without the use of optical isolator. In the next section, we will calculate the loss difference in term of the coupling coefficients.

4.3.2 Directionality Analysis

The loss difference has been defined in Eq.(3.1) in chapter 3, as

$$LD = 10\log(\frac{RI_A}{RI_B}) \tag{4.14}$$

where RI_A and RI_B are the returned intensities at points A and B, considering the lights are launched from B and A along the ccw and cw directions, respectively. According to Fig.4.12, they are given by:

$$\begin{aligned} RI_A &= I_{1a}^{cw} + I_{1a}^{ccw} \\ RI_B &= I_{6a}^{cw} \end{aligned} \tag{4.15}$$

where the superscripts *cw* and *ccw* in Eq.(4.15) denote the direction, from which the input light is launched, and subscript *a* denotes the light away from the coupler.

The intensities in Eq.(4.15) can be obtained by analyzing the resonator at the right side of the dashed line in Fig. 4.12. Considering the light is input from the ccw direction, the double-coupler ring resonator with an external reflector (DCRRER) will be analyzed, which is given in Appendix D2. From Eqs.(D.20) and (D.22), then we have I_{1a}^{cw} and I_{6a}^{cw} at phase resonance, expressed as:

$$I_{1a}^{cw} = \frac{R[b_1 - b_2(1-\gamma_1)p_s]^4}{(1-b_1 b_2 p_s)^4} \tag{4.16}$$

$$I_{6a}^{cw} = \frac{a_1^2 a_2^2 p_s^2}{(1-b_1 b_2 p_s)^2} \tag{4.17}$$

On the other hand, for the input light from the ccw direction, double-coupler ring resonator (DCRR) without the reflector will be analyzed. The DCRR is the special case of the DCRRER when the reflectivity is set to be zero. Then we have the following relations:

$$\begin{aligned} I_{1a}^{ccw} &= I_{6a}^{cw}(k_1 \Leftrightarrow k_2) \\ I_{8a}^{ccw} &= I_{3a}^{cw}(k_1 \Leftrightarrow k_2) \end{aligned} \tag{4.18}$$

where the symbol $\Leftrightarrow$ denotes the switch from k_1 to k_2 and vice versa.

From Eqs. (4.16)-(4.18), therefore, the loss difference can be written as:

$$LD = 10\log\left(\frac{R[b_1 - b_2(1-\gamma_1)p_s]^4}{a_1^2 a_2^2 p_s^2 (1-b_1 b_2 p_s)^2} + 1\right) \tag{4.19}$$

Figure 4.13 shows the loss difference as a function of k_2 for different values of k_1. It can be seen that a big *LD* can be obtained if k_1 and k_2 are chosen to be very different, i.e., either big k_1 and small k_2, or small k_1 and big k_2, which are referred to as $k_1^b - k_2^s$ and $k_1^s - k_2^b$ in the following, respectively. The superscripts b and s denote big and small. These could be better explained with the help of the optimum amplitude in Eq.(D.25), which shows that the k_1 and k_2 are very close. Equations (D.20)-(D.25) tell us that at optimum condition, the feedback intensity I_{1a}^{ccw} is going to be zero, and I_{6a}^{cw} becomes maximum, which leads to minimum *LD* of zero. This can be seen from the intersecting point on *x*-axis in Fig. 4.13. When k_1 and k_2 are very different, I_{1a}^{ccw} and I_{6a}^{cw} will become maximum and minimum, which will lead to large values of *LD*.

4.3.3 Insertion Loss

In the last section, we have discussed the *LD* of the CRRER. When the CRRER is used in lasers as shown in Fig.4.12, the DCRRER, as well as DCRR may be considered as an effective coupler. For DCRRER, consider light leaving point A in the cw direction. Part of the light returns to point B (I_{6a}); this is defined as the effective reflection R_{eff}. Another part of the light leaves port 8 as output I_{8a}; this is defined as the effective transmission T_{eff}. The insertion loss is defined as $1-T_{eff}-R_{eff}$. In this section, we should investigate the insertion losses of the DCRRER and DCRR, as well as the effective transmissions and reflections.

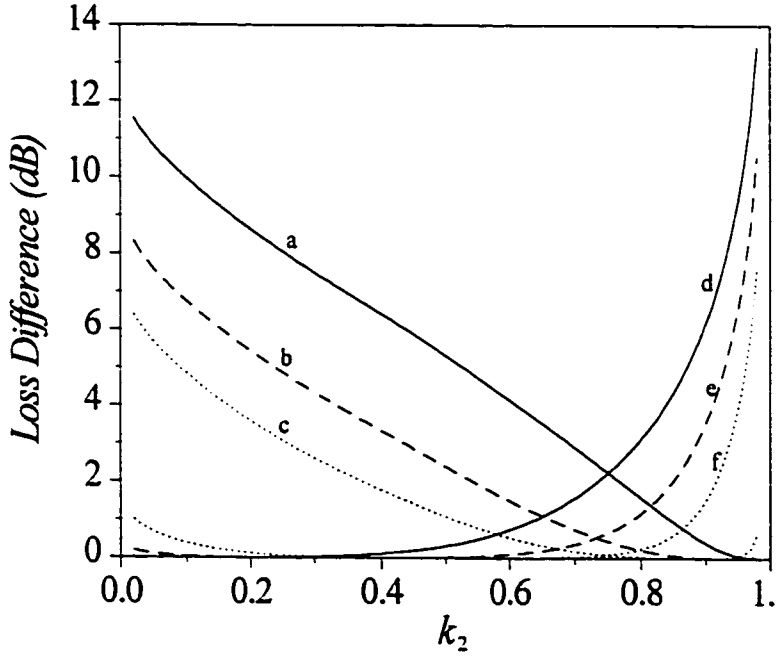

Figure 4.13 Loss difference as a function of k_2 for various values of k_1.
a: $k_1 = 0.95$; b : $k_1 = 0.9$; c: $k_1 = 0.7$; d: $k_1 = 0.5$; e: $k_1 = 0.3$; f: $k_1 = 0.1$.
Other parameters are $p_s = 0.99$, $\gamma_1 = \gamma_2 = 0.01$, and $R = 0.99$.

Figure 4.14(a) and (b) illustrate the output intensities at different ports against k_2 for two fixed values of k_1. Referring to Fig.4.12, I_{1a}, I_{6a}, and I_{8a} are the output intensities of DCRRER, which correspond to the effective feedback, reflection, and transmission,

respectively. For DCRR, consider light leaving point B in the ccw direction. Part of the light returns to point A (I_{1a}, equivalent to I_{3a} in DCRRER with switching k_1 and k_2), and the other part leaves as output (I_{8a}, equivalent to I_{6a} in DCRRER). So I_{3a} and I_{6a} in Fig. 4.12, correspond to the effective transmission and reflection of DCRR. In addition, the dark area in Fig.4.14 shows the range of *LD*, which is more than 3 dB. When k_1 is equal to 0.1, *LD* is more than 3 dB if k_2 is chosen to be greater than 0.8; when k_1 is equal to 0.9, *LD* is more than 3 dB if k_2 is chosen to be less than 0.42.

Figure 4.15 (a) and (b) display the insertion losses of the DCRRER and the DCRR against k_2 for different values of k_1. Inspection of Fig.4.15 shows the following characteristics:

1. The insertion losses of the DCRRER and DCRR have similar behaviours. When k_1 increases, the insertion losses increase. For the same parameters, the insertion loss of the DCRRER is slightly larger than that of the DCRR.
2. For both cases, with increasing k_2, the insertion losses increase. For small values of k_2, the insertion losses increase slowly, while for large values of k_2, the insertion losses increase rapidly.

As discussed earlier, the two groups of $k_1 - k_2$ are preferred for a big *LD*, which are $k_1^b - k_2^s$ and $k_1^s - k_2^b$. From Fig. 4.15, one can see that the set of $k_1^b - k_2^s$ has a low insertion loss, compared with the set of $k_1^s - k_2^b$. In the above plots, the transmission factor p_s has been fixed at 0.99. We shall investigate now how the transmission factor affects the insertion loss for the two sets of $k_1 - k_2$, i.e., $k_1^b - k_2^s$ and $k_1^s - k_2^b$. Figures 4.16 and Fig. 4.17 show the insertion losses as functions of k_2 with transmission factor as a parameter, and k_1 is fixed at 0.1 in Fig.4.16 and 0.9 in Fig.4.17, corresponding to the sets of $k_1^s - k_2^b$ and $k_1^b - k_2^s$, respectively. It is clear from Figs. 4.16 and 4.17 that, the lower

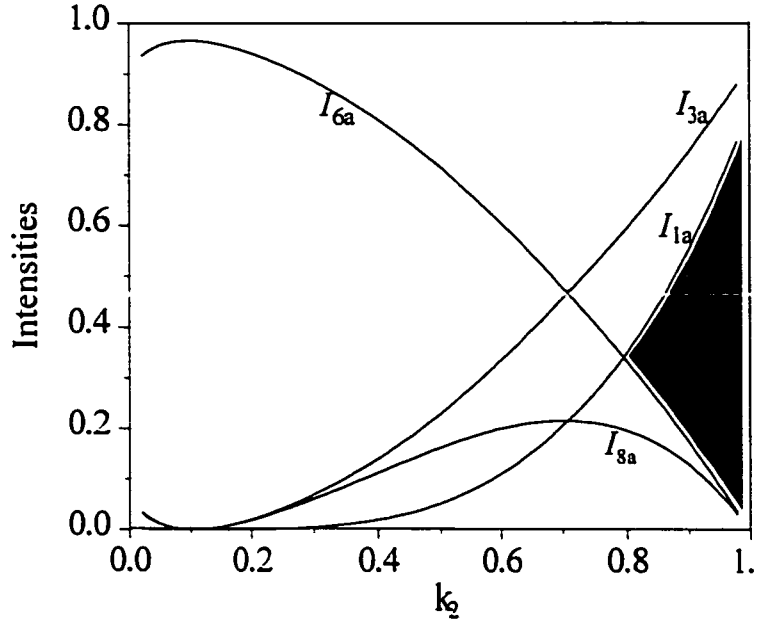

(a)

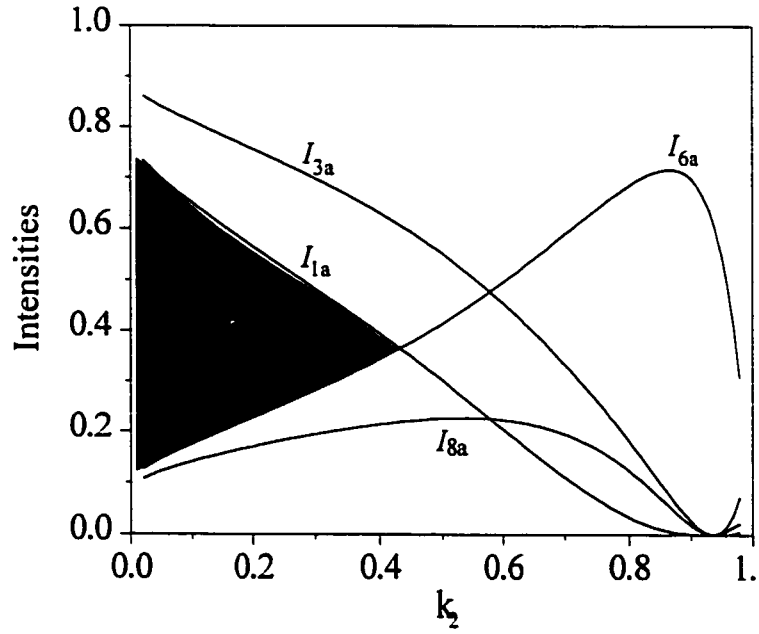

(b)

Figure 4.14 Output intensities against k_2 for a fixed values of k_1. (a) $k_1 = 0.1$ (b) $k_1 = 0.9$. Other parameters are Other parameters are $p_s = 0.99$, $\gamma_1 = \gamma_2 = 0.01$, and $R = 0.99$.

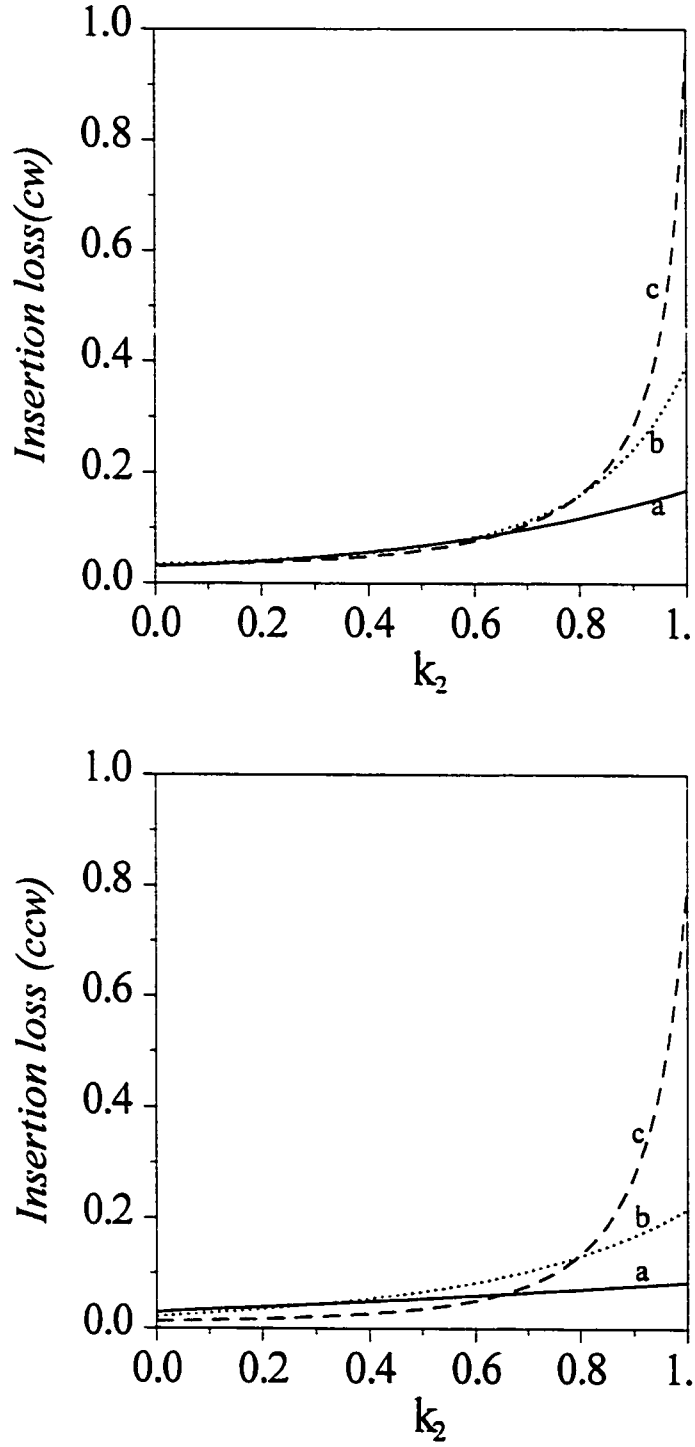

Figure 4.15 Insertion losses of (a) DCRRER and (b) DCRR against k_2 for different coupling coefficient of k_1. a: $k_1 = 0.1$; b: $k_1 = 0.5$; c: $k_1 = 0.9$. Other parameters are $p_s = 0.99$, $\gamma_1 = \gamma_2 = 0.01$, and $R = 0.99$.

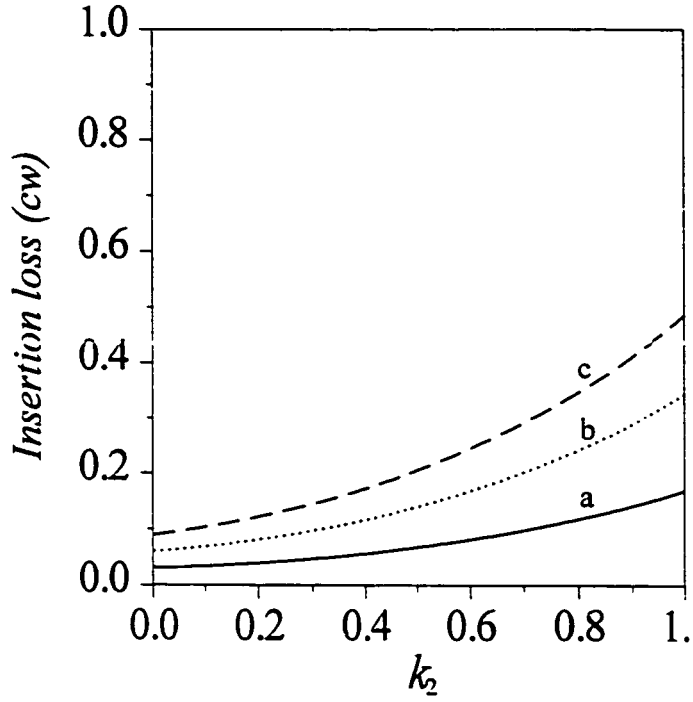

(a)

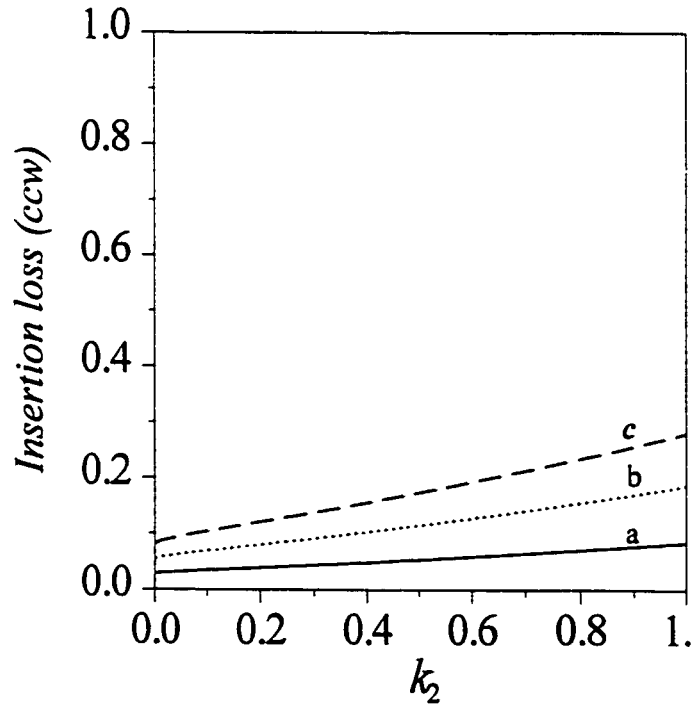

(b)

Figure 4.16 Insertion losses of (a) DCRRER and (b) DCRR against k_2 for different transmission factors with $k_1 = 0.1$. a: $p_s = 0.99$; b: $p_s = 0.96$; c: $p_s = 0.93$. Other parameters are Other parameters are $\gamma_1 = \gamma_2 = 0.01$, and $R = 0.99$.

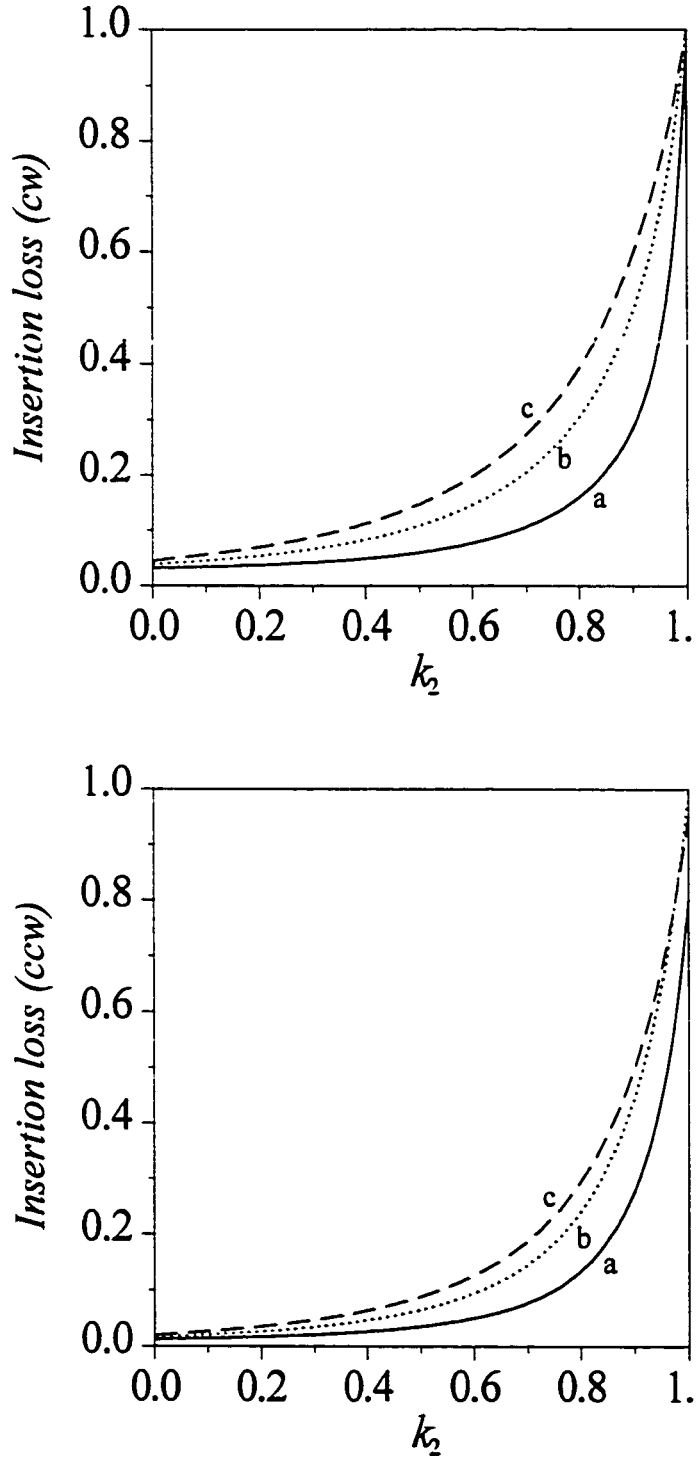

Figure 4.17 Insertion losses of (a) DCRRER and (b) DCRR against k_2 for different transmission factors with $k_1 = 0.9$. a: $p_s = 0.99$; b: $p_s = 0.96$; c: $p_s = 0.93$. Other parameters are $\gamma_1 = \gamma_2 = 0.01$, and $R = 0.99$.

the transmission factor, the bigger the insertion loss for both groups, and the set of $k_1^s - k_2^b$ has much bigger insertion loss than the set of $k_1^b - k_2^s$. Therefore, it is concluded that a high *LD* with a low insertion loss could be obtained by selecting a big k_1 and a small k_2.

4.3.4 Resonator Analysis

Since the CRRER is a non-reciprocal resonator, the situation here is similar to that described in chapter 3 for the FRRER. Referring to Fig. 4.11, two resonators, in which lights are launched into port 3 (ignore the reflector), and into port 8 should be considered. The former case corresponds to the CRR, which has been examined in detail in section 4.2, and the latter could be studied by using an unfolded equivalent model. As mentioned in chapter 3, considering the CRRER for lasers, both of the cases describe the state before the lasing threshold. Because of the loss difference in the ccw and cw directions, eventually, the lasers will oscillate in the ccw direction, for which the latter case could be applied. In this section, we will discuss the characteristics of the CRRER.

Figure 4.18 shows the unfolded equivalent model of the CRRER in Fig.4.11. The effect of the reflector could be replaced by a mirror resonator of the CRRER, where light at port 3 on the left side will be re-injected into port 3 at the right side as an input of the mirror resonator. Therefore, the output intensity and the circulating intensity of the CRRER in Fig.4.11 could be obtained, based on the relations of the intensities in the CRR as follows.

$$I_{8a}^{\cdot} = R \cdot I_{8a}(k_1 \Leftrightarrow k_2) \cdot I_{8a} \tag{4.20}$$

$$I_{1a}^{\cdot} = R \cdot I_{8a}(k_1 \Leftrightarrow k_2) \cdot I_{1a} \tag{4.21}$$

where R is the reflectivity of the external reflector.

Obviously, from Eq.(4.21) the CRRER has the same optimum conditions as the CRR, which are given earlier in section 4.2. We note that Eqs.(4.20)-(4.21) are analogous to Eqs.(3.15)-(3.16), then it is expected that the output intensity and the circulating intensity have the same behaviours as that for FRRER in section 3.3.2. Since we are

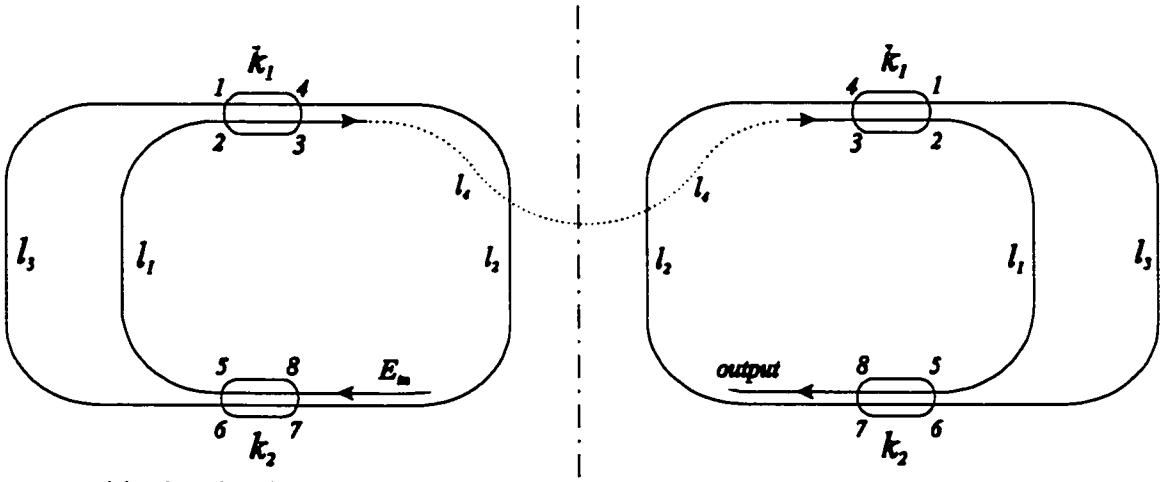

interested in the circulating intensity, in the following, we will examine the behaviours of the circulating intensity and the mode suppression.

Figure 4.18 Unfolded equivalent model of the configuration in Fig.4.11. The right side of the dashed line is a mirror image of the left side.

Figure 4.19 shows the circulating intensity as a function of the optical phase for various values of the coupling coefficient k_2. From Fig.4.19, it can be seen that when k_2 changes, the shape of the curve changes from quasi-channel-blocking type to channel-passing type. At the optimum values of k_2, the shapes of the curves are quasi-channel-blocking type with a dip at zero intensity, and with decreasing k_2, the dip depth decreases. When $k_2 = 0.635$, the curve becomes channel-passing type with a flat top. With further decrease in k_2, corresponding to the case of $k_1^b - k_2^s$, it becomes the regular channel-

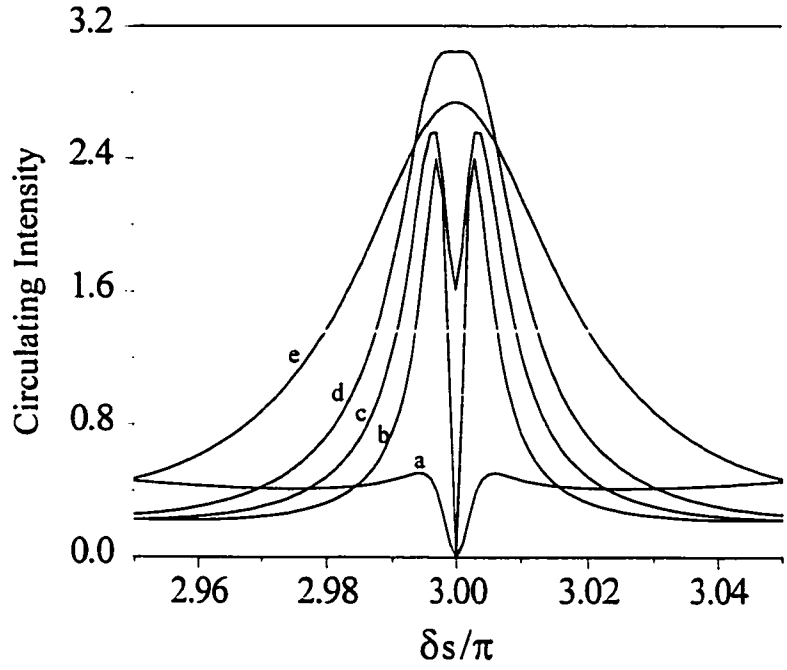

Figure 4.19 Circulating intensities as a function of optical phase δ_s / π. a: $k_2 = k_{opt}^B = 0.968$; b: $k_2 = k_{opt}^A = 0.80$; c: $k_2 = 0.73$; d: $k_2 = 0.635$; e: $k_2 = 0.3$. Other parameters are $k_1 = 0.9$, $\gamma_1 = \gamma_2 = 0.01$, and $R = 0.99$.

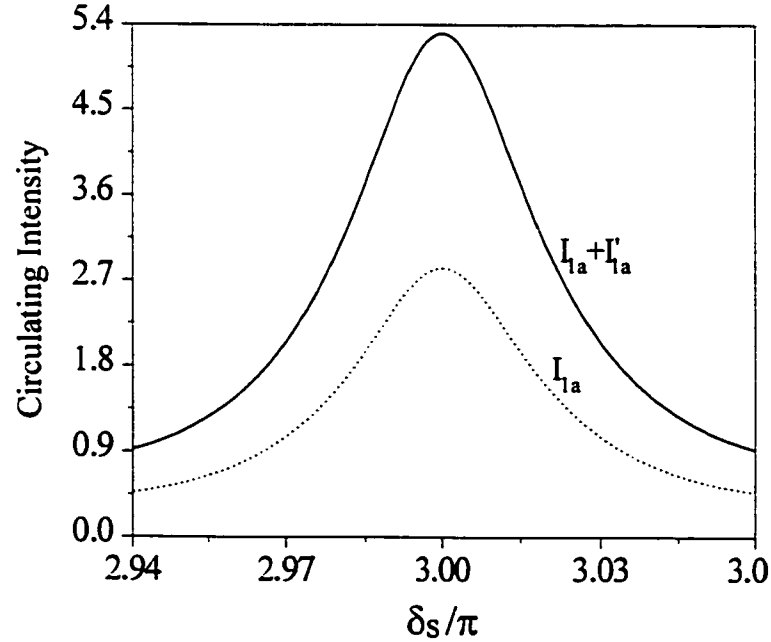

Figure 4.20 Circulating intensities as a function of optical phase δ_s / π for $l_p / l_s = 10$. Other parameters are $k_1 = 0.9$, $k_2 = 0.2$, $\gamma_1 = \gamma_2 = 0.01$, $p_s = p_p = 0.99$ and $R = 0.99$.

passing type, which is desirable for the CRRER as a laser resonator. We recall that the total circulating intensity of the CRRER is the summation of $I_{1a}^{'}$ and I_{1a}. The curves of the circulating intensities of the CRRER and CRR are shown in Fig. 4.20, from which it is obvious that the circulating intensity of the CRRER is nearly twice that of the CRR.

As to the mode suppression, it is expected that the CRRER has the same behaviour as the CRR because of the same phase resonance conditions. We recall that in section 4.2, the mode suppression as well as the reduction factor of the CRR are investigated, based on the optimum values of the coupling coefficients. However, as mentioned above, for applications in lasers, $k_1^b - k_2^s$ is the preferred choice for the CRRER with a high *LD*, thus, we shall explore the mode suppression when the coupling coefficients are chosen to be different from the optimum values.

Figure 4.21 demonstrates the mode suppression by use of the vernier effect in the CRRER. The ratio of the two cavity lengths is 6:1, and the coupling coefficients are chosen to be $k_1^b - k_2^s$ (k_1=0.9and k_2=0.2). From Fig.4.21, it can be seen that the *FSR* of the CRRER is determined by the FSR of the small ring, in other words, it is increased by 6 times that of the primary ring. The main peaks occur when the two rings resonate simultaneously, while the side peaks occur when only the primary ring resonates. It is noted that when increasing the ratio of the cavity lengths, the reduction factor (i.e., the ratio of the side peak to the main peak) will increase, which has been discussed earlier in section 4.2.

It is well known that for implementation of the CRRER in lasers, it is unavoidable to have a long main cavity length, due to the components. Therefore, by building a small

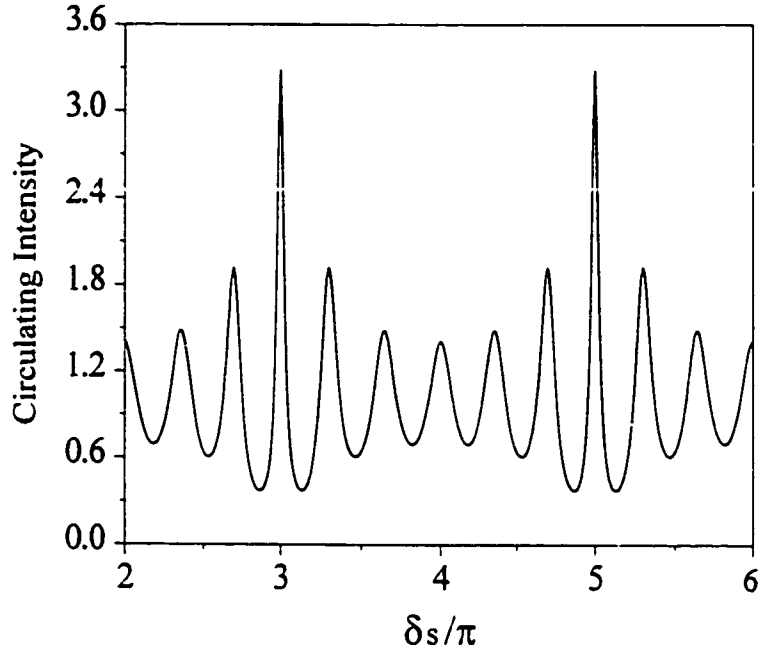

Figure 4.21 Mode suppression by vernier effect in CRRER for $l_p / l_s = 6$ Other parameters are $k_1 = 0.9$, $k_2 = 0.2$, $\gamma_1 = \gamma_2 = 0.01$, $p_s = p_p = 0.99$ and $R = 0.99$.

sub-ring resonator, it will enhance the FSR of the CRER, and consequently, improve the mode suppressions. This is a very useful property for applications in doped fiber lasers.

4.4 Summary

In this chapter, we have presented a theoretical analysis of the compound ring resonator (CRR), following by the CRR with an external reflector (CRRER).

The CRR is a double-coupler double-ring resonator. The analysis indicates that corresponding to one set of phase resonance condition, there are two sets of amplitude resonance conditions, i.e., A-resonance and B-resonance. For both types of resonance, a

small coupler coefficient k_1 is advantageous in terms of the circulating intensity, while a minimum value for the reduction factor can be obtained by suitably choosing the coupler coefficient k_1. It is found that under A-resonance, the circulating intensity is higher and the reduction factor is smaller than B-resonance. The resultant *FSR* of a DCDR resonator can be significantly enhanced by the vernier effect. The length of the two rings *RoL* may be chosen to be close to unity, $RoL \to 1$ or widely different, $RoL \gg 1$, for different applications. It appears that the case $RoL \gg 1$ has a reduction factor smaller than the case $RoL \to 1$. In both cases, a small resonant number is advantageous in terms of the reduction factor. These results may be useful when the compound resonator is used to construct narrow-bandwidth filters and single-frequency doped fiber lasers.

Based on the CRR, we designed the CRRER, which was mainly used for travelling-wave doped fiber lasers without using optical isolators, and which also has the advantages of the CRR. The computed results show that the loss difference depends greatly on the coupling coefficients, and a higher loss difference could be obtained by choosing the coupling coefficients either $k_1^b - k_2^s$ or $k_1^s - k_2^b$; however, the set of $k_1^b - k_2^s$ is the better choice because of the lower insertion loss. Considering the case of $k_1^b - k_2^s$, it is found that the circulating intensity in the CRRER is about twice of that in the CRR, and the mode suppression could be achieved by choosing the proper ratio of the cavity lengths of the two rings. Such a resonator is particularly advantageous in applications in doped fiber lasers.

4.5 Reference

1. J. Zhang and J.W.Y. Lit, "Compound fiber ring resonator: theory", *J. Opt. Soc. Am. A*, vol. 11, pp.1867-1873, 1994.
2. Y.H. Ja, "Flattening and reversing of resonant curves in an S-shaped two-coupler optical fiber-ring resonator", *Microwave Opt. Tech. Lett.*, vol. 7, pp.546-549, 1994.
3. F. Zhang and J.W.Y. Lit, "Direct-coupling single-mode fiber ring resonator", *J. Opt. Soc. Am. A*, vol. 5, pp.1347-1355, 1988.
4. P. Urquhart, "Compound optical-fiber-based resonators", *J. Opt. Soc. Am. A*, vol. 5, pp.803-812, 1988.
5. K. Oda, N. Takato, and H. Toba, "A wide-FSR waveguide double-ring resonator for optical FDM transmission systems", *J. Lightwave. Tech.*, vol. 9, pp.728-736, 1991.
6. G. Barbarossa, A.M. Matteo, and M.N. Armenise, "Theoretical analysis of triple-coupler ring-based optical guide-wave resonator", *J. Lightwave. Tech.*, vol. 13, pp.148-157, 1995.
7. Y.H. Ja, "A vernier S-shaped fiber double-loop resonator with double couplers and degenerate two-wave mixing", *J. Lightwave. Tech.*, vol. 11, pp.728-736, 1993.
8. J. Zhang and J.W.Y. Lit, "All-fiber compound ring resonator with a ring filter", *J. Lightwave. Tech.*, vol. 12, pp.1256-1262, 1994.
9. T. Peiffer, H. Schmuck, and H. Bulow, " Output power characteristics of erbium-doped fiber ring lasers", *IEEE Photon. Technol. Lett.*, vol.4, pp.847-849, 1992.
10. J. Zhang, C. Yue, G.W. Schinn, W.R.L. Clements and J.W.Y. Lit, "Stable single-mode compound-ring erbium-doped fiber laser", *J. Lightwave. Tech.*, vol.14, pp.104-109, 1996.
11. Double ring resonator with an external reflector, in preparation.

Chapter 5

Erbium-Doped Fiber Ring Laser: Experimental and Results

In the previous two chapters, we investigated the resonance characteristics of the FRR and CRR, as well as these resonators with external reflectors, i.e., FRRER and CRRER. We also analyzed the directional properties of the FRRER and the CRRER. In this chapter, we will present the single-wavelength travelling-wave erbium-doped fiber lasers (EDFLs), whose structures are based on the FRRER and CRRER. In addition to the single-wavelength EDFLs, a dual-wavelength EDFL has been developed, by modifying the EDFL with FRRER. Multiple-wavelength EDFLs are interesting because of their applications in fiber-optic WDM systems. In the following sections, we will first look at the related basic components in our EDFLs, and then give the experimental results of these lasers.

5.1 Related Fiber Laser Components

As mentioned in chapter 2, a fiber laser has a gain medium and various related devices. In our lasers, these devices include couplers, WDM, fiber Bragg grating, polarization controller and pump source. In the following sections, we shall discuss the basic principles of these components and their specifications.

5.1.1 Coupler and WDM

The single-mode directional coupler is a very important device in fiber lasers and fiber amplifiers. An ideal directional coupler is shown in Fig. 5.1. Light launched into port 1 is guided along the waveguides. In the coupling region, two waveguides are sufficiently close to produce an overlap of their transverse fields. Based on the coupled mode theory, the power transfer follows the cosine square and sine square forms:

$$\begin{aligned} P_1(L) &= P_1(0)\cos^2(\kappa L) \\ P_2(L) &= P_1(0)\sin^2(\kappa L) \end{aligned} \tag{5.1}$$

where $P_1(z=0)$ is the launched power, z is the length coordinate, L is the length of the coupling region, and κ is the coupling coefficient that depends on the wavelength and other physical parameters.

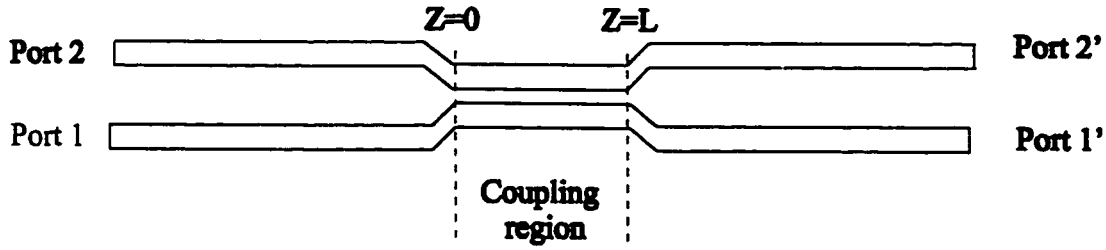

Figure 5.1 Basic structure of fiber coupler

Thus, the power transferred between the waveguides varies from zero to unity. By proper design the coupler provides two output beams with a predetermined power distribution. The wavelength dependence of κ is an important feature, by which the coupler can be made to deliver almost all the power at one wavelength at one output and almost all the power at another wavelength to the other output. Such devices are referred to as wavelength division demultipexers/multipexers (WDM).

Directional couplers could be made by polishing [1] single-mode fibers to achieve close proximity of the fiber cores. The polished-type fiber coupler is made by burying an optical fiber in a curved groove in a glass block and then polishing the block to remove a semicircular portion of the cladding. Two such blocks are then placed together so that the polished areas are in contact, with a little index-matching fluid over the contacting area. The drawback of the polishing method is the lengthy process and instability due to the structure. Fused tapering is another popular method to make fiber coupler, which is easy, and fast to fabricate and package. To fabricate the fused-taper-type fiber coupler [2], the resin coating of two fibers is removed along a short section of a few centimeters. The fibers are then twisted together, heated and drawn while the throughput and the coupled powers are monitored. Figure 5.2 shows the relationship between the coupling ratio and the drawn length for a fused tapered coupler [3]. The solid and dashed lines indicate the coupling ratios at wavelengths of 1.31 and 1.54 μm, respectively. It is clear that a 1.31/1.54 μm WDM coupler can be obtained when the drawing process is stopped at a drawn length of 4.5mm.

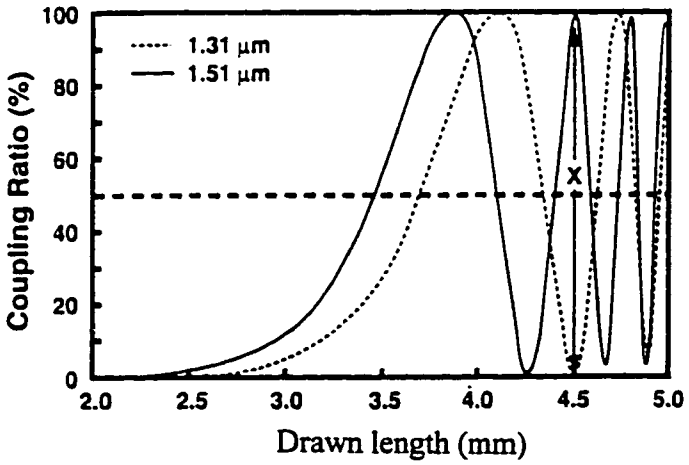

Figure 5.2 Relationship between coupling ratio and drawn length

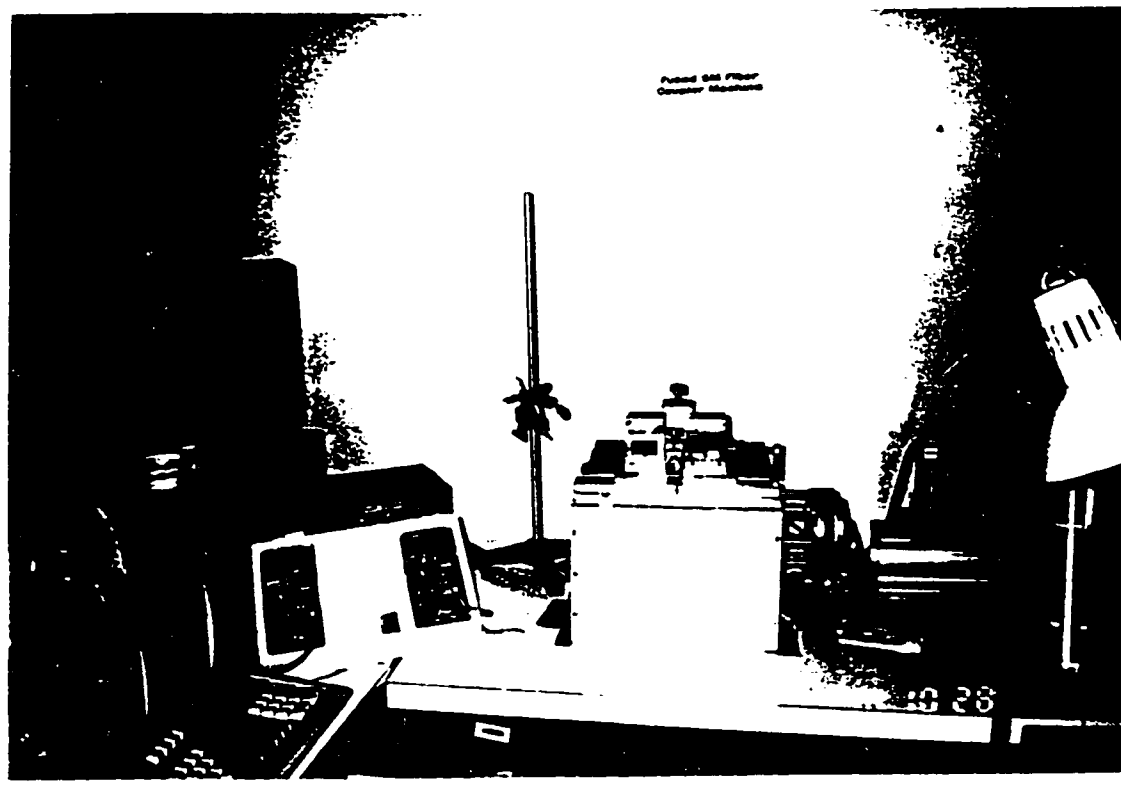

Figure 5.3 Workstation of single mode coupler machine

All the couplers in our lasers are homemade by a fused SM fiber coupler workstation in our lab, whose picture is shown in Fig.5.3. The fabrication technique and a detailed fabrication method by using the machine may be found in Ref.4. The insertion losses of the couplers made are usually less than 0.1 dB at any desired coupling ratio. The WDM used is from E-TEK. Table 5.1 shows the details of WDM^1 and WDM^2 coupler.

Table 5.1 Specifications of WDM coupler

WDM^1:

Wavelength	I.L. (dB)	Isolation (dB)	P.D.L. (dB)
980 nm	0.11	> 20	< 0.1
1550 nm	0.19	> 20	< 0.1

WDM^2:

Wavelength	I.L. (dB)	Isolation (dB)	P.D.L. (dB)
980 nm	0.06	> 20	N/A
1550 nm	0.07	> 20	N/A

Note: I.L – Insertion Loss; P.D.L – Polarization Dependent Loss

5.1.2 Fiber Bragg Grating

Fiber Bragg grating (FBG), just as its name implies, is a fiber device incorporating a grating structure in a fiber. It is a unique device for use as wavelength-selective reflection mirrors, optical notch filters, and optical taps. Figure 5.4 shows the model of the Bragg reflector. There are coupled modes travelling in opposite directions in the same waveguide. According to the coupled-mode theory, the reflectivity of a lossless FBG can be expressed as

$$R = \tanh^2(\kappa_B L) \tag{5.2}$$

where κ_B is the strength coupling coefficient and L is the length of the FBG. The central wavelength, i.e., where strong reflection occurs is determined by

$$\lambda_B = 2 \cdot n_{eff} \cdot \Lambda \tag{5.3}$$

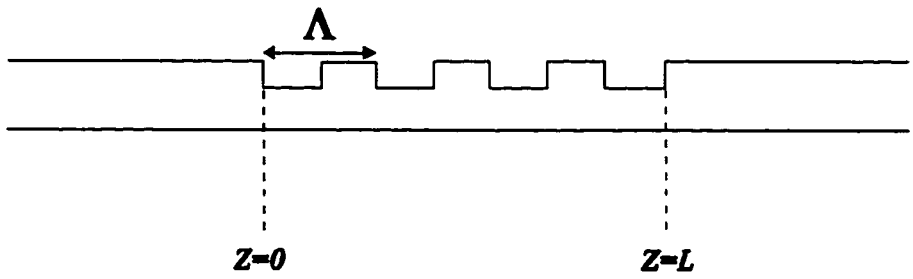

Figure 5.4 Model of the Bragg reflector

where n_{eff} is the effective refractive index and Λ is the period of the structure. Obviously, the bandwidth of the FBG is dependent on the $\kappa_B L$.

Writing a Bragg grating in a fiber, actually a photosensitive fiber, can be done with UV light [5]. It has a great advantage because of its low insertion loss, ease of fabrication, and high reflectivity at the Bragg wavelength.

The major method for fabricating a FBG is the side writing technique [6], in which the fiber is exposed to a UV interference pattern from the side. The interference pattern causes the refractive index to change because of the photosensitive effect, which results in a Bragg structure in a fiber. Such a technique enables us to fabricate a FBG with any designed Bragg resonance wavelength. Figure 5.5 shows a typical side writing fabrication method with a phase mask. The UV-induced refractive index change could be as big as 10^{-2}.

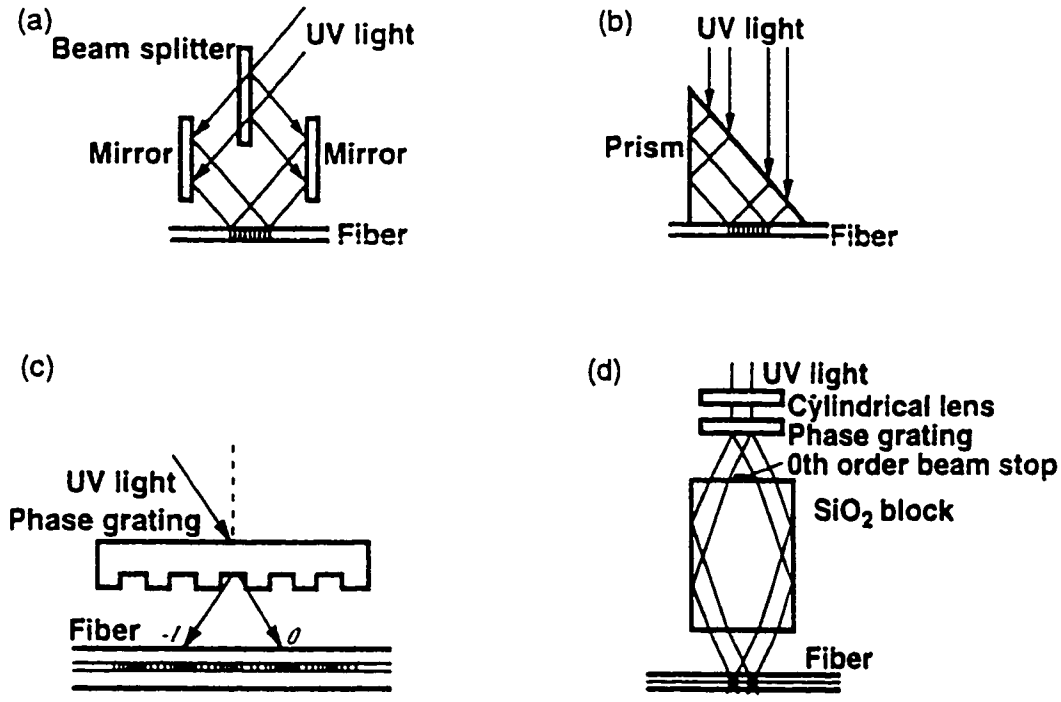

Figure 5.5 Fabrication method of UV-written grating

There are three fiber Bragg gratings (FBG^1, FBG^2, and FBG3) used in our laser systems. Table 5.2 lists the specifications of the three gratings. Their transmission spectra are shown in Fig.5.6.

Table 5.2 Specifications of the gratings

	Central wavelength	reflectivity	3-dB bandwidth
FBG^1	1549.05 nm	99.9%	0.1 nm
FBG^2	1550.4 nm	99.94%	0.1 nm
FBG^3	1555.28 nm	99.4%	32 pm

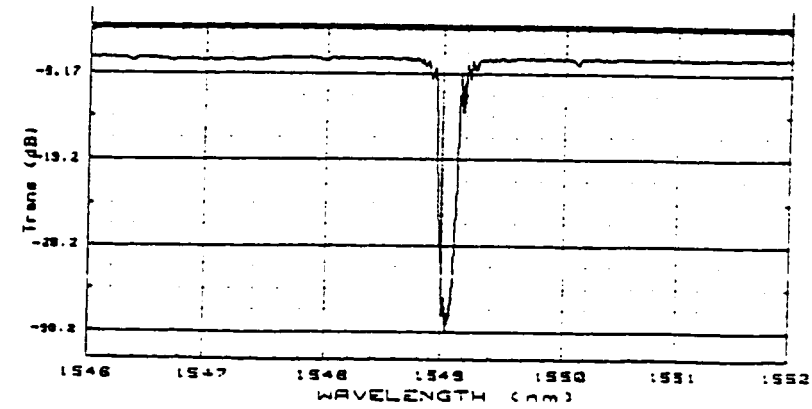

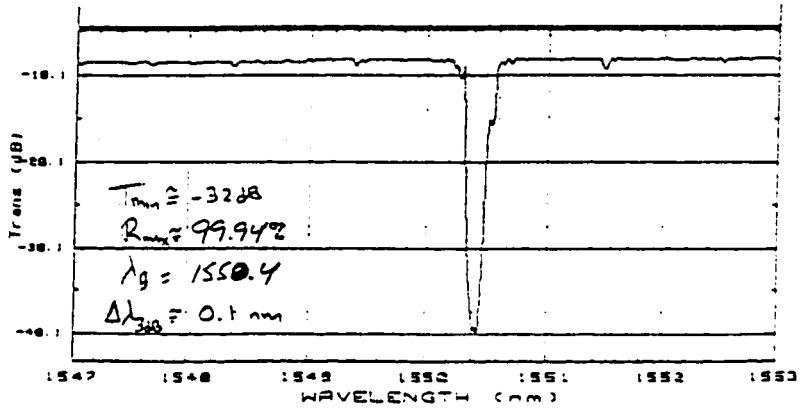

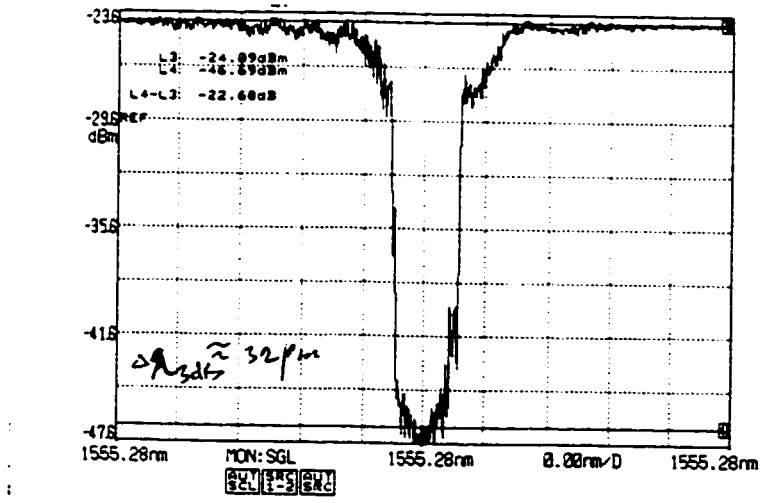

Figure 5.6 Spectrum of the FBGs

5.1.2 Polarization Controller

It is well known that in a fiber ring resonator, the resonant frequency and amplitude are strongly dependent on the state of polarization (SOP) of the light circulating inside the cavity. So it is important to have a polarization controller (PC) to adjust the SOP of the light in the fiber cavity. In classical optics, PC is formed by a combination of rotatable birefringent phase retardation plates, usually quarter-wave plates (QWP) or half-wave plates (HWP). These work by changing the relative phase of the components of the electric field of the light that lie in the direction of their fast and slow axes respectively.

In all-fiber systems, phase retardation plates could be made with the fiber itself. This is because birefringence is induced whenever a fiber is subjected to some type of stress. A lateral stress, either by bending or squeezing the fiber, will induce a linear birefringence [7]. Twisting the fiber on the other hand will cause circular birefringence. Thus, it is by deliberately bending the fiber a controlled amount that one can create the desired fractional wave plates.

For a fiber loop of radius R with an outer cladding radius r as shown in Fig.5.7, the linear polarization state in the plane of the loop encounters a higher index than that perpendicular to this plane by an amount Δn, given by

$$\Delta n = \frac{n^3}{4}(1+\sigma)(p_{12} - p_{11})(\frac{r}{R})^2 \tag{5.4}$$

The total phase change of the loop could be integrated along the fiber loop, then we have

$$|\Delta n| \cdot 2\pi NR = \frac{\lambda}{m} \tag{5.5}$$

Where N is the number of turns of the loop and m is the fractional number.

From Eq. (5.5), one can see that any desired λ / m fractional wave plates could be achieved by properly selecting the number of turns N of the loop and the radius R.

In addition, rotation of the plane of the loop will directly rotate the orientations of the principal axes of the fiber, which gives the analogous behavior of a classical fractional wave.

Figure 5.8 illustrates the configuration of the standard PC, formed by three coils (QWP) in laser system. The fiber is wrapped around aluminum disks machined to a correct radius to create a QWP. These disks are clamped in a cradle that allows them to be rotated by approximately ± 80 degree. In general, only two QWP's are necessary to transform any input polarization to any desired output polarization. However, if either of the fractional waveplates do not induce phase retardation exactly, then the two-QWP PC will be unable to produce all possible output polarizations, which is undesirable. On the other hand, in case of three-QWP PC, any of the three waveplates may be considered to be redundant. This redundant one can compensate for any problem related to one specific QWP, for instance, circular birefringence introduced by rotating the waveplates.

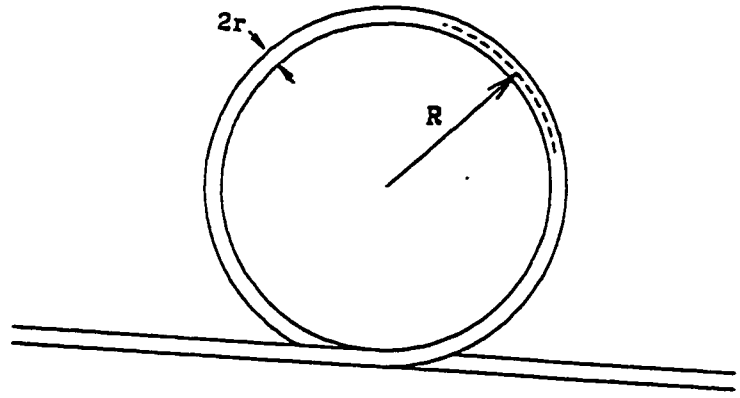

Figure 5.7 Birefringent fractional wave loops

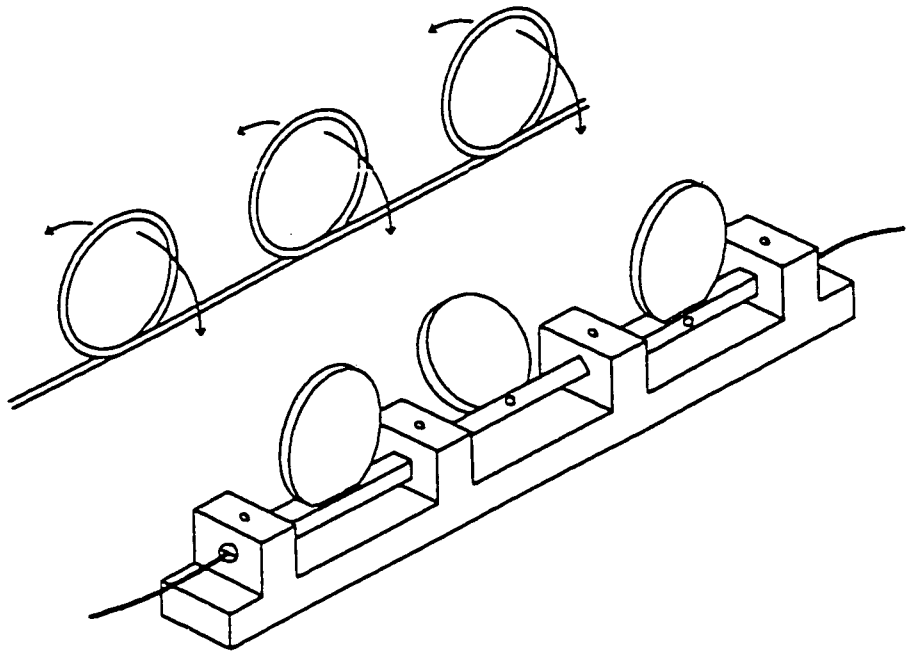

Figure 5.8 Construction of the all-fiber polarization controller

5.1.3 Gain Medium, Pump Source and Splicing

An optical fiber laser uses light at one wavelength as energy pump source to create light at a second wavelength with a gain medium. The most important elements for the fiber laser are the gain medium and the pump source.

The gain medium absorbs the pump energy and transfers the energy from pump to signal laser. In our EDFLs, the gain was provided by Er^{3+}:Al/Ge/P doped silica based fiber, which came from the National Institute of Optics. Table 5.3 lists the specification of the EDF.

Table 5.3 Specifications of EDF

Concentration	Er:3100 *ppm*
Absorption	980nm@11.8dB/m 1535nm@17.0dB/m
Core diameter	3.5 *μm*
Mode field diameter	6.1 *μm*
Confinement factor	0.5
Cutoff wavelength	875 ± 50 *nm*

A pump source supplies energy to the rare-earth-doped fiber. The required pump wavelengths depend on the rare-earth ion. For erbium-doped fiber, as mentioned earlier, 980 nm and 1480 nm are the two main pump wavelengths. So far the most commonly used pump sources for EDF are semiconductor lasers, i.e., laser diode (LD), such as 980 nm InGaAs-GaAs and 1480 nm InGaAsP-InP laser diodes. This is because they are compact, powerful, and moreover, fiber-pigtail LDs are fiber compatible. The drawback of a LD is wavelength instability, caused by reflection, thus degrading the laser performance. In particular, low reflectivity front-facet coating increases their sensitivity to outside reflection. One popular way to solve this problem is LDs with a wavelength-selective external cavity structure to stabilize the lasing wavelength, as shown in Fig. 5.9.

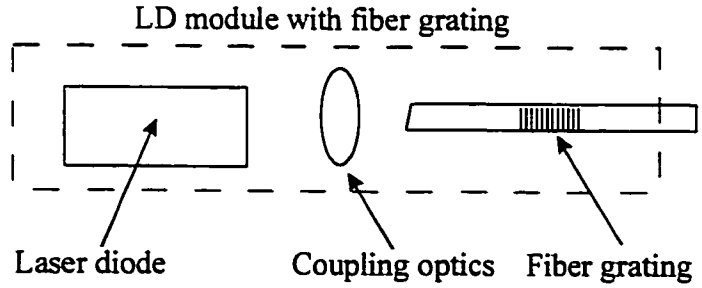

Figure 5.9 Schematic configuration of a wavelength-stabilized LD with a fiber grating

The 980 nm laser module used is from SDL Optics Inc. The pigtailed LD with TEC (thermal-electrical controlled) mode is stabilized by a fiber grating driven by a LDC-3722 laser diode controller from ILX Lightwave. The center wavelength of the LD is at 975.37 nm. Figure 5.10 shows the optical spectrum of the LD. The maximum driving current is 250 mA, at which about 100 mW output power could be provided. The relationship between the output power and the LD current is shown in Fig. 5.11, which appears linear.

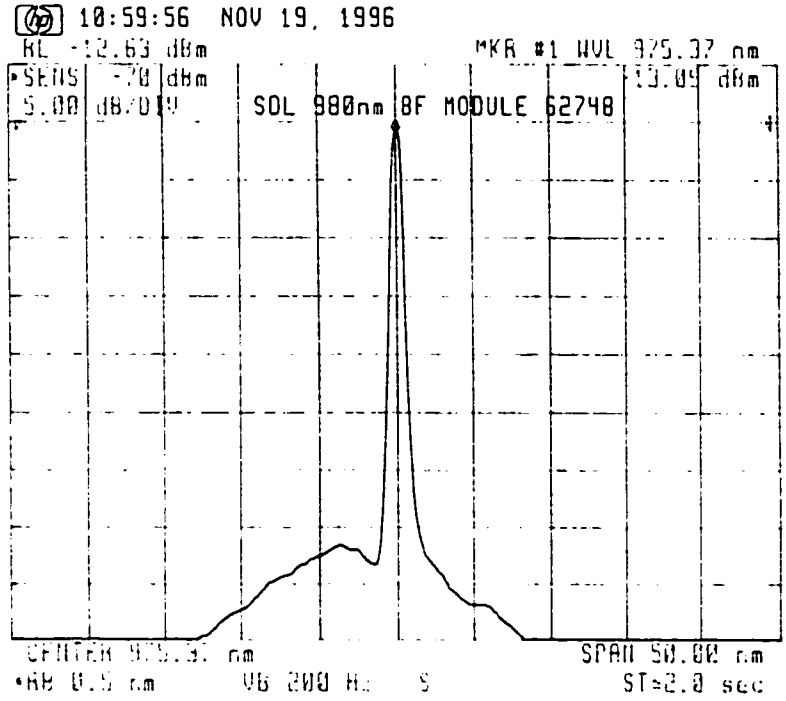

Figure 5.10 Optical spectrum of 980 nm laser module

A splice machine is one of the most important pieces of equipment for fiber-related devices. We use an automated fusion splicing set NT7L30AC (from Siecor) to splice the standard SMF-28 fibers, and SMF-28 fiber with erbium-doped fiber. Standard fibers spliced together have an average of estimated loss of less than 0.09 dB. A bigger loss is expected when a standard fiber is spliced with an erbium-doped fiber because of

the small mode field diameter of EDF. However, it is found that the loss may be reduced by increasing the duration of the arc. The longer arc time allows significant diffusion of the highly doped core, which rapidly reduces the effective index and increases the core diameter. By using this method, it is estimated that the average splicing loss in the laser systems could be reduced to less than 0.2 dB.

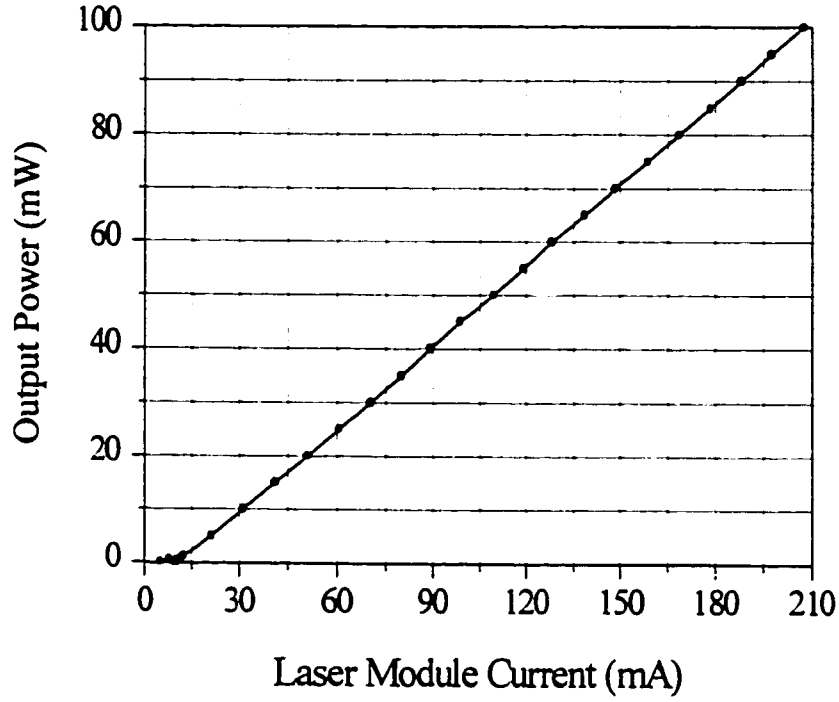

Figure 5.11 Output power as a function of driven current

5.2 Single-wavelength Erbium-doped Fiber Laser

In previous chapters, two fiber resonators (FRRER and CRRER) were proposed and analyzed. The theoretical results show that by using such resonators in fiber lasers, unidirectional fiber laser oscillation may be produced, without using optical isolators. In this section, we shall implement the two resonators in constructing fiber lasers.

5.2.1 Single-Ring EDFL with an external Grating

Since the first invention and demonstration of FBG in1989, it has become a very important and unique element in various filters, fiber amplifiers, fiber lasers, WDM systems, etc. FBG is a reflection-type filter with a narrow bandwidth, so it is widely used as a cavity mirror in FP-cavity fiber lasers. In addition, a travelling-wave cavity design with Sagnac-type loop configuration is designed to allow the use of FBG in travelling-wave fiber lasers. In this section, we introduce a new configuration which allows FBG to be used in a ring cavity design, i.e., single-ring EDFL with an external grating.

5.2.1.1 Experimental Configuration

A schematic diagram of the fiber laser is shown in Fig.5.12. Pump radiation from a 980 nm pigtail laser diode is coupled into the ring cavity via a polarization-insensitive WDM. Optical gain is provided by a 3.7-m long piece of erbium-doped Al/Ge/P fiber. An FBG is spliced to one of the free ends of the output coupler. With the help of an external grating, part of the amplified spontaneous emission (ASE) from the cw direction is injected back to the ccw direction, while the ASE in the ccw direction has no effect on the cw direction. Therefore, some non-reciprocal losses between the two directions are introduced into the ring cavity, which ensure unidirectional oscillation in the ccw direction without the need of optical isolators.

The difference in the steady-state photon-flux density $\Phi(\gamma)$ between the ccw and cw directions is given by [8]:

$$\Phi_{ccw}(\gamma)-\Phi_{cw}(\gamma)=\frac{N_0}{2\tau_{sp}}\left[\frac{1}{\alpha_{cw}}-\frac{1}{\alpha_{ccw}}\right]=\frac{N_0\Delta\alpha}{2\tau_{sp}\alpha_{cw}\alpha_{ccw}} \tag{5.6}$$

where α_{ccw} and α_{cw} are the loss coefficients for the ccw and cw directions, N_0 is the steady-state population difference between the metastable level and the ground level in the absence of amplification, and τ_{sp} is the spontaneous lifetime. So unidirectional operation can be enhanced by increasing the loss difference between the two directions.

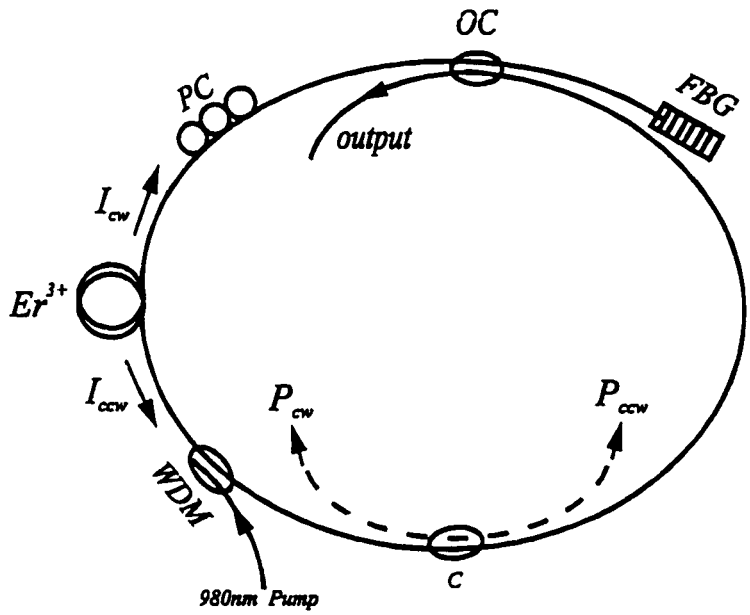

Figure 5.12 A nonreciprocal single-ring laser configuration

OC: output coupler; C: monitor coupler; PC: polarization controller; FBG: fiber Bragg grating; WDM: wavelength division multiplexer.

As shown in Fig.3.4, the loss difference increases with increase of the coupler coefficient; however, the lasing threshold will also be increased. A coupler with 10% coupling coefficient was used. In this configuration, one may notice the fiber ring in Fig. 5.12 is cross-coupled instead of direct-coupled in Fig.3.2. So the effective coupling ratio of the coupler should be treated as 90%, which corresponds to about 10-dB loss difference according to Fig.3.4. The reason for using a coupler with 10% coupling efficient instead of 90% is because fused coupler with lower coupling coefficient can be

more easily be made with lower insertion loss than coupler with higher coupling coefficient. The grating FBG[1] used had a peak reflectivity of 99.9% and a bandwidth of 0.1 nm centered at 1549.05 nm. It serves not only as a feedback reflector, but also as a mode selector, as will be seen in next section. A polarization controller was used to control the polarization of the propagating light. The round-trip laser cavity length in the ccw direction was about 13 m, corresponding to a passive mode spacing of 14.5 MHz.

To confirm the unidirectional operation in the nonreciprocal fiber ring cavity, a monitor coupler with a coupling coefficient of 1.5% was incorporated into the cavity. It is worthy to mention that the back-reflections from the ends of the output coupler and monitor coupler are detrimental. Although reflections from the end of the output coupler could be ignored because of the small coupling ratio, they could introduce inaccuracies into the measurement of the powers in the ccw and cw directions. To prevent the back-reflections, we spliced an optical isolator with 41-dB isolation to the end of the output coupler. While one end of the monitor coupler is connected to a detector, the other end is dipped into index matching liquid.

5.2.1.2 Results and Discussions

We first examined the power loss difference between the ccw and cw directions. The power meter used is an FOT-22AX from EXFO. The spectra of the outputs in the two directions, measured at the two ports of the monitor coupler, are shown in Fig.5.13. The two outputs have similar spectra. The figure shows that the output power difference was as high as 37 dB. This result demonstrates that with the help of FBG[1], a single-ring configuration without optical isolator can be as effective a unidirectional device as a ring cavity with optical isolators.

The laser output power as a function of pump power is plotted in Fig. 5.14. It shows that a maximum output power of 19.6 mW for 70 mW of incident pump power was obtained. The slope efficiency is 31%, with a laser threshold of 10 mW. Lower threshold could be expected by using an OC with a larger coupling coefficient. The laser output spectrum measured by an HP optical spectrum analyzer (OSA) is shown in Fig.5.15. This measurement was limited by the resolving power of the spectrum analyzer, which was 0.08 nm. By appropriate adjustment of the polarization controller, the spectrum was very stable. The lasing wavelength was measured to be 1548.5 nm, nearly coinciding with peak wavelength of the FBG[1]. The subtle difference of the two wavelengths is attributable to the temperature difference.

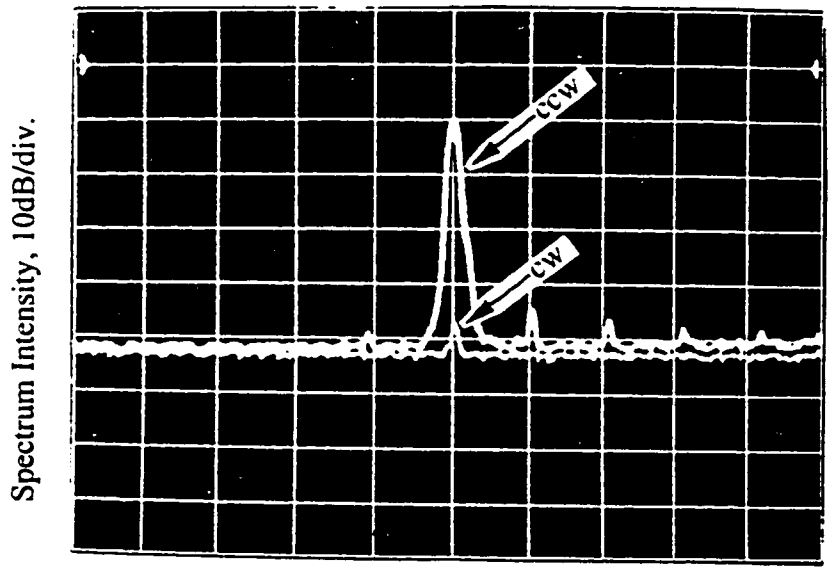

Span=20nm, res.=0.08nm, center wavelength=1548.5nm

Figure 5.13 Output spectra from the two ports of the monitor coupler

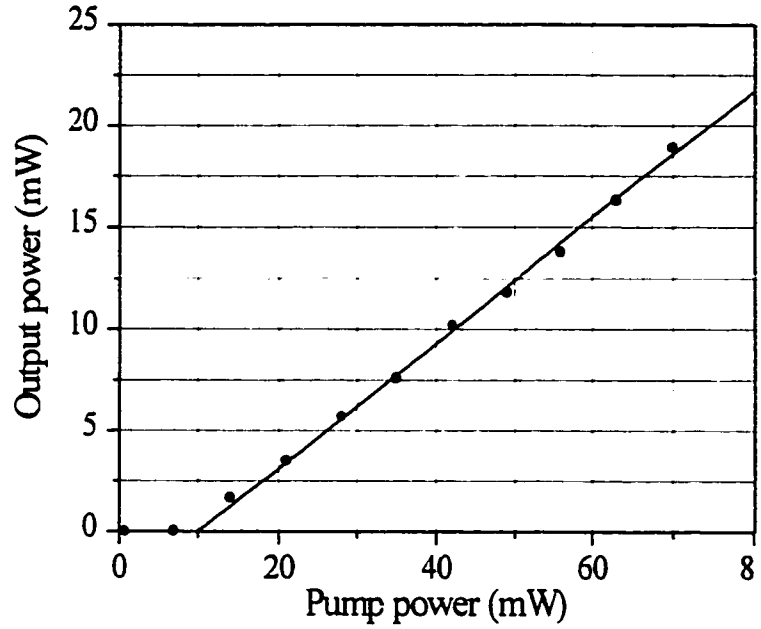

Figure 5.14 Laser output power as a function of diode pump power

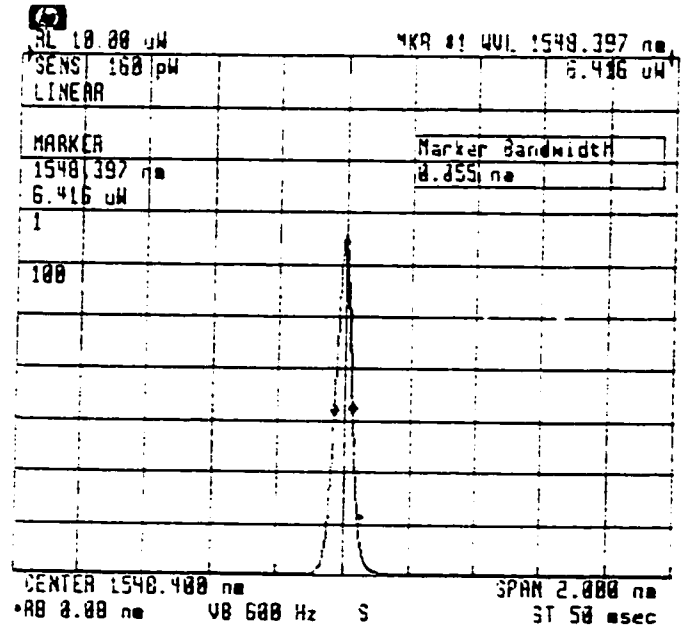

Figure 5.15 Optical spectrum of the laser output from HP OSA

To examine the spectrum of the fiber laser with high resolution, initially, a homemade scanning fiber ring interferometer (FSR = 48 MHz, Finesse = 21) was used. The structure of the interferometer and the principle of operation are given in appendix E. Single-mode operation was observed, but the modehops occurred nearly all the time. Figure 5.16 shows a scan over one FSR at one moment and only one mode was present. But we are not sure if the mode-hopping is attributed to the laser itself or the drift of the interferometer due to the change of the fiber ring length. Later, a confocal FP scanning interferometer (from Melles Griot) was employed to confirm the mode structure of the laser. The interferometer has a FSR of 300 MHz and a higher finesse of 344, resulting in a resolution of 872 kHz. Single mode was observed, but not robust. The mode jumped randomly, and two-mode and three-mode operations were also observed frequently.

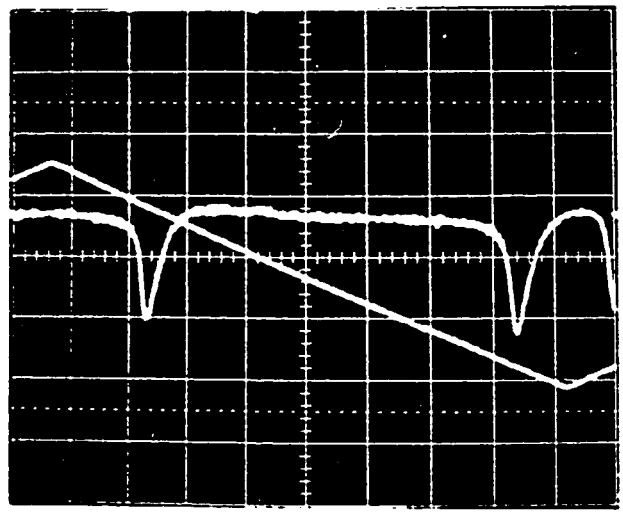

Figure 5.16 Output spectrum of the laser from interferometer

Let us look at the mode-selective mechanism of the laser. The grating confines possible modes within about 13.3 GHz region. The ring cavity length of 13 m corresponds to a FSR of 14.5 MHz, so there could be nearly one thousand possible oscillating modes within the confined region, which implies weak discrimination of the

modes in the central region. Consequently, the longitudinal mode could easily jump or possibly multi-modes could appear.

Obviously, this situation may be improved by increasing the FSR of the ring cavity, consequently, suppressing the number of the possible oscillating modes, which will be covered in next section.

5.2.2 Double-Ring EDFL with an external Grating

In this section, we propose a new double-ring resonator with an external grating, based on CRRER to implement the EDFL. The new configuration is used to increase the resultant FSR of the compound ring resonator, as shown in chapter 4, which could be obtained by either choosing the lengths of the two rings nearly equal or widely different. It is shown [9] that the case with widely different lengths of the two ring cavities is a preferred choice because of the insensitivity to the external disturbance.

5.2.2.1 Experimental Configuration

The configuration of the proposed EDFL is shown in Fig. 5.17. A primary ring and a secondary ring are formed by two couplers C_1 and C_2. The primary ring has the required components, i.e., a 3.2-m erbium-doped fiber and a polarization controller. The long primary ring is used to provide large gain, while the secondary ring is made small to increase the resultant FSR. The lengths of the primary and secondary rings are about 16 m and 2 m, giving FSR of 12.5 MHz and 0.1 GHz, respectively. The ratio of the lengths of the two cavities is about 8:1. Obviously, by using the second ring, the resultant FSR of the compound ring is substantially increased to 0.1 GHz, corresponding to 8 times the FSR of the single primary ring. An external fiber grating FBG is connected to the free end of the coupler C_1. It serves as a coarse mode-selector, and more importantly, as

described in chapter 4, it introduces a nonreciprocal loss of the cavity between the ccw and cw directions. Thus, the undirectional operation would be favored in the ccw direction, without the use of optical isolators. The grating FBG[3] used has a reflectivity of 99.4% at wavelength $\lambda = 1555.3\,\text{nm}$ with a 3-dB bandwidth of 32 pm. The coupling coefficients of the two couplers k_1 and k_2 are 92:8 and 18:82, corresponding to about 7-dB loss difference. The coupling coefficients with $k_1^b - k_2^s$ (big k_1 and small k_2) are chosen, according to the analysis in chapter 4.

The laser was pumped through a WDM[1] coupler by the pigtailed 980 nm laser diode. The polarization controller was included in the primary cavity to manipulate the polarization of the propagating light. A monitor coupler with 1.5% coupler ratio was inserted to measure the power loss difference between the two directions. The laser output was extracted through coupler C_2, which is spliced with an optical isolator (isolation: 41 dB) to prevent the back-reflection.

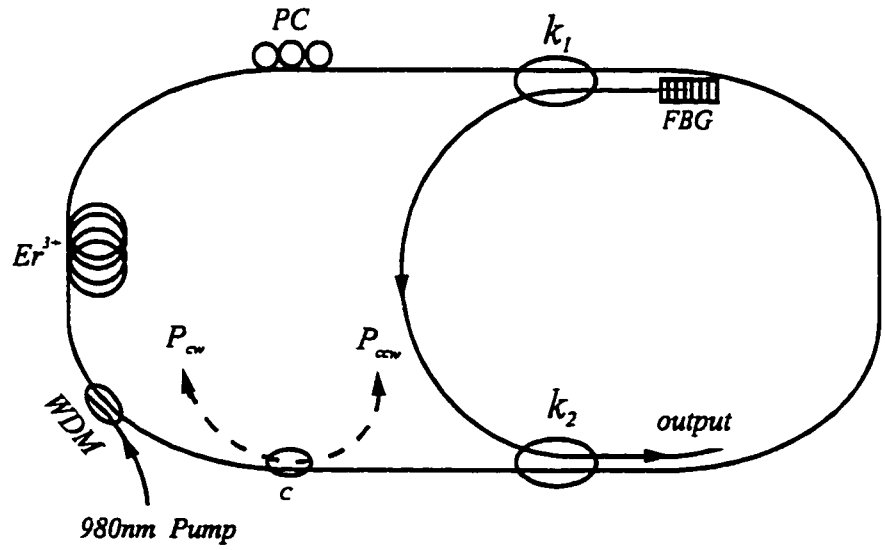

Figure 5.17 The Scheme of the double-ring EDFL with an external grating

5.2.2.2 Results and Discussion

The output power characteristics of the laser is illustrated in Fig. 5.18. The output power of 13.5 mW was obtained for an incident pump power of 59 mW. The slope efficiency was 27% with a lasing threshold of 9 mW. The slope efficiency and lasing threshold in this configuration is slightly lower than that in the single-ring EDFL in Fig.5.12. The former is due to additional insertion loss from the other coupler, while the latter is due to the large effective reflectivity of the compound ring (I_{6a}: ~ 20%, as shown in Fig. 4.14(b)), compared with ~ 10% reflectivity in single-ring EDFL.

The output wavelength was measured to be 1555.25 nm, which coincides with the peak reflectivity of the grating FBG[3], as expected. Figure 5.19 shows the optical spectrum trace of the fiber ring laser, measured by HP optical spectrum analyzer with a resolution of 0.08 nm. The laser was very stable within this resolution. Figure 5.20 shows a scan of the lasing line at the center of the spectrum, taken over a 40 s period. From fig.5.20 it can be seen that there is almost no drift in wavelength and in amplitude.

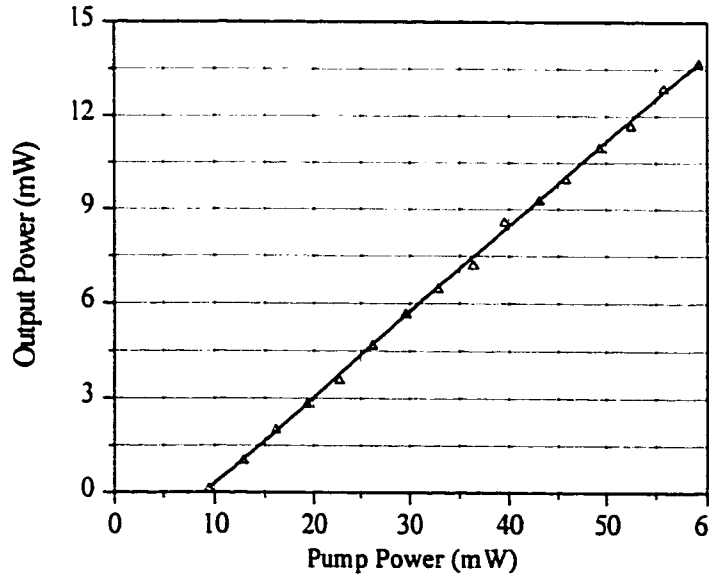

Figure 5.18 Fiber laser output power as a function of launched power

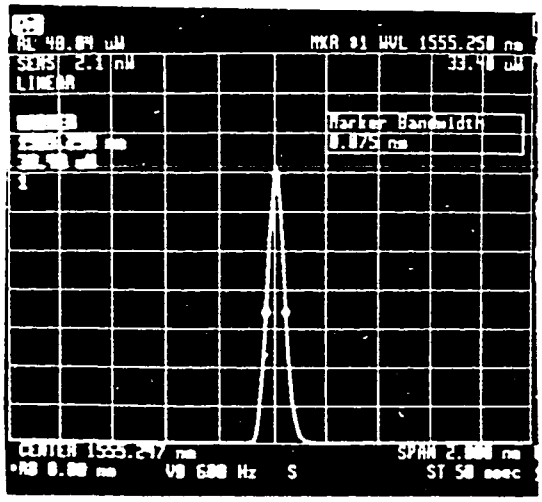

Center: 1555.247 nm Span: 2 nm Marker Bandwidth: 0.075 nm

Figure 5.19 Fiber laser output spectrum from OSA

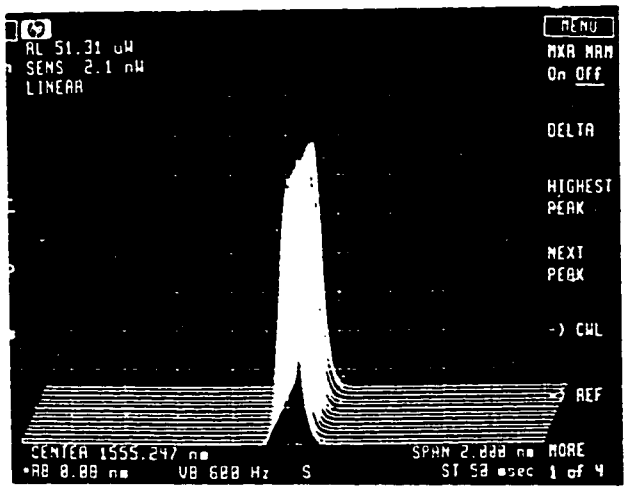

Figure 5.20 Scans of the lasing lines at center wavelength over 40 s

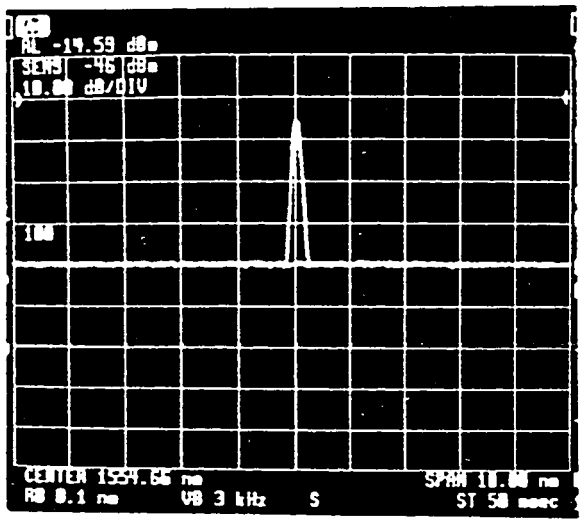

Figure 5.21 Output spectra for the ccw and cw directions

The output spectra of the ccw direction and cw direction in the monitor coupler are measured and shown in Fig. 5.21. It can be seen that there is about 35 dB power difference between the two directions. We observed that for different pump powers, the output power difference remained almost constant. This experimental result demonstrates the uni-directionality of the double-ring EDFL with an external grating.

Again, the confocal FP scanning interferometer was employed to examine the longitudinal mode structure of the fiber ring laser. The interferometer has an FSR of 300 MHz and a finesse of 344, giving a resolution of 872 kHz, which was high enough to resolve the individual longitudinal mode of the fiber laser. Figure 5.22 shows the interferometer trace scanned over one FSR; it confirms single-frequency operation. No evidence of multiple longitudinal mode operation was observed, which was an improvement over the case of the single-ring EDFL reported in last section. This was because there was one mode selector in this case more than the last described in the last section.

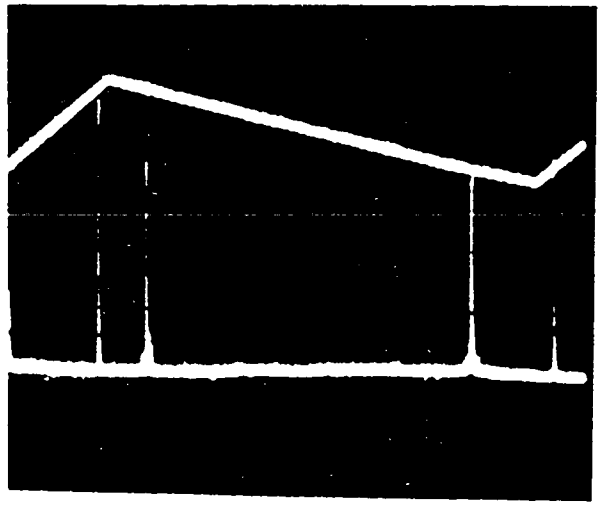

Figure 5.22 Laser spectrum from FP interferometer

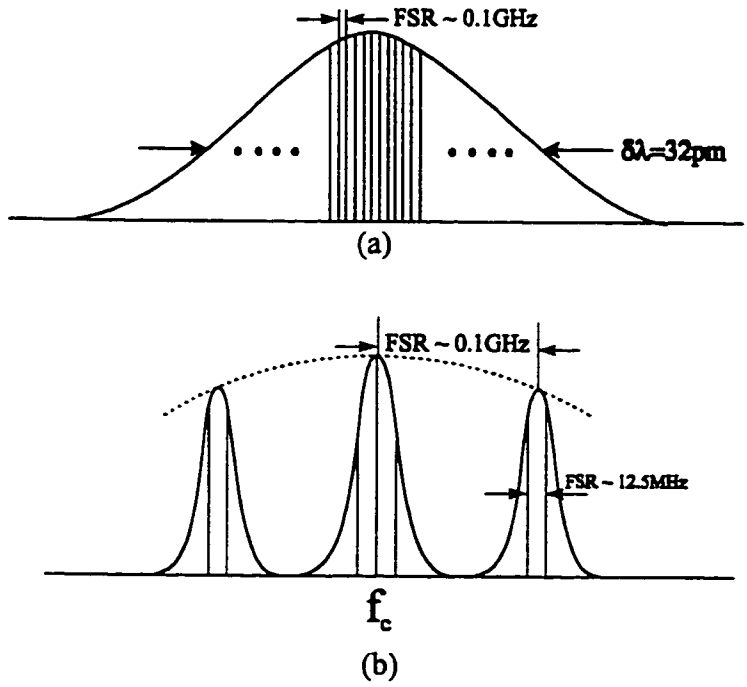

Figure 5.23 Different wavelength-selective mechanisms in the ring laser

Figure 5.23 shows several wavelength selection mechanisms in the laser. The grating serves as the first coarse mode selector. It has a 3 dB bandwidth of 32 pm, which corresponds to approximately 4.3 GHz spectral region, so only within this region lasing may occur because of low loss. The next mode selector is the secondary ring cavity. At resonance, it produces a periodic cavity loss with 0.1 GHz spacing. Hence, about 43 possible oscillating modes are confined by the grating, as shown in Fig. 5.23(a). Finally, the second ring further reduces the number of the possible oscillation mode by spacing about 12.5 MHz from the primary cavity mode [see Fig. 5.23(b)], which will ensure that only the central resonant mode with a maximum amplitude (i.e., minimum loss) f_c is able to oscillate. Thus, the capacity of the mode-suppression is significantly enhanced. Although the laser operated on robust single-longitudinal mode, mode-hopping to neighboring modes was still observed sometimes, which is due to the external disturbances such as temperature, vibration inducing the change of the fiber cavity length, as well as the fiber grating. It is believed that a more stable operation may be obtained by thermally and mechanically stabilizing the laser, or further decreasing the cavity length of the second ring.

5.3 Dual-wavelength Erbium-doped Fiber Laser

In the last section, we discussed the EDFL with only one lasing wavelength. EDFLs producing more than one wavelength are of great interest for wavelength division multiplexed (WDM) communication systems, as mentioned in chapter 1. In this section, we start with an introduction on the review of the multi-wavelength EDFLs, followed by the proposed configuration and the experimental setup. The results and discussion are given at the end.

5.3.1 Introduction

Multiple wavelength EDFLs have been demonstrated by a number of researchers [8-18]. Fabry-Perot and ring resonator configurations have been investigated by using one or more filters to define the multiple lasing wavelengths. Such filters may have different forms, such as fiber Bragg gratings, bandpass filters, FP etalons, and comb filters based on mode-beating either in a birefringent fiber or a multimode fiber. In order to achieve gain at several wavelengths simultaneously, various techniques have been used to create multi-wavelength lasers in EDF.

It is well known that an EDF has a large homogeneous linewidth at room temperature, which means the gain will be clamped by the cavity loss at only one lasing wavelength. So one of the techniques to achieve multiple wavelength operation is to cool the EDF to the cryogenic temperature to reduce the homogeneous linewidth of the EDF and prevent mode competition [10-11]. Furthermore, O. Graydon [12] designed a twincore EDF to provide an inhomogeneous gain medium through macroscopic (mm) spatial holeburning. Triple-frequency operation from the inhomogeneously broadened twincore EDF was reported. Obviously, cooling the EDF is inconvenient, while using a twincore EDF is expensive; it also suffers from very low efficiency.

The use of a different gain medium for each lasing wavelength [13-15] is another technique used to obtain multiple wavelength operation. However, this method requires many optical components, which increase the cost as well as the complexity. Alternatively, one could use a single gain medium, but the cavity losses corresponding to the different wavelengths could be carefully balanced. The advantage of this scheme is simplicity and low cost. Many multi-wavelength oscillations have been demonstrated,

based on this scheme; they include a fiber ring laser using an arrayed-waveguide wavelength multiplexed [16], a ring laser with two cavities [13, 17], a ring laser with fiber Bragg gratings [18-19], and a laser with a Sagnac-configuration [20]. In addition, Brillouin/erbium fiber lasers (BEFL's) have been recently demonstrated as a densely spaced robust multiwavelength laser source [21]. However, the power discrepancies among the different wavelengths limit their applications.

In this thesis, we propose a novel ring cavity configuration for dual-wavelength operation. Only one coupler and two external fiber Bragg gratings are required. The structure was based on the single wavelength EDFL in the last section, as we shall see it in the following section. The lasing wavelengths were determined by the two gratings with a wavelength separation of about 1 nm. Stable dual-wavelength oscillation has been achieved. The benefit of this approach is simplicity, compactness and low cost.

5.3.2 Experimental Configuration

The laser configuration is shown in Fig.5.24. The laser consists of a 3-m section EDF, a WDM, one 90:10 output coupler, a polarization controller and two Bragg gratings. It is similar to the single wavelength EDFL in the last section, but with additional fiber Bragg grating at the other end of the output coupler. The two gratings (FBG^1 and FBG^2) have a 99.9% reflection with 3-dB bandwidth of 0.1 nm at the wavelength of $\lambda_1 = 1549.05$ nm and $\lambda_2 = 1550.4$ nm, respectively.

Referring to Fig.5.24, when the laser is turned on, the ASE light generated in the EDF propagates in both cw and ccw directions. When it reaches the output coupler, part of the light is coupled out and proceeds to the two gratings, which reflect the light back into the laser cavity at the center wavelengths of the gratings.

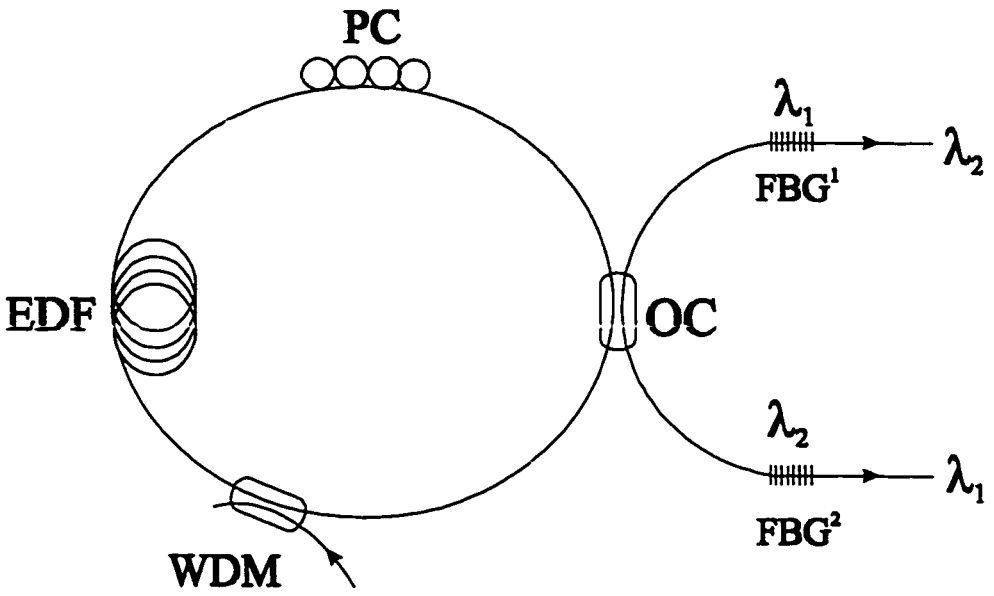

Figure 5.24 Schematic configuration of proposed dual-wavelength EDFL

Because of the two external gratings, the cavity losses for the two wavelengths in the two directions are non-reciprocal. Radiation with wavelength λ_1 will be favored in the cw direction and will come out from grating FBG^2, while that with λ_2 will be favored in the ccw direction and will come out from grating FBG^1. The PC is used to manipulate the polarization state in the laser resonator. In this case, it plays a more important role in balancing the effective gains at λ_1 and λ_2. To avoid reflections from the output ports after the two gratings, each of them is spliced to an optical isolator (41-dB Isolation from E-TEK) and an FC/APC connector (from JDS Fitel) which has a 60-dB return loss.

Laser tunibility can be obtained when the FBG is stretched or heated uniformly. The change in the Bragg wavelength as a function of strain or thermal variation is be given by:

$$\frac{\delta\lambda_B}{\lambda_B} = (1-\rho_e)\varepsilon + (\alpha+\zeta)\Delta T \tag{5.7}$$

where α is the coefficient of linear expansion, ζ is the thermo-optic coefficient, ρ_e is the photoelastic constant, and ε is the applied strain. A common technique to strain FBG is to use a piezoelectric translator (PZT) [20, 22]. By applying a voltage to the PZT, the FBG can be compressed or stretched. In our laser, a simple way was used to tune the laser. Two translation stages were fixed on an iron block and aligned along the moving direction, then two drops of wax were put on the stages. After that, the FBG was mounted on the top of the wax with epoxy. With the help of the wax, the grating can be easily removed from the stages and the wax from the stages. By adjusting either of the stages, the laser can be tuned. We tune both stages with the same amount in order to get a better uniform stretch.

5.3.3 Results and Discussions

The proposed EDFL was pumped by a 980 nm LD through the WDM coupler. By appropriately adjusting the polarization controller, the laser could obtain stable operation in the dual-frequency regime. The output optical spectrum is shown in Fig.5.25. It is clear that the dual-wavelength laser operates in the wavelengths, corresponding to the wavelengths of the gratings. As expected, the lasers at the two wavelengths come out separately, where λ_1 from the FBG^2, and λ_2 from the FBG^1. This is because both gratings have nearly unit reflectivity with a 0.1 nm 3-dB bandwidth, and the wavelength difference of the two gratings is about 1.3 nm. So FBG^1 is almost transparent to λ_2, and FBG^2 to λ_1.

We measured the two output powers, which are plotted in Fig.26. With an incident power of 80 mW, the outputs at λ_1, λ_2 were about 12 and 8 mW, respectively. So the total combined output power was about 20 mW. It is noted that at low pump powers, the output curves exhibit hysteresis behavior with a turning point at 22 mW pump power, and beyond which, the curves exhibit a kind of small oscillations about the straight line. This may be attributed to the inevitable small reflection of λ_2 from FBG[1], and λ_1 from FBG[2]. A similar phenomenon is also mentioned in Ref. 23.

The tuning characteristics were investigated by stretching the FBG[2]. Fig. 5.27 plots the lasing wavelength as a function of extension. A tuning range of 3.7 nm was obtained with an extension of 0.47%. As shown, the wavelength tuning was nearly linear over the tuning range. Stretching the FBG[2] further could increase the tuning range.

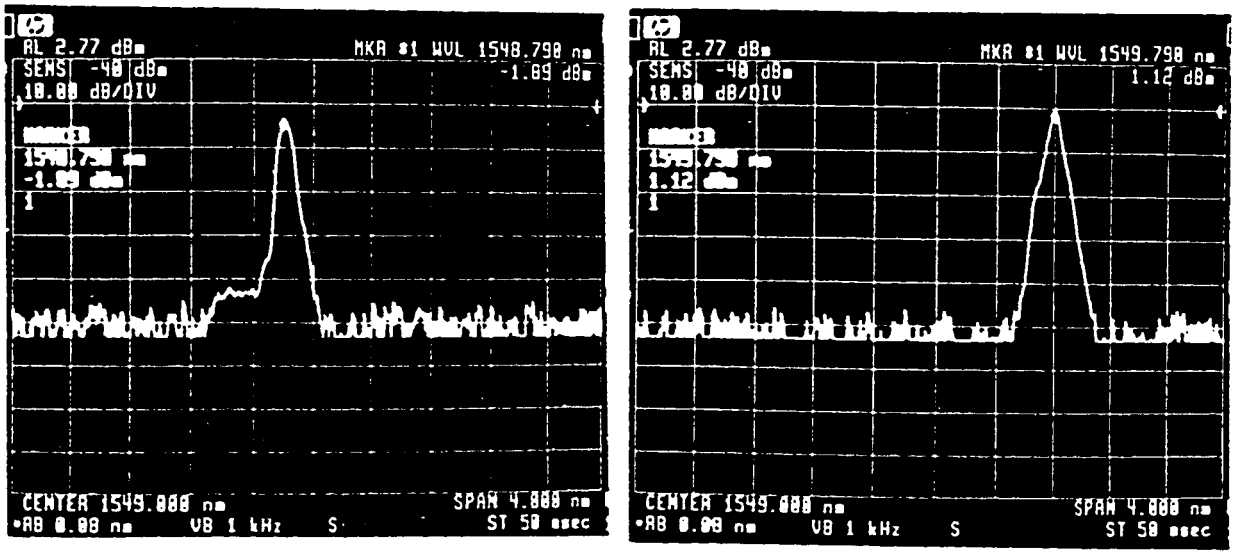

Center: 1549.000nm
Marker: 1548.790nm
(a)

Center: 1549.000nm
Marker: 1549.790nm
(b)

Figure 5.25 Optical spectra of the dual-wavelength EDFL

(a) $\lambda_1 = 1548.790nm$ (b) $\lambda_2 = 1549.790nm$

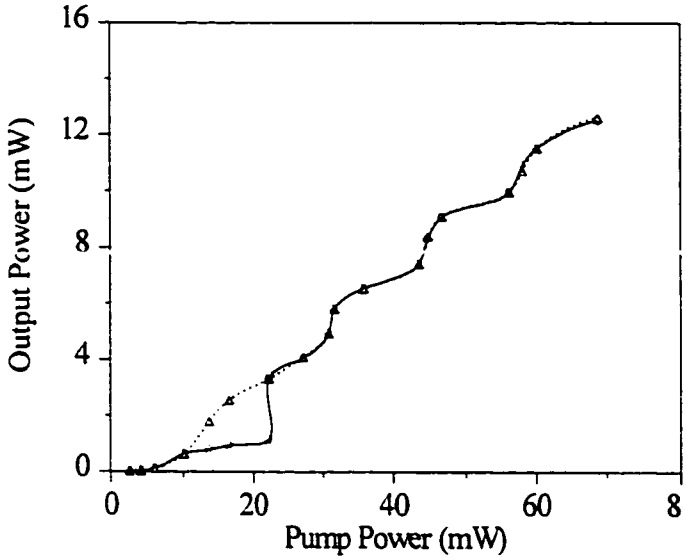

(a)

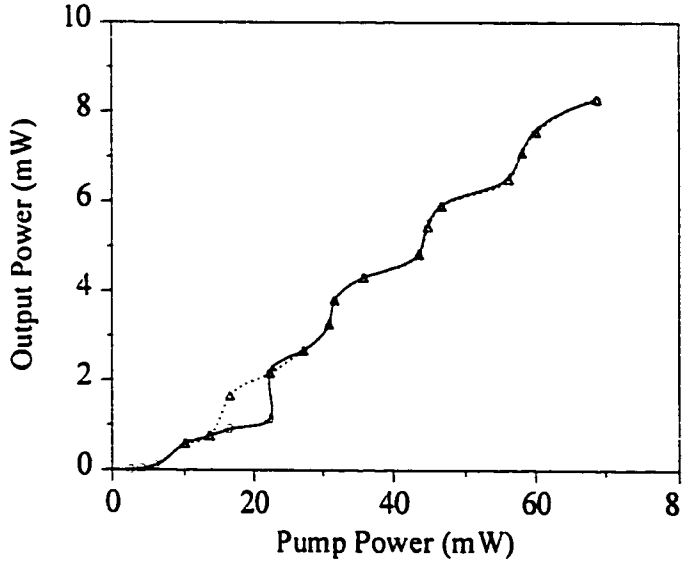

(b)

Figure 5.26 Output power versus pump power

(a) $\lambda_1 = 1548.790nm$ (b) $\lambda_2 = 1549.790nm$

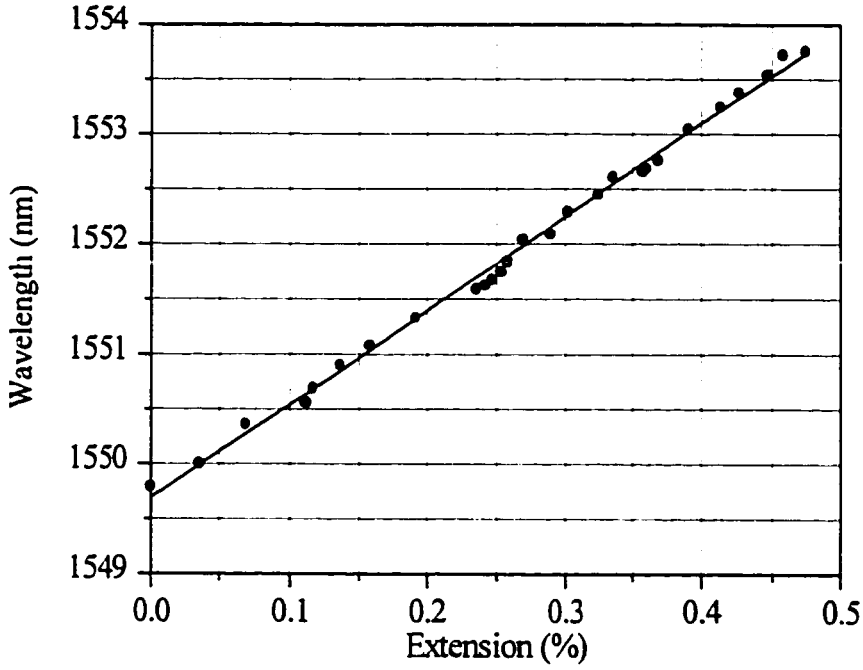

Figure 5.27 Wavelength tuning as a function of the expansion

5.4 Summary

We have demonstrated both single-wavelength and dual-wavelength laser operations. Two travelling-wave fiber lasers working in a single-wavelength region have been implemented, based on the configurations proposed in previous chapters. One is the single-ring EDFL and the other is the double-ring EDFL. They are constructed by incorporating an external fiber grating in a single-ring or a double-ring structure. With the help of gratings, the two EDFLs feature nonreciprocal cavities, and thus give rise to unidirectional lasing operation without the use of optical isolators. In a single-ring EDFL, an output as high as 20 mw with a slope efficiency of 31% was obtained. However, the single-longitudinal-mode (SLM) operation is not robust. The situation is improved in the

double-ring EDFL. It has a compound-ring resonator, and makes use of the vernier effect to effectively increase the resultant FSR, consequently, substantially enhance the mode suppression and ensure SML oscillation. Robust SLM operation is obtained, and the laser has an output power of 13.5 mW with a slope efficiency of 27%. Based on the configuration of single-ring EDFL, a novel dual-wavelength EDFL using two external gratings has been studied. The laser outputs at different wavelengths are separately extracted from the two ports of the output coupler. By stretching the fiber grating, a tuning range of 3.7 nm is obtained with an extension of 0.47%. The single-wavelength and dual-wavelength fiber lasers have considerable potential for a wide variety of fiber-optic communications and sensor applications.

5.5 Reference

1. R.A. Berch, G. Kotler, and H.J. Shaw, "Single-mode fiber optic directional coupler", *Electron. Lett.*, vol.16, pp260-261, 1980.
2. T. Bricheno and A. Fielding, "Stable low-loss single-mode coupler", *Electron. Lett.*, vol.20, pp230-232, 1984.
3. V.J. Tekippe, *Fiber and Integrated Optics*, vo.9, pp97, 1990.
4. R. M. Server, "Fiber coupler, loop reflector, fabry-perot interferometer: fabrication and characteristics", Master's thesis, University of Waterloo, 1997.
5. K.O.Hill, Y.Fujii, D.C. Jonson and B.S. Kawasaki, "Photosensitivity in optical fiber waveguides: application to reflection filter fabrication," *Appl. Phys. Lett.*, vol.32, pp647, 1978.
6. D.Z. Anderson, V. Mizrahi, T. Erdogan, and A.E. White, *Proc. Optical Fiber Communication*, OFC'93, San Jose, PD16, 1993.
7. H.C. Lefevre, "Single-mode fibre fractional wave devices and polarisation controllers", *Electron. Lett.*, vol. 16, pp778-780, 1980.
8. Y.Hua and J. Conradi, "Single-ploarization wavelength-tunable fiber laser with a nonreciprocal catity", *J. Lightwave Technol.*, vol.13, pp1913-1918, 1995.
9. L. Wei and J.W.Y. Lit, "Three-coupler double-ring fiber resonator for lasers", *Microwave and opt. technol. lett.*, vol.12, pp73-77, 1996.
10. J. Chow, G. Town, B. Eggleton, M. Ibsen, K. Sugden and I. Bennion, "Multiwavelength generation in an erbium-doped fiber laser using in-fiber comb filters", *IEEE Photon. Technol. Lett.*, vol.8, pp60-62, 1996.

11. S. Yamashita and K. Hotate, "Multiwavelength erbium-doped fiber laser using intracavity etalon and cooled by liquid nitrogen", *Electron. Lett.*, vol. 32, pp1298-1299, 1996.

12. O. Graydon, W.H. Loh, R.I. Laming and L. dong, "Triple-frequency operation of an Er-doped twincore fiber loop laser", *IEEE Photon. Technol. Lett.*, vol.8, pp63-65, 1996.

13. J.W. Dawson, N. Park and K.J. Vahala, "Co-lasing in an electrically tunable erbium-doped fiber laser", *Appl. Phys. Lett.*, vol. 60, pp3090-3092, 1992.

14. S.V. Chernikov, R. Kashyap, P.F. McKee and J.R. Taylor, "Dual frequency all fibre grating laser source", *Electron. Lett.*, vol. 29, pp1089-1099, 1993.

15. S.V. Chernikov, J.R. Taylor and R. Kashyap, "Coupled-cavity erbium fiber lasers incorporating fiber grating reflectors", *Opt. Lett.*, vol. 18, pp2023-2025, 1993.

16. H. Takahashi, H. Toba and Y. Inoue, "Multiwavelength ring laser composed of EDFAs and an arrayed-waveguide wavelength multiplexed", *Electron. Lett.*, vol. 30, pp44-45, 1994.

17. H. Okamura and K. Iwatsuki, "Simultaneous oscillation of wavelength-tunable, singlemode lasers using an Er-doped fibre amplifier", *Electron. Lett.*, vol. 28, pp461-463, 1992.

18. T. Komukai and M. Nakazawa, "Tunable single frequency erbium doped fiber ring lasers using fiber grating etalons", *Jpn. J. Appl. Phys.*, vol.34, ppL679-680, 1995.

19. S. Liaw, C. Lee, K. Ho and S. Chi, "Power equalized wavelength-selective fiber lasers using fiber Bragg gratings", *Opt. Commun.*, vol. 155, pp255-259, 1998.

20. S. Li, H. Ding and K.T. Chan, "Erbium-doped fibre lasers for dual wavelength operation", *Electron. Lett.*, vol. 33, pp52-53, 1997.

21. S. Yamashita and G.J. Cowle, "Bidirectional 10-GHz optical comb generation with an intracavity fibre DFB pumped Brillouin/Erbium fibre laser", *IEEE Photon. Technol. Lett.*, vol.10, p796-798, 1998.

22. G.A. Ball and W.W. Morey, "Continuously tunable single-mode erbium fiber laser", *Opt. Lett.*, vol.17, pp420-422, 1992.

23. S. Langlois, "S-resonator for fiber lasers", Master's thesis, University of Waterloo, 1997.

Chapter 6

Conclusion

Fiber resonators and erbium-doped fiber lasers are studied theoretically and experimentally.

A basic fiber ring resonator with an external reflector FRRER is presented and analyzed theoretically with regard to the resonant conditions and directionality properties. The optimum conditions for resonance, the intensities, the loss difference between the counter-clockwise (ccw) and clockwise directions (cw) are derived. It has been shown that the behavior of the resonators strongly depends on the coupling coefficients of the couplers and on the losses. The frequency responses of the circulating intensities are of channel-passing types, which make it suitable for building a fiber laser. More importantly, by suitably choosing the parameters of the resonator, the FRRER may offer a high loss difference between the ccw and cw directions, which is essential to produce unidirectional operation without using optical isolators when it is applied to a fiber laser.

Based on the FRRER, a compound ring resonator with an external reflector (CRRER) is proposed. A theoretical analysis of the compound resonator is carried out. It is shown that besides having the same features as the FRRER, its free spectral range can be increased substantially, which is desirable for the development of a single-longitudinal-mode fiber laser.

According to the directionality analysis, a high loss difference can be obtained by choosing either the sets big-k_1 small-k_2 or small-k_1 big- k_2, but the former is the preferred choice because it will produce lower insertion loss. According to the resonance analysis, there are two sets of amplitude resonance conditions, namely, A-resonance and B-resonance, for one set of phase resonance conditions. The effects of the coupling coefficients, losses and resonant numbers on the resonance are investigated. The results show that under A-resonance, the circulating intensity is higher and the reduction factor is smaller than B-resonance under the same conditions. The free spectral range of the resonator can be significantly enhanced by the vernier effect. The effect of the ratio of the length of the two rings (RoL) on the reduction factor is also discussed.

Based on the resonators FRRER and CRRER, we have fabricated two erbium-doped fiber lasers. Narrow-bandwidth fiber Bragg gratings are employed as external reflectors for both of the lasers for better mode selections. A high power difference between the ccw and cw directions is obtained, which guarantees the unidirectional operation of the two lasers without optical isolators. Single longitudinal mode (SLM) is achieved for both lasers, but the EDFL laser with ERRER shows frequent mode hops, while the stability of SLM-EDFL laser with CRRER is much better. This is attributed to the large free spectral range of the CRRER. Based on the configuration of the FRRER, we have fabricated and characterized a new tunable dual-wavelength EDFL with outputs coming out separately from two ports of different output coupler.

Appendix A

All-Fiber Bragg Grating Filters

A1 Introduction

Over the past few years all-fiber filters have aroused considerable interests mainly because of applications in fiber-optic communications, such as channel selection in wavelength multiplexed communication systems. The introduction of fiber Bragg grating (FBG) [1-2] has opened a new horizon in the all-fiber filter area. A single FBG has been widely used as a band-stop reflection filter [3-4]. However, in general a bandpass filter is more useful than reflection filter. Several all-fiber bandpass filter designs have been constructed by using a phase-shifted fiber Bragg grating. The combination of FBG and optical circulator (OC) [5-6] can turn an FBG reflection-type filter into a transmission-type filter, but the OC could cause high cost and serious additional losses. A phase-shifted fiber Bragg grating [7] may be used as a transmission filter because it has a transmission window within the stopband. However, for system designers, it is desirable to have a bandpass filter with high throughput and nearly rectangular shape, i.e., quasi-flat-top passband shape and steep slopes. Compound phase-shifted Bragg gratings [8-9] have been proposed to give a flatter passband. A nearly flat spectral behavior was demonstrated by stacked, phase-shifted, thinfilm gratings [8], in which the individual Bragg gratings have different grating strengths. To avoid the complexity introduced by different grating strengths, a compound phase-shifted Bragg grating filter [9] with constant grating strength has been proposed. Their results show that although a

transmission spectrum with a flat top was obtained with a two-phase-shift filter, significant ripples still occur in three-phase-shift filters.

In this thesis, a new ripple-free all-fiber bandpass filter is presented. It has a symmetrical structure formed by compound phase-shifted uniform fiber Bragg gratings. Special cases for filters with 2 phase-shift and 3 phase-shift sections are discussed. The general condition for the optimum design is derived for both cases. A transfer matrix formalism is used to obtain the bandpass characteritics of the filter. It is shown that by suitably choosing the ratio of the grating lengths, a flattened spectrum could be achieved. The ripple factor is studied in terms of the ratio of the grating lengths. The dependence of the slope and 3-dB bandwidth of the passband on the ratio of the FBG lengths and coupling strength of the FBG is investigated.

A2 Theoretical Analysis

A2.1 Single FBG

Figure A.1(a) shows a schematic diagram of a single FBG. E^+ and E^- are respectively the complex field amplitudes of forward and backward propagating waves. l is the grating length. The relations of the E^+ and E^- at the two ends of the grating are given by [10]:

$$\begin{bmatrix} E^+(0) \\ E^-(0) \end{bmatrix} = [g] \cdot \begin{bmatrix} E^+(l) \\ E^-(l) \end{bmatrix} = \begin{bmatrix} m & n \\ n^* & m^* \end{bmatrix} \begin{bmatrix} E^+(l) \\ E^-(l) \end{bmatrix} \tag{A.1}$$

$$m = \left[\cosh(\gamma l) + \frac{i\delta\beta l \sinh(\gamma l)}{\gamma l} \right] \exp(\frac{i2\pi l}{\lambda_B}) \tag{A.2}$$

$$n = \frac{-\kappa l \sinh(\gamma l)\exp(\frac{-i2\pi l}{\lambda_B})}{\gamma l} \tag{A.3}$$

$$\gamma^2 = \kappa^2 - (\delta\beta)^2 \tag{A.4}$$

where m^* and n^* are the complex conjugates of m and n respectively; κ is the coupling coefficient of the grating; $\delta\beta = 2\pi(\lambda^{-1} - \lambda_B^{-1})$ is the detuning from the Bragg wavelength λ_B related to the grating period Λ as $\lambda_B = 2n_{eff}\Lambda$. Here n_{eff} is the effective mode index.

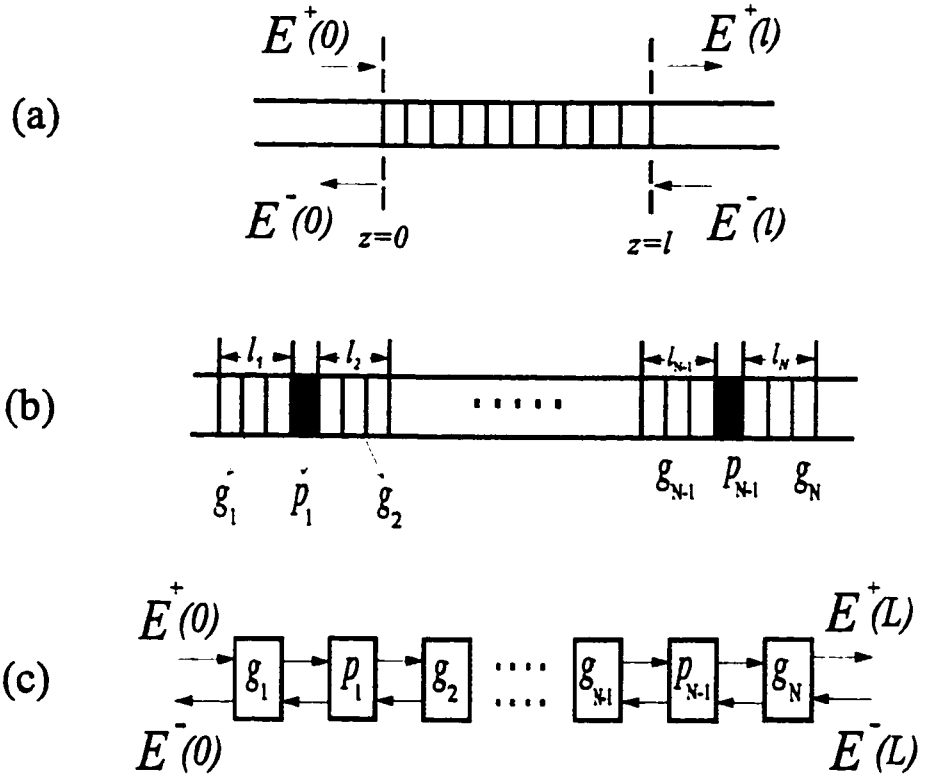

Figure A.1 Schematic diagram of FBG-filter structure: (a) single FBG, (b) compound phase-shifted GBF, and (c) transfer-matrix for (b), $g_1, \cdots, g_N$ are gratings; $p_1, \cdots, p_{N-1}$ are phase-shifts.

The reflection coefficient and transmission coefficient are then obtained by imposing the boundary condition $E^-(l)=0$, and given by:

$$r=\frac{E^-(0)}{E^+(0)}=\frac{n^*}{m} \tag{A.5}$$

$$t=\frac{E^-(l)}{E^+(0)}=\frac{1}{m} \tag{A.6}$$

A2.2 Compound Phase-shifted FBG Filter

Figure A.1(b) shows the compound FBG filter structure. The compound FBG filter has N linear gratings ($g_1,\cdots,g_N$), separated by N-1 phase-shifts ($p_1,\cdots,p_{N-1}$). Their transfer-matrix model is shown in Fig.A.1(c). The elementary matrix for a phase-shift section with a phase-shift value of ϕ could be written as:

$$[p]=\begin{bmatrix} e^{-i\phi} & 0 \\ 0 & e^{i\phi} \end{bmatrix} \tag{A.7}$$

By using the elementary matrices g and p in Eq. (A.1) and (A.7), the total transfer matrix of a compound FBG filter can be straightforwardly obtained:

$$\begin{bmatrix} E^+(0) \\ E^-(0) \end{bmatrix}=\begin{bmatrix} A & B \\ C & D \end{bmatrix}\cdot\begin{bmatrix} E^+(L) \\ E^-(L) \end{bmatrix} \tag{A.8}$$

where

$$\begin{bmatrix} A & B \\ C & D \end{bmatrix}=[g_1]\cdot[p_1]\cdots[p_i]\cdots[p_{N-1}]\cdot[g_N] \tag{A.9}$$

and L is the total length of the compound FBG filter.

By applying the boundary condition $E^-(L)=0$, the total amplitude transmission can be shown to be:

$$t = \frac{E^+(L)}{E^+(0)} = \frac{1}{A} \tag{A.10}$$

A2.3 Filter Design

The incorporation of phase-shifts gives rise to a narrow band transmission window inside the stopband of an FBG. By adjusting the magnitudes and locations of the phase-shift regions, one can tailor the transmission spectrum for specific needs. In order to get a quasi-flat-top transmission spectrum, we design filters with a symmetrical structure, and with all phase-shifts equal to $\pi/2$. In other words, $l_1 = l_N$, $l_2 = l_{N-1}, \cdots$, and $\phi_1 = \phi_2 = \cdots = \phi_{N-1} = \pi/2$, for a filter with N grating sections. Here l_N is the Nth grating length. The special cases for filters with 2 and 3 phase-shifts are discussed below.

A3 Two-Phase-Shift FBG Filter

In this case the filter has three grating sections and two phase-shifts. According to section A2, we have $N = 3$, $\phi_1 = \phi_2 = \pi/2$, and $l_1 = l_3$. From Eq. (A.10) the amplitude transmission is

$$t = \frac{1}{m_1 n_1 n_2^* + m_1 n_1^* n_2 + m_1^2 m_2 e^{-i2\phi_1} + m_2^* n_1^* e^{-i2\phi_1}} \tag{A.11}$$

A3.1 General Condition for Transmission Curve with Flattened Top

For the sake of simplicity, we assume $\delta\beta = 0$. Then, for each grating section, the reflection coefficient can be written as:

$$r_1 = r_3 = \tanh(\kappa d_1)$$
$$r_2 = \tanh(\kappa d_2) \tag{A.12}$$

From Eqs.(A.5), (A.6) and (A.11), we can obtain the normalized transmission intensity:

$$I = tt^* = \frac{(1-r_1^2)^2(1-r_2^2)}{(1-r_1^2)^2(1-r_2^2)+[r_2(1+r_1^2)+2r_1\cos 2\phi_1]} \tag{A.13}$$

By setting $I = 1$ and $\phi_1 = \pi/2$ in the above equation, one can find the general condition for unity transmission:

$$r_2(1+r_1^2) - 2r_1 = 0 \tag{A.14}$$

We introduce an important parameter, the ratio C of the grating lengths:

$$C = \frac{l_2}{l_1} \tag{A.15}$$

Subsitituting Eq.(A.12) into (A.14), one could obtain $l_2 = 2l_1$. So, $C = 2$ is the condition for unity transmission. Moreover, it is the condition for a quasi-flat-top transmission curve, as will be shown later. It is noted that we have assumed $\delta\beta = 0$, i.e., $\lambda = \lambda_B$. That means the above result holds at the central wavelength λ_B.

Fig.A.2 shows the normalized transmission intensity as a function of $\delta\lambda$ with C as a parameter, here $\delta\lambda$ is the deviation of wavelength from the central Bragg wavelength λ_B (λ_B = $1.55\mu m$). For $C > 2$, the Eq. (A.14) doesn't hold, and the maximum transimission is less than unity. This situation is called an under coupling state. For $C < 2$, there are two symmetrical peaks around λ_B, which could be explained with the help of the Eq.(A.14). For a given C there are values of $|\delta\beta|$, at which Eq.(A.14) could still hold; thus, double peaks will occur at $\pm\delta\beta$. This condition is called an over coupling state. As C approaches 2 from below, the two side

peaks approach the middle peak at $\delta\lambda = 0$. Because the magnitudes of all three peaks are unity, the result is a transmission curve with a quasi-flat top. This phenomenon persists up to $C = 2$. Thus $C_2 = 2$ is the condition for a 2-phase-shift FBG filter to have flattened transmission spectrum. Here the subscript 2 denotes the optimum value for a filter with 2 phase-shifts. This is a very desirable quality for an optical filter.

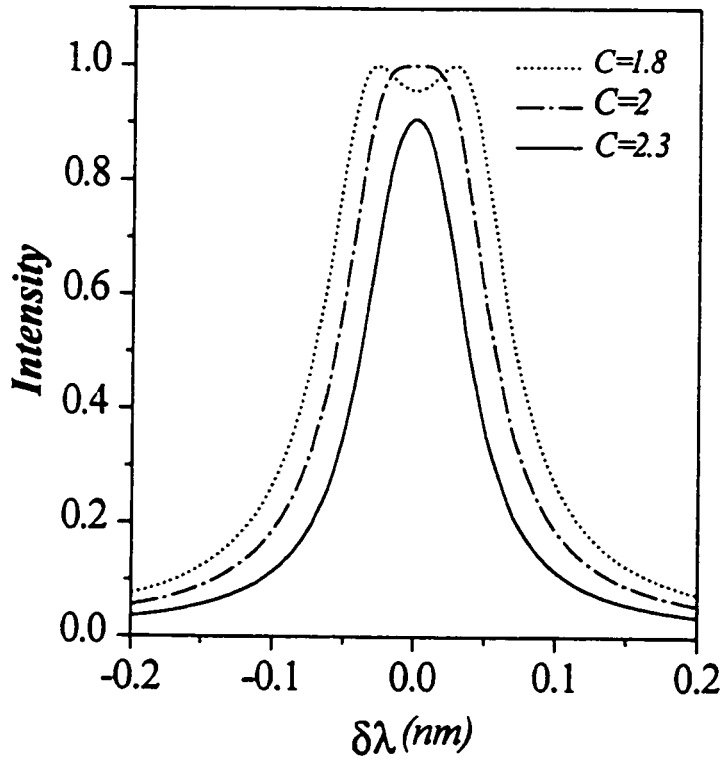

Figurer A.2 Normalized transmission intensity as a function of deviation of wavelength $\delta\lambda$, for various values of the ratio C of the grating lengths with $l_1 = 1$ mm.

A3.2 Ripple Factor

We have seen in section A3.1 that when C is smaller than C_2, there are two symmetrical peaks. This means the transmission band has ripple effects. In order to investigate how C affects the transmission curve, we define a ripple factor as:

$$R = \frac{I_{max} - I_{min}}{I_{max} + I_{min}} \tag{A.16}$$

where I_{max} is the peak intensity (unity), and I_{min} is the minimum intensity of a dip. If $R = 0$, the filter has a flat spectrum response around λ_B. It is obvious that R lies between zero and one. The ripple factor as a function of the length ratio C, with κl_1 as a parameter, is plotted in Fig.A.3 for l_1 = 1 mm. Here κl_1 is the coupling strength of the individual grating sections. The ripple factor R increases with the difference between C and the optimum value C_2. It also increases with increase of the coupling strength κl_1. All the curves converge to the optimum point $C = 2$. Therefore, the flattened transmission curve for a 2-phase-shift FBG filter can always be realized as long as the ratio $C = 2$, no matter what the coupling strength of the individual grating section is. This is a very interesting result.

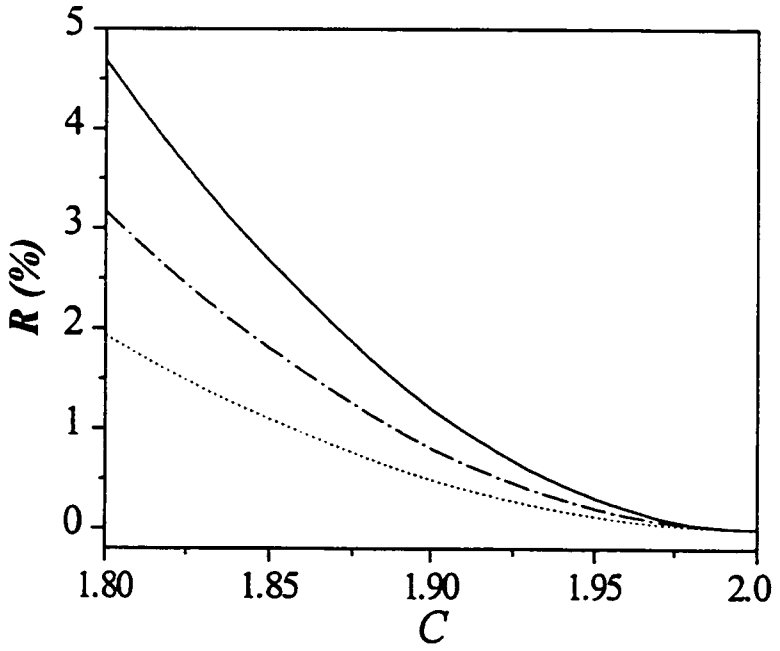

Figure A.3 Ripple factor as a function of the ratio C of the grating lengths with $l_1 = 1$ mm. Dotted curve: $\kappa l_1 = 1.4$. Dashed curve: $\kappa l_1 = 1.8$. Solid curve: $\kappa l_1 = 2.2$..

A3.3 Bandwidth and Slope

The bandwidth and slopes of the transmission band are two other important parameters that determine the effectiveness of an optical filter. Because the slope is not constant, we define the slope as that value at the 3-dB point. The bandwidth and the slope are plotted against the coupling strength κl_1 with l_1 as a parameter in Fig.A.4. Here, C is fixed at the optimum value. The bandwidth decreases and the slope increases with increase of κl_1. As the grating length l_1 decreases, the bandwidth increases and the slope decreases.

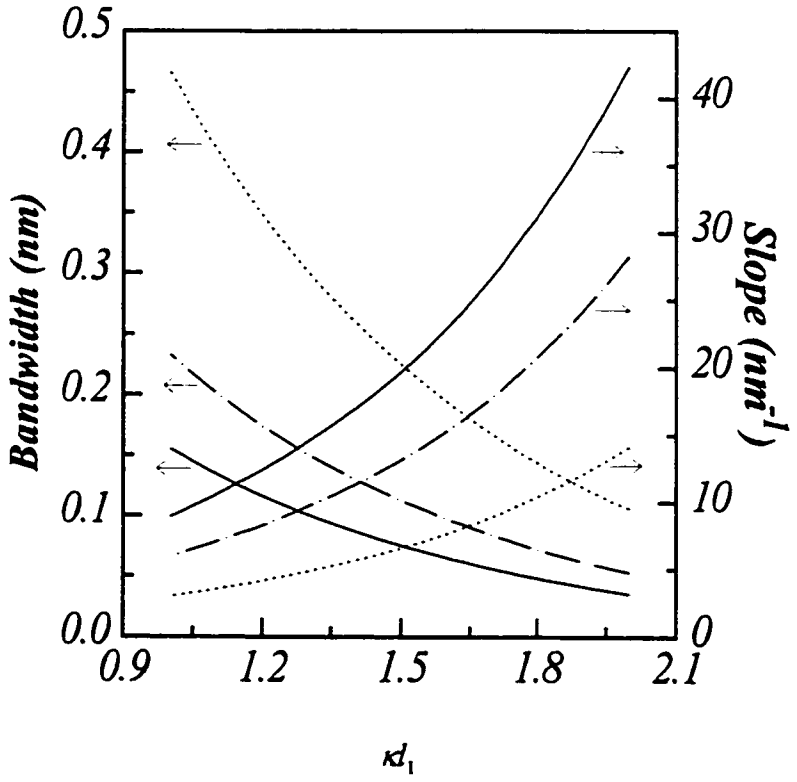

Figure A.4 Bandwidth and the slope against the coupling strength κl_1. Dotted curve: $l_1 = 0.5$ mm. Dashed curve: $l_1 = 1.0$ mm. Solid curve: $l_1 = 1.5$ mm.

A4 Three-Phase-Shift FBG Filter

The three-phase-shift FBG filter has four FBGs and three phase-shifts. They are designed with $l_1 = l_4$, $l_2 = l_3$, and $\phi_1 = \phi_2 = \phi_3 = \pi/2$. With the help of Eq.(A.10) the amplitude transmission is

$$t = \frac{1}{D} \tag{A.17}$$

$$\begin{aligned} D = {} & (m_1 m_2)^2 e^{-i3\phi} + m_1 m_2 n_1^* n_2 e^{-i\phi} + m_1 m_2 n_1 n_2^* e^{-i\phi} + n_1 n_1^* n_2 n_2^* e^{i\phi} \\ & + m_1^* n_2 n_2^* e^{-i\phi} + m_1 m_2^* n_1^* n_2 e^{i\phi} + m_1 m_2^* n_1 n_2^* e^{i\phi} + (m_2^* n_1^*)^2 e^{i3\phi} \end{aligned} \tag{A.18}$$

A4.1 General Condition for Transmission Curve with Flattened Top

We assume $\delta\beta = 0$. Then, the reflection coefficients of the four fiber Bragg gratings are

$$\begin{aligned} r_1 &= r_4 = \tanh(\kappa l_1) \\ r_2 &= r_3 = \tanh(\kappa l_2) \end{aligned} \tag{A.19}$$

The intensity transmission can be derived by using Eqs.(A.5), (A.6) and (A.17) as

$$I = \frac{1}{1 + \dfrac{2r_1^2(1+x)(2x+H-1)^2}{(1-r_1^2)^2(1-r_2)^2}} \tag{A.20}$$

where $x = \cos(2\phi_1)$, and $H = r_2^2 + r_2(r_1 + 1/r_1)$.

From Eq. (A.20) we find the condition for unity transmission

$$x = -1$$

or (A.21)

$$H = 1 - 2x$$

where the first condition gives to the central peak at λ_B, and the second condition gives the 2 side peaks. It is obvious that the first condition is automatically satisfied with $\phi_1 = \pi/2$ which

means the intensity transmission is always unity at the central Bragg wavelength. When that is satisfied, the second condition becomes:

$$r_2^2 + r_2(r_1 + \frac{1}{r_1}) = 3 \tag{A.22}$$

If Eq.(A.22) holds, then the three peaks will overlap at the central Bragg wavelength λ_B, which will make the transmission curve a quasi-flat top. So Eq.(A.22) is the optimum condition for a flattened response. After substituting Eq. (A.19) into (A.22), one could obtain the optimum value C_3 by numerical calculation. It is noted that unlike the case of a *2*-phase-shift FBG filter which has a constant $C_2 = 2$, a 3-phase-shift FBG filter has a variable C_3, which is a function of the grating strength κl_1.

The dependence of the optimum value C_3 on the κd_1 is plotted in Fig.A.5. As κd_1 increases, the optimum length ratio C_3 decreases. So, for a given grating strength, a quasi-flat-top bandpass filter could be realized by adjusting the grating length ratio C. For example, at $\kappa d_1 = 1.5$, C_3 is 2.23. Fig.A.6 shows the transmission intensity characteristics of a filter as a function of $\delta\lambda$ with C as a parameter for $\kappa d_1 = 1.5$ and $l_1 = 1$ *mm*. It is clear from Fig.A.6 that $C = C_3 = 2.23$ is the optimum ratio for a flattened transmission response.

A4.2 Ripple Factor

Figure A.6 shows that when $C < C_3$, three peaks exist, i.e., the response shows a ripple phenomenon. The ripple factor as a function of the ratio C is shown in Fig.A.7 for various values of κl_1. All the curves end at their corresponding optimum values of C. It is obvious that the ripple factor increases as the grating length ratio C deviates from C_3. It is noted that each curve has a region where R is almost zero, within which the transmission curve is almost

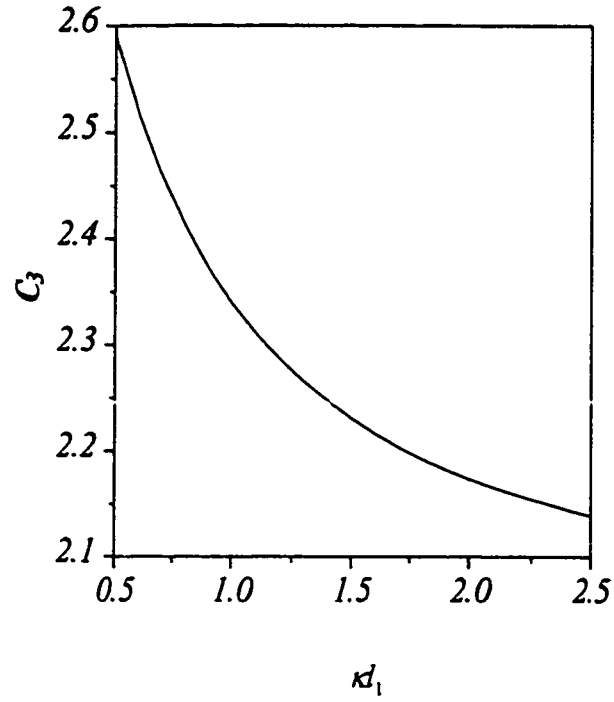

Figure A.5 Optimum value C_3 for a three-phase-shift FBG against the grating strength κl_1 with $l_1 = 1$ mm

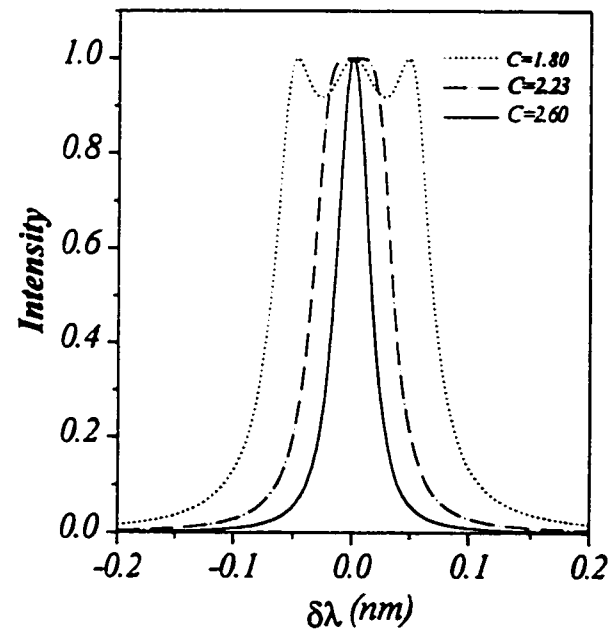

Figure A.6 Transmission intensity as a function of $\delta\lambda$ for various of the ratio C of the grating lengths with $\kappa l_1 = 1.5$ and $l_1 = 1$ mm.

ripple-free. For example, for $\kappa l_1 = 1.5$, the "ripple-free" region could be given by C between 2.15 and 2.23. This range becomes wider as the grating strength κl_1 decreases. This property allows filters to be much more easily fabricated. It also makes the filters much less sensitive to the environment, which could change the individual grating lengths.

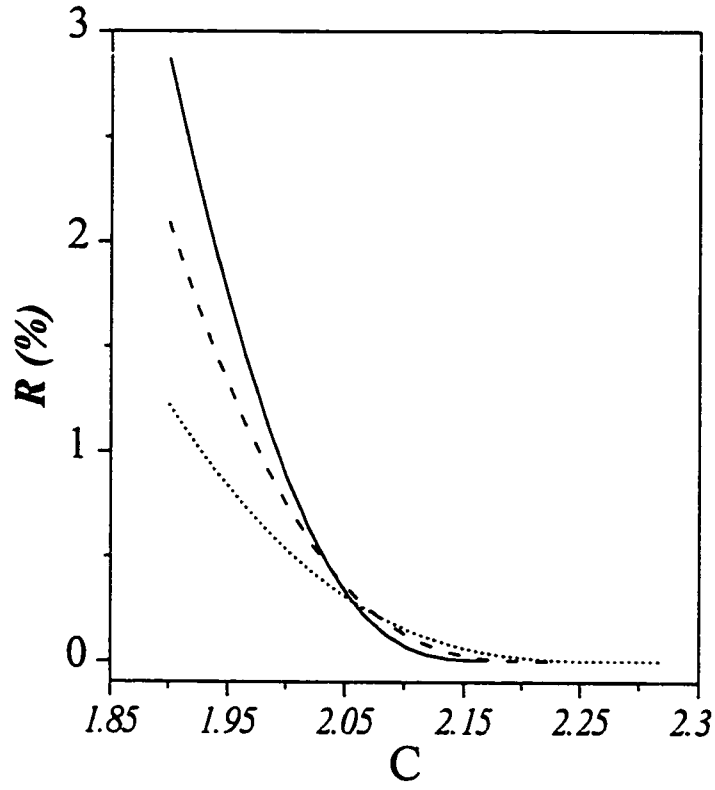

Figure A.7 Ripple factor as a function of the ratio of C of the grating lengths for various values of with κl_1 and $l_1 = 1$ mm. Dotted curve: $\kappa l_1 = 1.0$. Dashed curve: $\kappa l_1 = 1.5$. Solid curve: $\kappa l_1 = 2.0$.

A4.3 Bandwidth and Slope

The bandwidth and the slope as functions of the grating strength κl_1 are plotted in Fig. A.8 with l_1 as a parameter with C assuming its optimum value; thus the transmission curves are

ripple-free. Just as in the 2-phase-shift FBG filter, as κl_1 increases, the bandwidth decreases and the slope increases; as l_1 decreases, the bandwidth increases and the slope decreases. Comparison of Figs.A.4 and A.8 shows that for the same grating strength κl_1 a 3-phase-shift filter has a smaller bandwidth, and a larger slope than a 2-phase-shift filter. To show this comparison more clearly, the transmission curves for the two cases with the same bandwidths are shown in Fig.A.9. These curves show that the transmission curve is more nearly rectangular in the case of a 3-phase-shift filter than in the case of a 2-phase-shift filter, with the bandwidths being equal. So, the characteristics of a filter could be improved significantly by introducing additional grating and phase-shift sections; however, this will also increase the fabrication complexities and the physical length of the filter.

A5 Summary

A theoretical study of phase-shifted fiber Bragg grating filters has been presented. Special cases with 2 and 3 phase-shift sections are discussed in detail. The general optimum conditions for ripple-free transmission curves are derived exactly. A critical parameter is the ratio C of the grating lengths. For a 2-phase-shift FBG filter, the optimum condition occurs at $C_2 = 2$. For a 3-phase-shift FBG filter, the optimum value C_3 is variable; it decreases with increase of κl_1. As κl_1 changes, the bandwidth and slope change in opposite directions. For the same bandwidth a 3-phase-shift filter has a more rectangular intensity transmission curve than a 2-phase-shift filter. Such a property could be specially useful in applications such as channel selection in wavelength-multiplexed optical fiber communication systems.

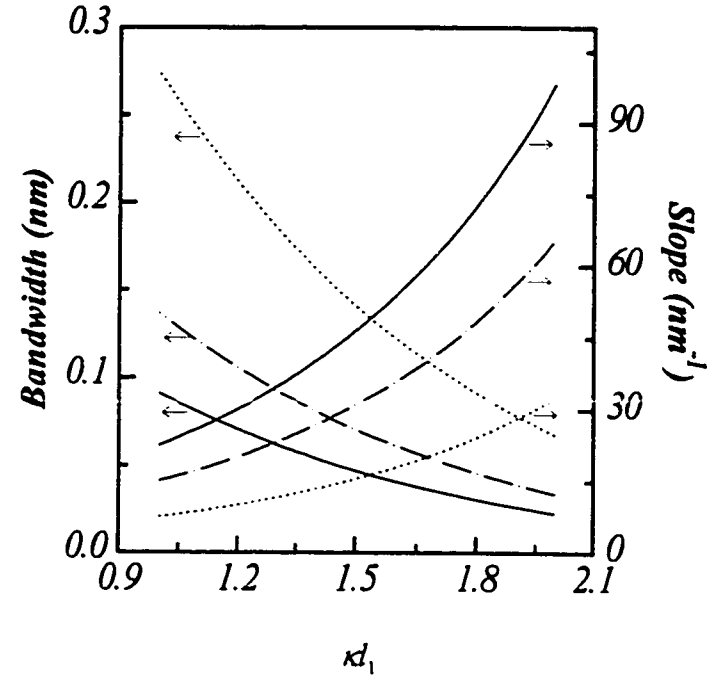

Figure A.8 Bandwidth and slope as functions of the grating strength κd_1. Dotted curve: $l_1 = 0.5$ mm. Dashed curve: $l_1 = 1.0$ mm. Solid curve: $l_1 = 1.5$ mm.

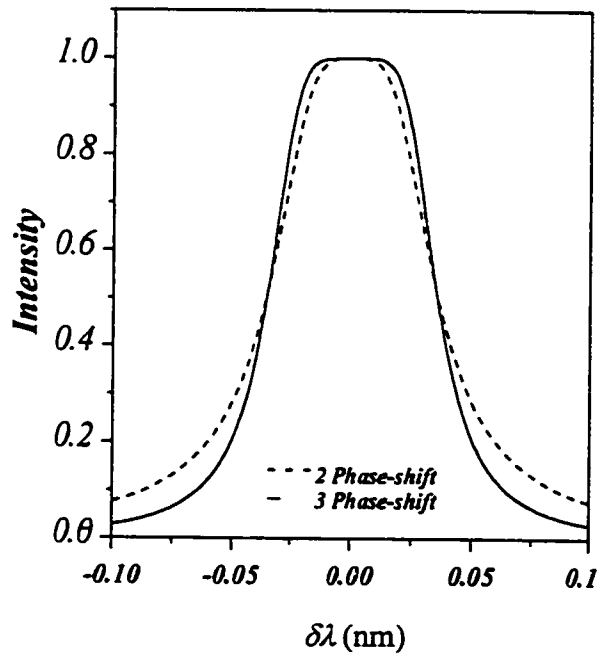

Figure A.9 Transmission characteristics of the two-phase-shift filter and three-phase-shift against the deviation wavelength $\delta\lambda$ with the same bandwidth $l_1 = 1$ mm.

A6 Reference

1. K.O.Hill, Y.Fujii, D.C.Johnson, and B.S.Kawasaki, "Photosensitivity in optical fiber waveguide: Applications to reflective filter fabrication," *Appl. Phys. Lett.*, vol. 32, pp. 647-649, 1978.
2. G.Meltz, W.W.Morey, and W.H.Glen, "Formation of Bragg grainges in optical fiber by a transverse holographic method," *Opt. Lett.*, vol. 14, pp. 823-825, 1989.
3. R. Kashyap, P.F.Mckee and D. Armes, "UV written reflection grating structure in photosensitive optical fibers using phase-shifted phase mases," *Electron. Lett.*, vol.30, pp. 1977-1978, 1994.
4. J.L.Archambault, L.Reekie, and P.St.J. Russell, "High reflectivity and narrow bandwidth fiber grating written by a single excimer pulse," *Electron. Lett.*, vol. 29, pp. 28-29, 1993.
5. J.Capmany,R.I.Laming, and D.N.Payne, "A novel highly selective and tunable optical bandpass filter using a fiber grating and a fiber Fabry-Perot," *Microwave and Optical Tech. Lett.*, vol. 7, pp. 499-501, 1994.
6. T.Komukai, Y.Miyajima, and M.Nakazawa, "An in-line optical bandpass filter with fiber gratings and an optical circulator and its application to pulse compression, " *Jpn. J. Appl. Phys.*, vol. 34, pp. L230-232, 1995.
7. G.P. Agrawal and S. Radic, "Phase-shifted fiber Bragg Grating and their application for wavelength demultiplexing," *IEEE Photonics Tech. Lett.*, vol. 6, pp. 995-997, 1994.
8. C.H. Henry, Y. Shani, R.C. Kistler, T.E. Jewell, V. Pol, N.A. Olsson, R.F. Kazarinov, and K.J. Orlowsky, "Compound Bragg reflection filters made by spatial frequency doubling lithography," *J. Lightwave Technol.*, vol.7, pp1379-1385, 1989.

9. R. Zengerle and O. Leminger, "Phase-shifted Bragg-grating filters with improved transmission characteristics," *J. Lightwave Technol.*, vol.13, pp2354-2358, 1995.

10. M.Yamada and K. Sakuda, "Analysis of almost-periodic distributed feedbach slab waveguides via a fundamental matrix approach, " *Appl. Opt.*, Vol. 26, pp3474-3478, 1987.

Appendix B Loss Difference of FRRER

We derive the expression for loss difference given in Eq. (3.2). Referring to Fig. 3.2, the intensities at the four ports of the coupler can be written as

$$\begin{bmatrix} I_{1a} \\ I_{2a} \\ I_{3a} \\ I_{4a} \end{bmatrix} = \begin{bmatrix} 0 & 0 & b^2 & a^2 \\ 0 & 0 & a^2 & b^2 \\ b^2 & a^2 & 0 & 0 \\ a^2 & b^2 & 0 & 0 \end{bmatrix} \cdot \begin{bmatrix} I_{1t} \\ I_{2t} \\ I_{3t} \\ I_{4t} \end{bmatrix} \tag{B.1}$$

and other relations are

$$I_{1t} = I_{4t} = I_{in} \tag{B.2}$$

$$I_{2t} = 0 \tag{B.3}$$

$$I_{3t} = R \cdot I_{3a} \tag{B.4}$$

where $a = \sqrt{(1-k)(1-\gamma)}$, and $b = \sqrt{k(1-\gamma)}$. The subscripts a and t denote the light travelling away from and toward the coupler.

From Eqs.(B.1)-(B.4), the loss difference can be straightforwardly obtained as following:

$$LD = 10\log(\frac{I_{1a}}{I_{4a}}) = 10\log\left[\frac{k^2(1-\gamma)^2 R}{1-k} + 1\right] \tag{B.5}$$

Appendix C

C1 Electric fields in Case I

Figure 3.5(a) shows the configuration of Case I, which consists of a ring resonator. In order to investigate the properties of the resonator, one should find the electric fields in each port. For clarity, in the following, we use a and t as subscripts of fields to denote the field travelling away from or towards the coupler.

Referring to Fig.3.5(a), the electric fields at the four ports of the coupler can be related by matrix equation:

$$\begin{bmatrix} E_{1a} \\ E_{2a} \\ E_{3a} \\ E_{4a} \end{bmatrix} = \begin{bmatrix} 0 & 0 & jb & a \\ 0 & 0 & a & jb \\ jb & a & 0 & 0 \\ a & jb & 0 & 0 \end{bmatrix} \cdot \begin{bmatrix} E_{1t} \\ E_{2t} \\ E_{3t} \\ E_{4t} \end{bmatrix} \tag{C.1}$$

other relations can be given by:

$$E_{1t} = E_{4a} e^{-(\alpha l + \xi) + i\beta l} \tag{C.2}$$

$$E_{2t} = E_{in} \tag{C.3}$$

$$E_{3t} = 0 \tag{C.4}$$

$$E_{4t} = E_{1a} e^{-(\alpha l + \xi) + i\beta l} \tag{C.5}$$

with

$$\begin{aligned} a &= \sqrt{(1-k)(1-\gamma)} \\ b &= \sqrt{k(1-\gamma)} \end{aligned} \tag{C.6}$$

where Eq.(C.1) is based on the coupled-wave equations, while Eqs.(C.2) and (C.5) are based on propagation relations along fibers; a and b are the effective transmission coefficient and reflection coefficient. The parameters α and β are the amplitude

attenuation coefficient, the propagation constant of the fiber; ξ and l are the splicing loss and length of the fiber ring, respectively.

From Eqs.(C.1)-(C.5), the circulating intensity and output intensity can be straightforwardly obtained as follows:

$$\frac{E_{4a}}{E_{in}} = \frac{jb}{1 - ae^{-(\alpha l + \xi)} e^{i\beta l}} \tag{C.7}$$

$$\frac{E_{1a}}{E_{in}} = \frac{a - (1-\gamma) e^{-(\alpha l + \xi)} e^{i\beta l}}{1 - ae^{-(\alpha l + \xi)} e^{i\beta l}} \tag{C.8}$$

C2 Electric fields in Case II

The configuration of Case II is shown in Fig.3.5(b). The difference between Case II and Case I is in that an end reflector is added at port 3 and the input light is launched at port 2 instead of port 3 in Case I. Therefore, the above equations for Case I can be applied except that Eqs.(C.3) and (C.4) are replaced by the following two equations:

$$E_{2l} = E_{in} \tag{C.9}$$

$$E_{3l} = r \cdot E_{3a} e^{-(\alpha l_0 + \xi_0) + (i\beta l_0 + \delta_0)} \tag{C.10}$$

where parameters r, δ_0, ξ_0 and l_0 are the amplitude reflectivity of the ER, the phase change due to the ER, the splicing loss and the fiber length between port 3 and the end reflector, respectively.

Based on Eqs.(C.1)-(C.2), (C.5)-(C.6), and (C.9)-(C.10), the circulating intensities and output intensity can be solved as:

$$\frac{E_{4a}}{E_{in}} = \frac{jb}{1 - ae^{-(\alpha l + \xi)} e^{i\beta l}} \tag{C.11}$$

$$\frac{E_{1a}}{E_{in}} = \frac{jrbe^{-(\alpha l_0+\xi_0)}e^{i\beta l_0}e^{i\delta_0}}{1-ae^{-(\alpha l+\xi)}e^{i\beta l}} \cdot E_{3a}$$
$$= \frac{jrbe^{-(\alpha l_0+\xi_0)}e^{i\beta l_0}e^{i\delta_0}}{1-ae^{-(\alpha l+\xi)}e^{i\beta l}} \cdot \frac{a-(1-\gamma)e^{-(\alpha l+\xi)}e^{i\beta l}}{1-ae^{-(\alpha l+\xi)}e^{i\beta l}} \qquad \text{(C.12)}$$

$$E_{2a} = re^{-(\alpha l_0+\xi_0)}e^{i\beta l_0}e^{i\delta_0} \cdot (E_{3a})^2$$
$$= re^{-(\alpha l_0+\xi_0)}e^{i\beta l_0}e^{i\delta_0} \cdot \left[\frac{a-(1-\gamma)e^{-(\alpha l+\xi)}e^{i\beta l}}{1-ae^{-(\alpha l+\xi)}e^{i\beta l}}\right]^2 \qquad \text{(C.13)}$$

Appendix D

D1 Electric fields of CRR

we use the coupled wave equations for the coupler and propagation relations between different points along the fiber to derive the output and circulating fields, where the coupled wave equations are formulated in matrix form.

Referring to Fig.4.1, we obtain the following equations:

$$\begin{bmatrix} E_{1a} \\ E_{2a} \\ E_{3a} \\ E_{4a} \end{bmatrix} = \begin{bmatrix} 0 & 0 & ib_1 & a_1 \\ 0 & 0 & a_1 & ib_1 \\ ib_1 & a_1 & 0 & 0 \\ a_1 & ib_1 & 0 & 0 \end{bmatrix} \cdot \begin{bmatrix} E_{1t} \\ E_{2t} \\ E_{3t} \\ E_{4t} \end{bmatrix} \tag{D.1}$$

$$\begin{bmatrix} E_{5a} \\ E_{6a} \\ E_{7a} \\ E_{8a} \end{bmatrix} = \begin{bmatrix} 0 & 0 & ib_2 & a_2 \\ 0 & 0 & a_2 & ib_2 \\ ib_2 & a_1 & 0 & 0 \\ a_1 & ib_2 & 0 & 0 \end{bmatrix} \cdot \begin{bmatrix} E_{5t} \\ E_{6t} \\ E_{7t} \\ E_{8t} \end{bmatrix} \tag{D.2}$$

and

$$E_{3t} = E_{in} \tag{D.3}$$

$$E_{4t} = E_{7a} e^{(-\alpha + i\beta)L_2 + \xi} \tag{D.4}$$

$$E_{5t} = E_{2a} e^{(-\alpha + i\beta)L_1 + \xi_1} \tag{D.5}$$

$$E_{6t} = E_{1a} e^{(-\alpha + i\beta)L_1 + \xi_3} \tag{D.6}$$

we also have

$$E_{1t} = E_{2t} = E_{7t} = E_{8t} = 0 \tag{D.7}$$

where $j=(-1)^{1/2}$, $a_i=\sqrt{(1-k_i)(1-\gamma_i)}$, $b_i=\sqrt{k_i(1-\gamma_i)}$ with i = 1, 2, and γ_i is the coupler intensity loss coefficient the ith coupler. The parameters α, β, ξ_i (i = 1, 2, 3) are, respectively, the amplitude attenuation coefficient, the propagation constant and the splicing loss of the fiber. The subscripts a and t denote the field travelling away from and towards the corresponding couplers.

The output and circulating fields are easily obtained from Eqs.(D.1) - (D.7) as follows:

$$E_{1a}=\frac{i[b_1+b_2p_sq_s(1-\gamma_1)]}{p_2q_2(1-a_1a_2p_pq_p+b_1b_2p_sq_s)}E_{in} \tag{D.8}$$

$$E_{8a}=\frac{(a_1a_2p_sq_s+b_1b_2p_pq_p)-p_sq_sp_pq_p(1-\gamma_1)(1-\gamma_2)}{p_2q_2(1-a_1a_2p_pq_p+b_1b_2p_sq_s)}E_{in} \tag{D.9}$$

where

$$\begin{aligned} p_i&=e^{(-\alpha L_i+\xi_i)}\\ q_i&=e^{j\beta L_i} \end{aligned} \qquad (i=1,2,s,p) \tag{D.10}$$

The subscripts 1, 2, s and p denote the values for the fiber segment L_1, L_2, L_s, and L_p, respectively.

D2 Electric fields of double-coupler ring resonator with an external reflector

The schematic diagram of the double-coupler ring resonator with an external reflector (DCRRER) is shown in Fig.D.1. It is just the structure of the right side of the dash line in Fig.4.12.

To find the electric fields at port 1, 6 and 8, first we need to write the equations related to the eight ports as in appendix A and B, which are as following:

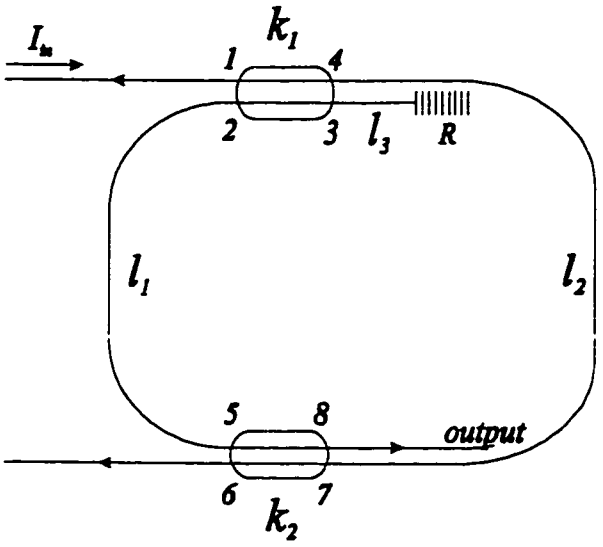

Figure D.1 Configuration of the DCRRER

$$\begin{bmatrix} E_{1a} \\ E_{2a} \\ E_{3a} \\ E_{4a} \end{bmatrix} = \begin{bmatrix} 0 & 0 & ib_1 & a_1 \\ 0 & 0 & a_1 & ib_1 \\ ib_1 & a_1 & 0 & 0 \\ a_1 & ib_1 & 0 & 0 \end{bmatrix} \cdot \begin{bmatrix} E_{1t} \\ E_{2t} \\ E_{3t} \\ E_{4t} \end{bmatrix} \tag{D.11}$$

$$\begin{bmatrix} E_{5a} \\ E_{6a} \\ E_{7a} \\ E_{8a} \end{bmatrix} = \begin{bmatrix} 0 & 0 & ib_2 & a_2 \\ 0 & 0 & a_2 & ib_2 \\ ib_2 & a_1 & 0 & 0 \\ a_1 & ib_2 & 0 & 0 \end{bmatrix} \cdot \begin{bmatrix} E_{5t} \\ E_{6t} \\ E_{7t} \\ E_{8t} \end{bmatrix} \tag{D.12}$$

and

$$E_{1t} = E_{in} \tag{D.13}$$

$$E_{2t} = E_{5a} e^{(-\alpha + i\beta) l_1 + \xi_1} \tag{D.14}$$

$$E_{3t} = E_{3a} e^{(-\alpha + i\beta) l_3 + \xi_3} \tag{D.15}$$

$$E_{4t} = E_{7a} e^{(-\alpha + i\beta) l_2 + \xi_2} \tag{D.16}$$

$$E_{5t} = E_{2a} e^{(-\alpha + i\beta) l_1 + \xi_1} \tag{D.17}$$

$$E_{7t} = E_{4a} e^{(-\alpha + i\beta) l_2 + \xi_2} \tag{D.18}$$

we also have

$$E_{6t} = E_{8t} = 0 \tag{D.19}$$

The above equations may be solved to give:

$$\frac{E_{6a}}{E_{in}} = \frac{a_1 a_2 p_2 q_2}{1 + b_1 b_2 p_s q_s} \tag{D.20}$$

$$\frac{E_{3a}}{E_{in}} = -\frac{i[b_1 + b_2(1-\gamma_1) p_s q_s]}{1 + b_1 b_2 p_s q_s} \tag{D.21}$$

$$\frac{E_{1a}}{E_{in}} = -\frac{r[b_1 + b_2(1-\gamma_1) p_s q_s]^2}{(1 + b_1 b_2 p_s q_s)^2} = r(E_{3a})^2 \tag{D.22}$$

$$\frac{E_{8a}}{E_{in}} = i\frac{r a_1 a_2 p_1 q_1 [b_1 + b_2(1-\gamma_1) p_s q_s]}{(1 + b_1 b_2 p_s q_s)^2} = r E_{3a} E_{6a} p_1 q_1 / p_2 q_2 \tag{D.23}$$

where

$$\begin{aligned} p_i &= e^{(-\alpha L_i + \xi_i)} \\ q_i &= e^{i\beta L_i} \end{aligned} \qquad (i = 1,2,s) \tag{D.24}$$

The subscripts 1, 2 and s denote the values for the fiber segment l_1, l_2, l_s, and $l_s = l_1 + l_2$.

Other parameters have the same definition as in appendix D1.

By setting $E_{8a} = 0$, the optimum resonance conditions can be obtained as:

$$\begin{aligned} k_1 &= k_2(1-\gamma_1) p_s^2 \\ \beta \cdot l_s &= (2m+1)\pi \end{aligned} \tag{D.25}$$

Appendix E

E1 Principle of operation of interferometer

Fabry-Perot-type or ring-type interferometers are essentially ultra-narrow linewidth filters which produce a series of sharp transmission peaks as the cavity length is slightly varied with the scanning of the piezo-electric ramp voltage. The difference between FP and ring type interferometer is that transmission curve is channel-passing type for FP while channel-blocking for ring interferometer. In another words, when the cavity is on resonance, FP type has a maximum transmission and ring type has a minimum transmission. The resonance occurs when

$$\frac{2nL}{\lambda} = m \qquad \text{(FP resonator)} \qquad \text{(E.1)}$$

$$\frac{nL}{\lambda} = m \qquad \text{(Ring resonator)} \qquad \text{(E.2)}$$

where L is the cavity length, n is the refractive index of cavity path, and m is integer.

From Eq. (E1-E2) one can obtain the following expression for the change $d\nu$ in the resonance frequency of a given transmission peak due to a length variation dl

$$\frac{d\nu}{FSR} = -\frac{dl}{(\lambda/2n)} \qquad \text{(FP resonator)} \qquad \text{(E.3)}$$

$$\frac{d\nu}{FSR} = -\frac{dl}{(\lambda/n)} \qquad \text{(Ring resonator)} \qquad \text{(E.4)}$$

According to Eqs.(E3) and (E4), we can tune the peak transmission frequency of the interferometer by 1 FSR by changing its length half a wavelength or a wavelength. This property is utilized in operating FP or ring resonator as a scanning interferometer. The optical signal to be analyzed passes through the resonator as its length is being swept. If

the width of the transmission peaks is small compared to that of the spectral detail in the incident optical beam signal, the output of the resonator will constitute a replica of the spectral profile of the signal.

The finesse of the interferometer can be written as [1]

$$F = \frac{\pi\sqrt{R}}{1-R} \qquad \text{(FP resonator)} \qquad \text{(E.5)}$$

(Fiber ring resonator) (E.6)

$$k_r = 1-(1-\gamma_0)(1-a_0)\exp(-2\alpha L) \qquad \text{(E.7)}$$

where R is the reflectivity of the FP mirrors; a_0 is the splice intensity loss; α is the fiber loss per unit length, γ_0 is the coupler insertion loss and L is the fiber loop length.

E2 Structure of interferometer

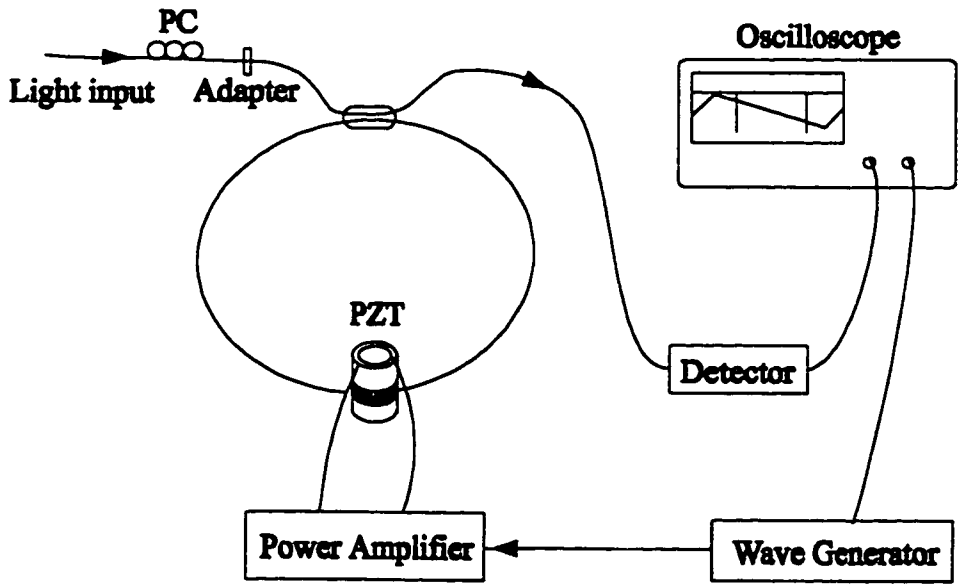

Figure E.1 Scanning ring interferometer experimental arrangement.

Figure E.1 shows the schematic of the homemade fiber ring interferometer. The phase modulation is achieved by fiber stretching. The fiber is wound around a PZT cylinder whose diameter is changed by a voltage supplied by a power amplifier. The laser output is coupled from one port of the coupler and the output is connected to a detector, which converts the optical signal to electrical signal. The detail spectrum is shown from the oscilloscope.

Reference:

1. F. Zhang and J.W.Y. Lit, "Direct-coupling single-mode fiber ring resonator", *J. Opt. Soc. Am. A*, vol.5, No.8, Aug. 1988.

List of Publications

1. L. Wei and J. W.Y. Lit, "Compound ring resonator with an external reflector for lasers", in preparation.

2. L. Wei and J. W.Y. Lit, "Compound ring resonator with double couplers", in preparation.

3. Li Wei and J.W.Y. Lit, "Traveling-wave Single-mode Er-doped Fiber Laser," *Proc. SPIE*, vol. 3280, pp111-118, 1998.

4. Li Wei and J.W.Y. Lit, "Erbium doped fiber ring laser with an external fiber Bragg grating", *Proc. IEEE LEOS*, Nov. 1997.

5. Li Wei and J.W.Y. Lit, "Phase-shifted Bragg Grating filters with symmetrical Structures", *J. Lightwave Technol.*, vol. 15, pp1405-1410, Aug. 1997.

6. Li Wei, and J.W.Y. Lit, "Fibre ring resonator with stable eigenstate of polarization", *Physics in Canada*, CAP 97', Calgary, Vol.53, No.3, PC9, June 1997.

7. Li Wei and J.W.Y. Lit, "Three-Coupler Double-Ring Fiber Resonator for Lasers," *Microwave and Optical Technology Letters*, vol.12, pp.73-77, June 1996.